# The Effects of Load History and Design Variables on Performance Limit States of Circular Bridge Columns
Volume 3: Analysis Methods

Prepared By:
Yuhao Feng
Jason Chad Goodnight
Mervyn J. Kowalsky
James M. Nau
North Carolina State University

January 2015

REPORT DOCUMENTATION PAGE	Form approved OMB No. 298

Public reporting for this collection of information is estimated to average 1 hour per response, including the time for reviewing instructions, searching existing data sources, gathering and maintaining the data needed, and completing and reviewing the collection of information. Send comments regarding this burden estimate or any other aspect of this collection of information, including suggestion for reducing this burden to Washington Headquarters Services, Directorate for Information Operations and Reports, 1215 Jefferson Davis Highway, Suite 1204, Arlington, VA 22202-4302, and to the Office of Management and Budget, Paperwork Reduction Project (0704-1833), Washington, DC 20503

1. AGENCY USE ONLY (LEAVE BLANK) 4000(72)	2. REPORT DATE January 2015	3. REPORT TYPE AND DATES COVERED FINAL, November 2008 through January 2015

4. TITLE AND SUBTITLE	5. FUNDING NUMBERS
The Effects of Load History and Design Variables on Performance Limit States of Circular Bridge Columns – Volume 3: Analysis Methods	AKSAS #60855/T2-08-02 Federal # HPR-4000(72)

6. AUTHOR(S)
Yuhao Feng
Jason Chad Goodnight
Mervyn J. Kowalsky
James M. Nau

7. PERFORMING ORGANIZATION NAME(S) AND ADDRESS(ES) North Carolina State University	8. PERFORMING ORGANIZATION REPORT NUMBER 4000(72)

9. SPONSORING/MONITORING AGENCY NAME(S) AND ADDRESS(ES) Alaska Department of Transportation and Public Facilities Research, Development &Technology Transfer P.O. Box 112500 3132 Channel Drive Juneau, AK 99811-2500	10. SPONSORING/MONITORING AGENCY REPORT NUMBER 4000(72)

11. SUPPLEMENTARY NOTES

12a. DISTRIBUTION / AVAILABILITY STATEMENT No restrictions.	12b. DISTRIBUTION CODE

13. ABSTRACT (Maximum 200 words)
This report is the third of three volumes and presents the numerical portion of the research project on the impacts of loading history on the behavior of reinforced concrete bridge columns. Two independent finite element methods were utilized to accomplish the goal of this research work. First, fiber-based analysis was utilized which employed the Open System for Earthquake Engineering Simulation (OpenSees). The second model uses solid elements to predict bar buckling. The model included a segment of reinforcing bar and its surrounding elements, such as spiral turns and concrete. A series of strain histories from the experimental tests and fiber-based analyses were applied to the finite element model to study their impacts on the strain limit for reinforcing bar buckling.

Initial analytical investigations have shown significant impact of load history on the strain demand to lead to reinforcing bar buckling in the plastic hinge region. The parametric study extended the range of load history types and also studied the effect of reinforcement detailing on bar buckling. A design approach was developed to include the load history effect on the strain limit state of bar buckling.

14. KEYWORDS : Seismic, reinforced concrete, strain limits, buckling, performance-based design, bridge design, plastic hinge lengths	15. NUMBER OF PAGES 165
	16. PRICE CODE N/A

17. SECURITY CLASSIFICATION OF REPORT Unclassified	18. SECURITY CLASSIFICATION OF THIS PAGE Unclassified	19. SECURITY CLASSIFICATION OF ABSTRACT Unclassified	20. LIMITATION OF ABSTRACT N/A

SI* (MODERN METRIC) CONVERSION FACTORS

APPROXIMATE CONVERSIONS TO SI UNITS

Symbol	When You Know	Multiply By	To Find	Symbol
LENGTH				
in	inches	25.4	millimeters	mm
ft	feet	0.305	meters	m
yd	yards	0.914	meters	m
mi	miles	1.61	kilometers	km
AREA				
in^2	square inches	645.2	square millimeters	mm^2
ft^2	square feet	0.093	square meters	m^2
yd^2	square yard	0.836	square meters	m^2
ac	acres	0.405	hectares	ha
mi^2	square miles	2.59	square kilometers	km^2
VOLUME				
fl oz	fluid ounces	29.57	milliliters	mL
gal	gallons	3.785	liters	L
ft^3	cubic feet	0.028	cubic meters	m^3
yd^3	cubic yards	0.765	cubic meters	m^3
NOTE: volumes greater than 1000 L shall be shown in m^3				
MASS				
oz	ounces	28.35	grams	g
lb	pounds	0.454	kilograms	kg
T	short tons (2000 lb)	0.907	megagrams (or "metric ton")	Mg (or "t")
TEMPERATURE (exact degrees)				
^oF	Fahrenheit	5 (F-32)/9 or (F-32)/1.8	Celsius	^oC
ILLUMINATION				
fc	foot-candles	10.76	lux	lx
fl	foot-Lamberts	3.426	candela/m^2	cd/m^2
FORCE and PRESSURE or STRESS				
lbf	poundforce	4.45	newtons	N
lbf/in^2	poundforce per square inch	6.89	kilopascals	kPa

APPROXIMATE CONVERSIONS FROM SI UNITS

Symbol	When You Know	Multiply By	To Find	Symbol
LENGTH				
mm	millimeters	0.039	inches	in
m	meters	3.28	feet	ft
m	meters	1.09	yards	yd
km	kilometers	0.621	miles	mi
AREA				
mm^2	square millimeters	0.0016	square inches	in^2
m^2	square meters	10.764	square feet	ft^2
m^2	square meters	1.195	square yards	yd^2
ha	hectares	2.47	acres	ac
km^2	square kilometers	0.386	square miles	mi^2
VOLUME				
mL	milliliters	0.034	fluid ounces	fl oz
L	liters	0.264	gallons	gal
m^3	cubic meters	35.314	cubic feet	ft^3 m^3
	cubic meters	1.307	cubic yards	yd^3
MASS				
g	grams	0.035	ounces	oz
kg	kilograms	2.202	pounds	lb
Mg (or "t")	megagrams (or "metric ton")	1.103	short tons (2000 lb)	T
TEMPERATURE (exact degrees)				
^oC	Celsius	1.8C+32	Fahrenheit	^oF
ILLUMINATION				
lx	lux	0.0929	foot-candles	fc
cd/m^2	candela/m^2	0.2919	foot-Lamberts	fl
FORCE and PRESSURE or STRESS				
N	newtons	0.225	poundforce	lbf
kPa	kilopascals	0.145	poundforce per square inch	lbf/in^2

*SI is the symbol for the International System of Units. Appropriate rounding should be made to comply with Section 4 of ASTM E380.
(Revised March 2003)

ACKNOWLEDGEMENTS

ABSTRACT FOR VOLUME 3

This report presents the numerical portion of the research project on the impacts of loading history on the behavior of reinforced concrete bridge columns. In well-detailed reinforced concrete structures, reinforcing bar buckling and subsequent bar rupture serve as common failure mechanisms under extreme seismic events. Engineers often use a strain limit state which is associated with bar buckling as the ultimate limit state, but the relationship between the strain demand and resultant bar buckling is not well understood. Past research has indicated large impact of the cyclic loading history on the strain demand to achieve reinforcing bar buckling. On the other hand, sectional analysis is widely implemented by engineers to relate strain to displacement. However, the cyclic load history also has potential impact on the relationship between strain limits and displacement limits. As a result, it is important to study the seismic load history effect on the strain limit state of reinforcing bar buckling and on the relationship between local strain and structural displacement. In addition, Performance-Based Earthquake Engineering (PBEE) strongly depends on an accurate strain limit definition, so a design methodology needs to be developed to identify the strain limit for reinforcing bar buckling including the seismic load history effect.

Two independent finite element methods were utilized to accomplish the goal of this research work. First, fiber-based analysis was utilized which employed the Open System for Earthquake Engineering Simulation (OpenSees). The fiber-based method was selected because of its accuracy in predicting strains and its computational efficiency in performing nonlinear time history analysis (NTHA). The uniaxial material models in fiber-based sections were calibrated with data from material tests. In addition, strain data and force-deformation response from large scale testing assists selection of element types and integration schemes to ensure accuracy. The advanced beam-column elements and material models in OpenSees resulted in a very accurate prediction of strain at local sections as well as global dynamic response of structures. A number of nonlinear time history analyses with 40 earthquake ground motions were conducted to investigate the effect of seismic load history on

relationship between structural displacement and strain of extreme fiber bars at the critical section.

The second finite element model was established with solid elements to predict bar buckling. The model included a segment of reinforcing bar and its surrounding elements, such as spiral turns and concrete. This model separates itself from previous bar buckling research by utilizing actual sectional detailing boundary conditions and plastic material models instead of the simplified bar-spring model. The strain history is considered as the demand on this model. A series of strain histories from the experimental tests and fiber-based analyses were applied to the finite element model to study their impacts on the strain limit for reinforcing bar buckling.

Initial analytical investigations have shown significant impact of load history on the strain demand to lead to reinforcing bar buckling in the plastic hinge region. This is also confirmed in the experimental observation which only included a limited number of load histories. The parametric study extended the range of load history types and also studied the effect of reinforcement detailing on bar buckling. On the other hand, analyses with fiber-based models showed that the load history rarely impacts the relationship between local strain and structural displacement. A design approach was developed to include the load history effect on the strain limit state of bar buckling.

TABLE OF CONTENTS

LIST OF TABLES

LIST OF FIGURES

LIST OF NOTATIONS

d_{bl} = Longitudinal Bar Diameter

d_h = Transverse Bar Diameter

Drift(%) = Drift Ratio

H = Column Height (same as column length)

K = Column Effective Length Factor

L_c = Column Length

Lp = Plastic Hinge Length

L_{SP} = Strain Penetration Depth

N_{2f} = Cycle of Loading

P_{cr} = Critical Buckling Force

P_T = Inelastic Critical Buckling Force

s = Transverse Bar Spacing

Δ_y = Column Yield Displacement

ε_c = Compressive Strain Limit for Bar Buckling

ε_t = Tensile Strain Limit for Bar Buckling

φ_y = Section Yield Curvature

Chapter 1: Introduction

1.1 Background and Scope

The research presented in this report represents the analytical portion of the load history research project funded by the Alaska Department of Transportation and Public Facilities and the Alaska University Transportation Center and is the third of three volumes. The experimental portion of the project (Volumes 1 and 2) has shown that load history has large impact on the strain limit related to reinforcing bar buckling. Therefore, finite element methods are utilized to specify different mechanisms of bar buckling under a variety of load histories. The details of finite element models are shown in Chapters 3 and 5. In addition, the impact of load history on the relationship between strain and displacement are investigated.

Presented in this volume of the report is a summary of the analytical modelling conducted as part of this research. This includes chapters on the role of fiber-modelling, finite element analysis, and finally a model for prediction of bar buckling for RC bridge columns.

In order to quantify the load history effect on the strain limits and the relationship between strain and displacement, the numerical method implemented should be able to capture the global non-linear behavior of a reinforced concrete bridge column as well as the local damage such as reinforcing bar buckling. In the case of investigating the load history effect on the relationship between strain and displacement, a finite element method with fiber-based elements was utilized because of its capability in providing strain information. In addition, as a simplified method compared to a finite element model with solid elements, the fiber-based model significantly reduces the computational cost of the nonlinear time history analysis (NTHA). This will allow a large number of NTHAs to be conducted with a variety of earthquake ground motions and RC columns. However, for the purpose of capturing local non-linear damage, especially reinforcing bar buckling, a portion of the plastic hinge region

is model with solid elements. Non-linear material behavior is determined by material tests and assigned to both finite element models.

1.2   Layout of Report

This report contains the following chapters: Chapter 2 contains a literature review; Chapter 3 introduces the fiber-modelling employed as part of this research program; Chapter 4 utilizes the fiber modelling of Chapter 3 to discuss the impact of load history on strain-displacement relationships; Chapter 5 Introduces the development of the FEA model for buckling; Chapter 6 utilizes the FEA of Chapter 5 to develop a model to predict bar buckling; and Chapter 7 are the conclusions of the analytical portion.

Chapter 2: Literature Review

2.1 General Discussion

This chapter will review the numerical methods to simulate the nonlinear response of RC members. In the case of global force deformation response of a concrete structure, a frame element is often utilized to model the RC member. Frame elements are defined on the basis of moment of inertia (bending and torsion), elastic modulus, and cross sectional area, among other parameters. In the case of nonlinear analysis, section hysteretic rules, such as the Modified Takeda Degrading Stiffness model (Otani (1974)), are defined to address non-linearity. However, if local behavior or damage is sought, a finite element method with solid or shell elements is utilized. Frame elements have apparent advantages in computational cost compared to a finite element models and it are often implemented in nonlinear time history analysis (NTHA). Nevertheless, engineers and researchers often acquire strain information in a NTHA to evaluate the damage under a seismic event. Fiber-based element models fulfill this requirement and also ensure reliable dynamic behavior as shown by Petrini et al. (2008).

2.2 Relevant Articles on Numerical Simulation

2.2.1 Fiber-Based Modeling of Reinforced Concrete Members

Fiber-based elements are able to provide strain information in an RC section which serve as an indicator of the damage limit state, such as longitudinal bar buckling. To investigate the seismic load history effect, it is convenient to utilize the fiber-based model for conducting NTHA and evaluating the structural performance with strain information. The research described in this report utilizes the Open System for Earthquake Engineering Simulation (OpenSees) to conduct analysis with fiber-based models.

Conventional frame elements utilize Euler-Bernoulli beam theory to distribute the lateral and axial displacement based on cubic Hermitian polynomials and linear Lagrangian shape

functions, respectively. Beam theory represents the exact solution for a deformed member with a linear distribution of curvature and constant axial strain. In structural members with higher order curvature and axial strain distributions, such as nonlinear RC members, the theory will fail to capture the actual structural behavior. Weiler (1990) and Neuenhofer (1993) stated that this limitation can be overcome with higher-order displacement interpolation functions in connection with internal element nodes. As a result, multiple displacement-based elements are required to model a nonlinear RC member.

Spacone et al. (1996), and Neuehofer and Filippou (1997) developed a new nonlinear frame finite-element based on force interpolation functions as opposed to the displacement fields or shape functions in traditional finite elements. The external force or moment distributions on a beam or column are often known in the typical engineering problem, such as the linear moment distribution under lateral loading in RC bridge columns. The actual distribution of force can be implemented as the force interpolation function directly without any further assumptions. As a result, the solution from the flexibility (force)-based element is exact for this force distribution. Since the flexibility-based elements are based on exact force interpolation functions, the solution involves limited numerical integration error even with a small number of elements or integration points. By contrast, the displacement interpolation functions deviate from the exact solution, so that a finer mesh with a large number of displacement-based elements is required to compensate for the assumption on displacement field.

Neuehofer and Filippou (1998) proposed the curvature-based displacement interpolation (CBDI) to enhance the functionality of the force-based element. This modification takes full advantage of the force interpolation field. Since the force distribution of a structural member is often known in actual engineering problems, only one force-based element with the exact force interpolation function is required. The CBDI allows locating multiple integration points within a force-based element to assess the high order deformation shape. Instead of multiple force-based elements, one element with multiple integration point allows the model to be

more efficient. The curvature-based interpolation procedure permits the consistent linearization of the governing compatibility equations for force-based elements.

The localization of response in reinforced concrete members modeled by continuum finite elements was studied by de Borst et al. (1994) and Bazant and Planas (1998). Similar to their findings, the displacement-based element approach also causes localization of response over a single element while the force-based element suffers from the localization of deformation at a single integration point. Scott and Fenves (2006) found that the strain softening behavior of concrete could cause a softening section in a fiber-based element. In this case, the localization of deformation in the force-based element is significant. To address this issue in the force-based element, Scott and Fenves (2006) developed a force-based element with adjustable integration weight at the ends of the element. The integration weight can be selected based upon the length of plastic hinges for the purpose of spreading the plasticity. A modified Gauss-Radau plastic hinge integration method was implemented in this force-based element to allow the control of the integration weight. The proposed element was recommended for the nonlinear analysis of frame structures when softening and degradation of the members is expected.

The approach of using one integration point to represent the plastic zone was adopted and improved by Lee and Filippou (2009). A new force-based element was developed to capture the development of the plastic zone depending on the moment gradient along the element. Figure 2.5 showes the inelastic zone length, which depends on a portion of the moment diagram where the moment magnitude exceeds the plastic moment capacity of the section. This method is able to capture the growth of the inelastic zone under incremental loading at the strain hardening section. However, a strain softening section during post peak behavior may not reach the plastic moment capacity of the section, but may still result in the spread of plasticity. Therefore, the approach using moment magnitude to define the extent of plasticity is not applicable with the strain softening section. Lee and Filippou (2009) then assumed the inelastic zone is fixed and time independent which is identical to Scott and Fenves' (2006) assumption.

As discussed, several methods have been developed to overcome the response localization in the force-based element with a strain softening section. However, these approaches fail to converge in the case of strain hardening response. In order to have a single element type which accurately predicts both strain hardening and softening behavior, Scott and Hamutcuoglu (2008) applied a numerically consistent regularization on the force-based elements. The force-based element was regularized by utilizing interpolatory quadrature with two integration points of prescribed characteristic lengths at the element ends. As shown in Figure 2.6, a standard quadrature rule (Gauss Lobatto) is modified with two additional integration points within the plastic hinges at each end. Scott and Hamutcuoglu (2008) showed that this regularization ensured the accuracy for strain softening sections and maintained a convergent solution for the spread of plasticity under strain-hardening behavior.

Alemdar and White (2005) studied the difference between displacement-based and flexibility-based elements. A mixed beam-column finite element formulation was also proposed for distributed plasticity analysis. Both the force field and displacement field were applied to the mixed beam-column element whose algorithm converts all residual displacements at the section and element levels to residual forces and then transfers them to the global level.

M_1

M_P

Bending Moment Diagram

Inelastic Zone

$L_{P,2}$

Node 1

Node 2

Elastic Zone

$L_{P,1}$

Inelastic Zone

M_P

M_2

L
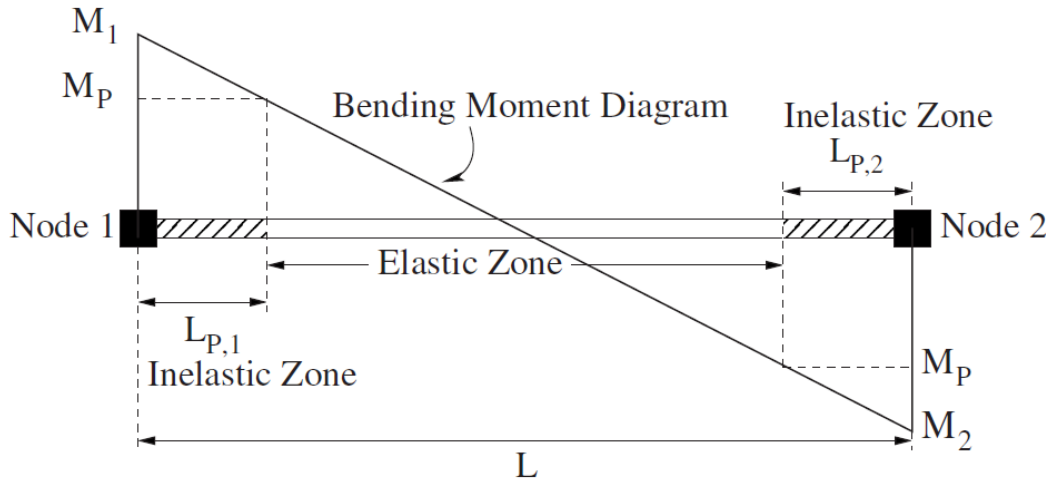
Figure 2.1 Sizes of Inelastic Zones in the Element from Lee and Filippou (2009)

$x_1 = 0$ $x_2 = 0.1727\,L$ $x_3 = 0.5\,L$ $x_4 = 0.8273\,L$ $x_5 = L$

$w_2 = 0.2722\,L$ $w_3 = 0.3556\,L$ $w_4 = 0.2722\,L$

$w_1 = 0.05\,L$ $w_5 = 0.05\,L$

(a)

x_1 ξ_I x_2 x_3 x_4 $L - \xi_J$ x_5

$w_{\xi I} =$

$0.05\,L - l_{pI}$ Locations $x_1 - x_5$ same as above $w_{\xi J} =$

$0.05\,L - l_{pJ}$

$w_1 = l_{pI}$ $w_2,\ w_3,\ w_4$ from solution to Equation (13) $w_5 = l_{pJ}$

(b)
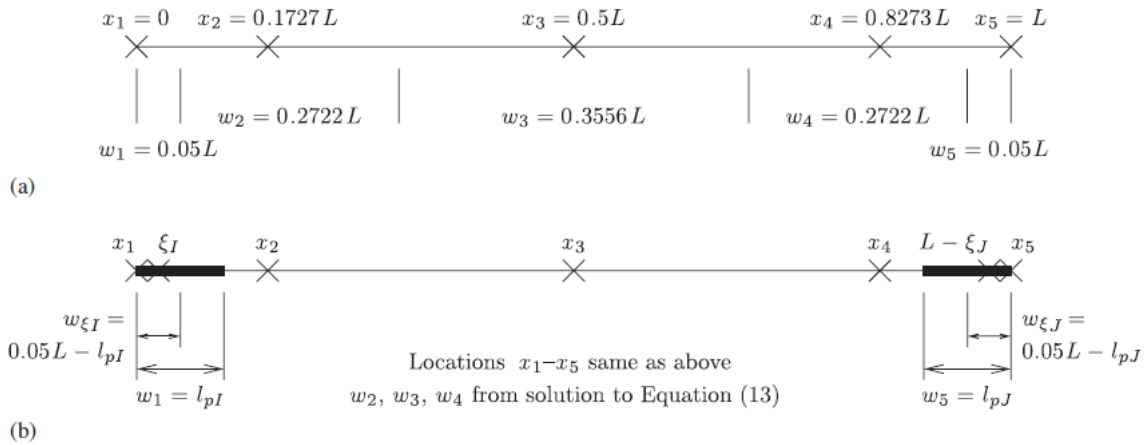
Figure 2.2 (a) Standard five-point Gauss–Lobatto integration rule and (b) five-point Gauss–Lobatto rule regularized by addition of two integration points just inside the element ends from Scott and Hamutcuoglu (2008)

2.2.2   Finite Element Method for Reinforcing Bar Buckling

It is difficult to numerically simulate a RC structural member including the inelastic buckling of reinforcing bars. Modeling localized nonlinear behavior and the complicated boundary conditions as well as its interaction with the reinforcing bar requires extensive computational effort. Convergence failure often occurs during the analysis. However, the localized behavior must be simulated appropriately to study the effect of loading history and sectional detailing on bar buckling. Numerous modeling approaches have been developed to capture bar buckling in previous studies. Mau and El-Mabsout (1989) developed a beam-column element to carry out inelastic analysis of reinforcing bars to generate the stress-strain behavior of buckled bars. Dhakal and Maekawa (2002) utilized the fiber-based technique in the finite element method to establish the average stress-strain relationship including post buckling behavior. Masukawa et al. (1999) presented the bar buckling model in which a beam-column element simulated the bar, and springs modeled the boundary condition at the hoops. The stress-strain behavior including bar buckling was implemented in a 3D finite element column model where the reinforcement and concrete were simulated with shell elements. Zong and Kunnath (2008) compared the stress-strain behavior of reinforcing bars in both a full column finite element model and an independent bar-with-springs model. Bar buckling over multiple spiral gauges was considered in this study. However, the full column finite element analysis assumed the concrete to be elastic which is fails to capture the plastic elongation of core concrete under compression. Calladine (1972) and Bae et al. (2005) both studied the impact of imperfections on inelastic bucking of longitudinal bars. An analysis of local bar buckling was conducted by Urmson and Mander (2012) to precisely predict the average stress and strain relationship after buckling. The ratio of hoop spacing and bar diameter was found to affect the crippling strength of a buckled bar which was governed by the compressive plastic ultimate strength of the bar section and the eccentricity of the bar respectively.

In most cases, the goals of these studies are to investigate the effect of reinforcing bar buckling on stress-strain behavior, or the force-deformation response of the structural

member. Independent bar buckling models were developed to include the post-buckling behavior on the stress-strain relationship. The typical modeling approach simulated the bar with one or multiple beam-column elements with fixed ends and converted the hoops or spirals to springs to restrain out-of-plane deformation. The beam-column elements behaved uniaxially until the buckling load was reached. The out-of-plane deformation activates the restraining spring. Therefore, the buckled bar retains load carrying capacity because of the presence of the lateral restraint. These models provided a general idea of the post buckling behavior and a coarse prediction of buckling load in some cases, but the simplified boundary conditions do not consider the dilation of the concrete core and its effect on bar buckling. In addition, the effect of cyclic load history and reinforcement detailing, such as spacing of hoops and bar diameter, has not been quantified.

2.3 Chapter Summery

Past research has shown that the bar buckling is a common damage mechanism in RC bridge columns and the load history has obvious impact on the deformation limit state for bar buckling. However, the effect of seismic load history on the strain limit for bar buckling and the relationship between strain and displacement has not been quantified. As a result, the research discussed in this report focuses on defining the impact of the seismic load history on the relationship between strain and displacement as well as the bar buckling strain limit itself. Fiber-based and finite element models are developed and utilized to conducted analysis.

Chapter 3: Fiber-Based Modeling of Circular Reinforced Concrete Bridge Columns

3.1 Introduction and Background

The ability to predict the non-linear response of reinforced concrete structures is essential to meet the objective of performance-based seismic design. As a result, several methods have been used for the nonlinear analysis of reinforced concrete bridge columns, ranging from simple hand calculations, to frame element analysis, fiber-based element analysis, and solid/shell based finite element analysis. In the case of fiber-based analysis, the primary advantage is the local strain information that it provides at relatively low computational cost. Such information is important for Performance-Based Earthquake Engineering where the objective is to control structural performance (usually defined on the basis of strain) under prescribed seismic events. However, in order to implement fiber-based analysis, several modeling choices must first be made, and the implications of each fully understood.

Discussed in this chapter is a brief primer on fiber-based modeling theory followed by a discussion of force and displacement-based elements. A method is then proposed for predicting the strain gradient in plastic hinge regions using the modified compression field theory. The subsequent section then discusses the importance of including strain penetration in the analysis model. The last section of the chapter demonstrates the accuracy of combining force-based elements, strain penetration elements, and the proposed strain gradient prediction method for accurate assessment of strain profiles in the plastic hinge region of bridge columns. The accuracy of the model to predict overall force-deformation response is also presented. All fiber-based analysis results in this chapter were conducted using the Open System for Earthquake Engineering Simulation (OpenSees).

Some of the experimental data referenced later in this chapter was obtained from physical column tests conducted at North Carolina State University (Goodnight et al., 2012) as part of the large research program on the impact of load history on the behavior of reinforced concrete bridge columns (see companion volumes of this report). Through the implementation of an optical 3D measurement system (Optotrak), it was possible to obtain the engineering strain in the longitudinal reinforcement in the tests well into the nonlinear range. A series of LED markers were attached to the exposed reinforcement and the sensors (Optotrak cameras) captured the movement of the LED markers in 3D space. The elongation between two LED markers was utilized to calculate the average strain in each gauge length. This technique provides strain histories along the longitudinal direction of the bar. However, there are two basic assumptions in the strain calculation with Optotrak data: (1) the longitudinal reinforcement behaves uniaxially and (2) significant localization of strain does not occur inside one gauge length. Therefore, the strain calculated from Optotrak data are not considered to be valid after bar buckling or necking occurs. The Optotrak system and its operating mechanism are displayed in Figure 3.1.
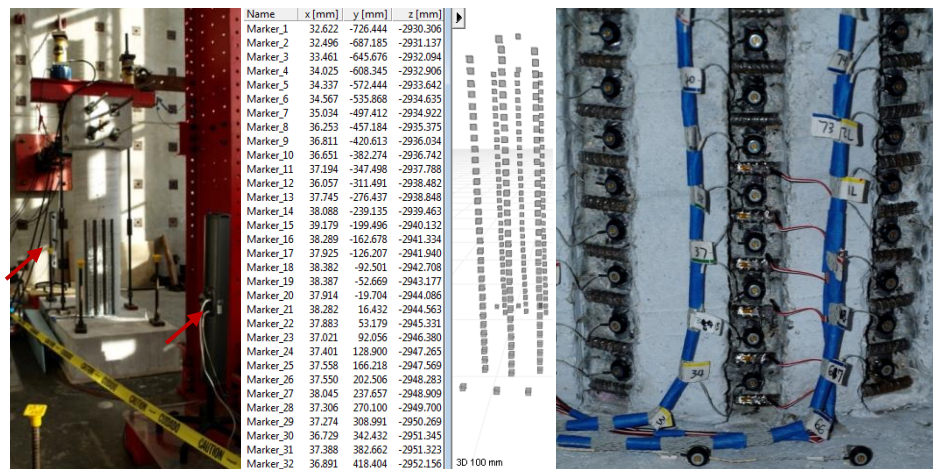
Figure 3.1. The dual camera Optotrak system, coordinate system, and LED markers on the reinforcement

3.2 Theory of Fiber-Based Modeling

Fiber-based analysis is well established for modeling structural members undergoing primarily flexural deformation. The difference between fiber-based elements and frame elements lies in the method to define the global structural behavior. Frame elements are defined on the basis of moment of inertia (bending and torsion), elastic modulus, and cross sectional area, among other properties. In the case of nonlinear analysis, section hysteretic rules, such as the Modified Takeda Degrading Stiffness model (Otani, S. (1974)) shown in Figure 3.2, are defined to address non-linearity. In the case of a fiber-based element, the cross section is divided into a series of fibers that follow prescribed constitutive relationships. As a result, the global force-deformation behavior of a fiber-based element depends on the individual material responses. A key advantage of fiber-based elements is that strain, stress, and curvature can be directly obtained whereas they may only be inferred with frame analysis.
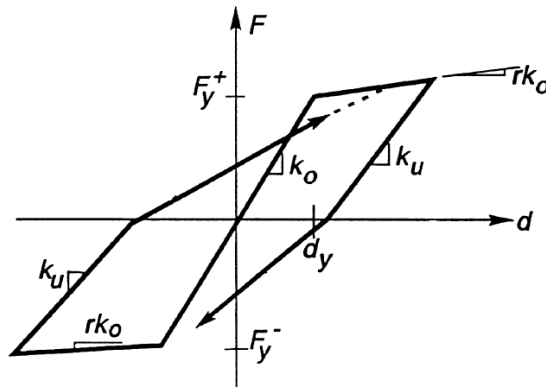
Figure 3.2. Modified Takeda Degrading Stiffness (Otani (1974)) Force-Deformation Response for RC Beams and Columns (drawing from Carr (2007))

For the convenience of users, OpenSees provides a number of community developed constitutive models. A few parameters, such as steel yield strength and concrete compressive strength, are usually required to define both monotonic and cyclic stress-strain behavior. For this research, the steel model developed by Filippou, et al. (1983) and the concrete model developed by Yassin (1994) were selected for analysis. The steel material allows the user to control the cyclic behavior by defining a pair of hardening ratios in addition to an adjustable yield strength and elastic modulus. The concrete constitutive model has an inherent cyclic behavior which depends on user defined strength parameters.

Fiber sections are assumed to remain plane throughout the analysis. For reinforced concrete, sections are divided into a number of concrete and steel segments as shown in Figure 3.3. Strain compatibility between reinforcement and the surrounding concrete is assumed. The sectional deformations consist of a moment and axial load resultant from the sectional deformations, including axial strain at the center of the section and the curvature. A unique solution of this deformation combination will be obtained based on a cyclic sectional analysis.
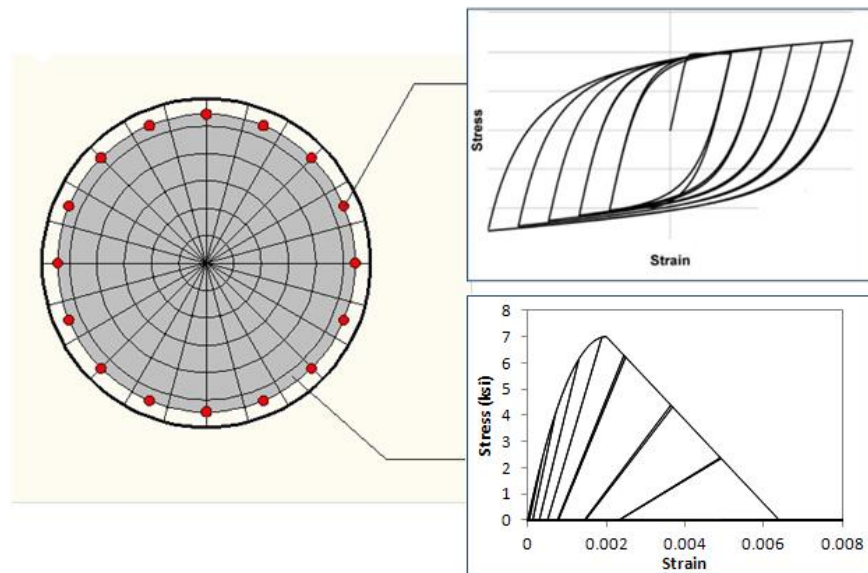
Figure 3.3. Material Fibers in a Section

To establish a fiber-based element, a number of fiber-based sections are spread along the length of the element with each section located at an integration point. A predefined interpolation function of the force or the displacement is required to convert the global demand to sectional demands, which will be in terms of sectional moment or curvature demands. The sectional responses will be calculated, and then integrated to obtain the global response which will be either deformation or the reaction force. Therefore, the accuracy of the fiber-based element depends on 1) the force or displacement interpolation function 2) and the order of exact integration of the integration scheme which relates to the number and location of integration points.

The integration scheme determines the locations of integration points where fiber sections are placed. In addition, the integration scheme is utilized to obtain either the global stiffness or flexibility matrix along with the interpolation function based on the displacement or force field. The type of integration scheme and the number of integration points determine the degree of polynomials up to which the numerical integration is exact. Various integration schemes are available in elements, including the Gauss-Lobatto, Gauss-Legendre, Gauss-Radau integration (Hildebrand (1974)).

Fiber-based elements are separated into two categories depending on the interpolation functions used. The force(flexibility)-based element utilizes the force interpolation function to distribute the nodal concentrated force to each section where a moment and axial force are assigned. The sectional response is then obtained in terms of a combination of axial strain and curvature. Subsequently, the curvature and axial strain are integrated to obtain the lateral displacement and axial elongation. In an engineering problem, the distribution of the force and moment are often known. For the case of seismic forces in bridges, the distribution of bending moment is triangular with a point load at the center of the superstructure (usually, inertia weight of the columns is either ignored or a portion of it is combined with the superstructure weight). The force-based element utilizes this linear load distribution to obtain the loading demand at each section. Therefore, there is no assumption on the force

interpolation function and equilibrium is satisfied at each section and end node. On the other hand, the displacement-based element applies a displacement shape function to distribute the nodal deformation to each section. As a result, each section will be forced to accommodate the tributary deformation. Each section will react with the moment and axial load. The global force will be obtained by extrapolating the sectional force to the node. A shortcoming of displacement-based elements is that the displacement shape function may not reflect the real deflected shape of a structural component. As a result, a finer mesh is often required with multiple displacement-based elements to increase the accuracy of the deformation shape. Moreover, equilibrium is only satisfied at the nodes and the distribution of moment along the column element is not ensured to be linear as it is in a bridge column.

The displacement-based element utilizes a displacement interpolation function to distribute the nodal deformation along the element length. The nodal force is related to sectional behavior by integrating the sectional stress along with the interpolation function. Equilibrium is satisfied by a weighted integral sense as expressed in Eq. 3.1 from Alemdar and White (2005).

$$\int_0^L \mathbf{N}(x)^T \mathbf{D} dx - \mathbf{Q} = \mathbf{0} \qquad 3.1$$

$\mathbf{N}(x)$ is constructed with the displacement interpolation functions. Matrix $\mathbf{D}$, $\mathbf{Q}$, and $\mathbf{L}$ are the stress-resultant section force, the external force at the nodes, and the length of the element respectively. Neuenhofer and Filippou (1998) proposed the force-based element where a prescribed force field is assigned instead of the displacement interpolation function. The element adapted a governing compatibility equation derived from the principle of virtual work as shown in Eq. 3.2 Alemdar and White (2005).

$$\int_0^L \mathbf{N}_F(x)^T \mathbf{d} dx - \mathbf{q} = \mathbf{0} \qquad 3.2$$

$\mathbf{N}_F(x)$ represents the force interpolation functions, the sectional strain is represented by $\mathbf{d}$, and the matrix $\mathbf{q}$ is referred to as the nodal displacement. Curvature-Based Displacement Interpolation (CBDI) was used to account for geometric nonlinear effects. At a coarse mesh

level, the CBDI method ensures that the distribution of deformation has a relatively high order of accuracy.

The force-based element satisfies equilibrium on a section-by-section basis. The force-based element, however, suffers from localization of deformation under strain-softening behavior which results in the response changes as a function of the number of integration points. The reinforced concrete section in fiber-based element tends to exhibit localization of deformation because of the post-peak softening of concrete and low post-yield hardening of steel. The force field in the element causes the maximum moment to always be located at the same section. In the extreme load case, the critical section may deform to pass the peak capacity point while other sections are still approaching the peak. This will cause continuous softening of the critical section and will prevent other sections from reaching their peak capacity. Consequently, the deformation will concentrate at the integration point associated with the critical section. The computed response is determined by the spread of the deformation implied by the integration weight. As discussed, a unique solution does not exist and is mesh dependent. In general, the force-based element sacrifices the inter-sectional compatibility to enforce the inter-sectional equilibrium. There is no compatibility restriction on the deformation gradient between two adjacent sections.

Alemdar and White (2005) stated that the displacement-based element satisfies equilibrium in a weighted integral sense at element nodes only. The imposed linear curvature field in the element is an assumption which may not capture the real behavior in structural components. To compensate for this potential shortcoming, a fine mesh with multiple elements is usually required for the displacement-based element thus increasing the computational cost. However, localization of deformation could also occur in the case of modeling one structural member with multiple displacement-based elements. The nodal displacements at each element satisfy compatibility and continuity while a displacement field is also imposed within a single element. However, there is no inter-element restriction on sectional deformation. Therefore, the curvature could also concentrate in a single displacement-based element while the sections have strain softening responses. As a result,

this requires special awareness on the number of displacement-based elements and number of integration points of a force-based element while modeling a reinforced concrete member.

To evaluate the accuracy of both force and displacement-based elements, the analytical results are compared to test data. The experiments include a series of cyclic column tests subjected to controlled reversed cyclic loading as well as real earthquake time histories. The reinforced concrete columns were 8 ft (2.44m) in height and 2 ft (0.61m) in diameter. The reinforcement consisted of 16 0.75 in (19mm) diameter bars and a 0.375 in (9.5mm) spiral at 2 in (51mm) pitch. As shown in Figure 3.4, the force-based element, denoted FB, generates a better prediction of the force-deformation relationship for a cyclic test result. It is also observed that the displacement-based element, denoted DB in Figure 3.4, overestimates the strength of the specimen. Though a finer mesh with multiple displacement-based elements can improve the accuracy, an over-meshed model can also lead to localization of the deformation at a single element.

The force-based element was selected because of its accuracy in predicting the force-deformation response of the specimen. However, there are multiple variations of force-based elements. One such element (termed 'beam with hinges') was developed by (Scott and Fenves (2006)) to overcome the 'loss of objective' problem. The 'beam with hinges' element utilizes a plastic hinge integration method which defines the integration weight of the critical section with a plastic hinge length. The element involves a modified Gauss-Radau integration rule where the weight of the end integration point is adjustable, as shown in Scott and Fenves (2006). A numerically consistent regularization is placed on the force-based element by Scott and Hamutcuoglu (2008) to resolve the dichotomy of the solutions from strain hardening and strain softening problems. This method will increase the accuracy when modeling a structural member with unknown sectional behavior or different post-yielding sectional behavior from one member end to the other end. Lee and Filippou (2009) proposed an element which has variable inelastic end zones. Similar to the 'beam with hinges' element, its inelastic zone at member ends is represented by the characteristic length of the end integration point, which will vary depending on the magnitude of moment distribution.
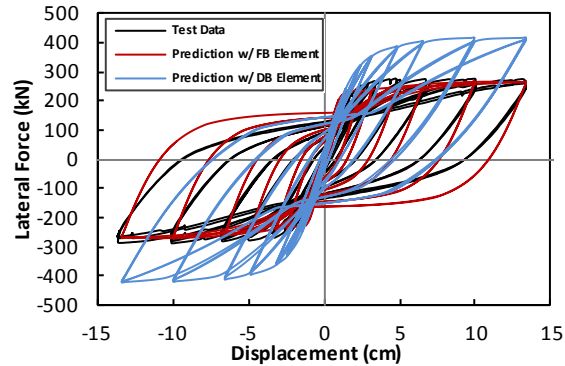
Figure 3.4. Comparison between model predictions and test data

3.3 Proposed methods for simulating RC bridge columns

3.3.1 Experimental Observation

It is usually not suggested to place multiple integration points in the plastic hinge region for a force-based element due to potential strain-softening behavior of the concrete section. Localization of deformation in RC members modeled by the finite element method was discussed by Borst et al. (1994) and Bazant and Planas (1998). Scott et al. (2004) stated that three to five Gauss-Lobatto integration points along the element would accurately represent the material nonlinear behavior, which results in using one integration point to represent the behavior of the plastic hinge. However, the distribution of strain in the plastic hinge region is not available without multiple integration points. Considering the case with a strain-hardening section, such as a circular RC section, nine Gauss-Lobatto integration points were placed along the element. In addition, a strain penetration model serves as an extra 'integration point' at the end of the element. The strain penetration model is discussed later in this chapter. A post-processing method of the strain information was proposed to include the

"tension shift effect", described below and illustrated in Figure 3.5, on the distribution of strain and its application on post-processing strain data from a fiber-based model.

The strain profile in the reinforcement within the plastic hinge region was obtained with the Optotrack 3D position measurement position measurement system. Figure 3.6 displays typical strain profiles at different displacement ductility levels where the compressive strain is usually lumped at the bottom of the column, but the tension strain fans out and extends to a section higher up in the column. This type of strain distribution occurred consistently during all column tests. It is believed that the tension shift effect causes the strain on the tension side of a flexural member to spread to higher levels without influencing the compressive strain.
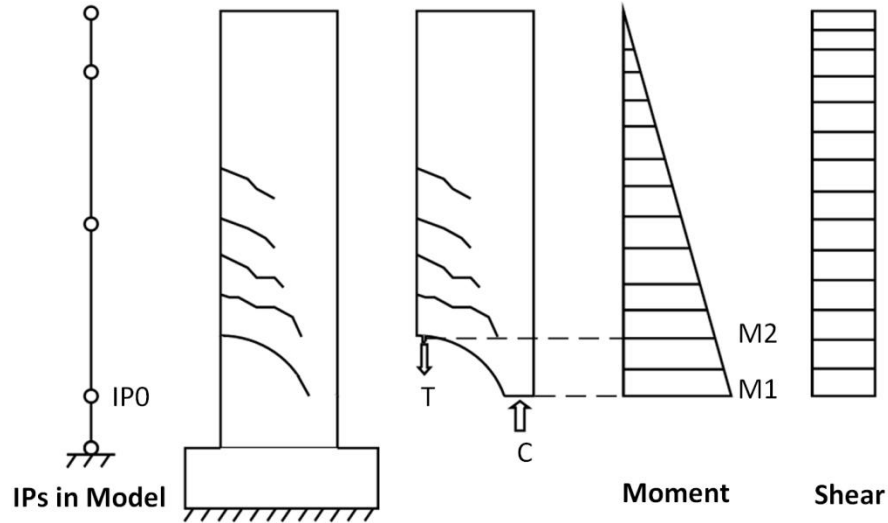
Figure 3.5. Tension Shift Effect
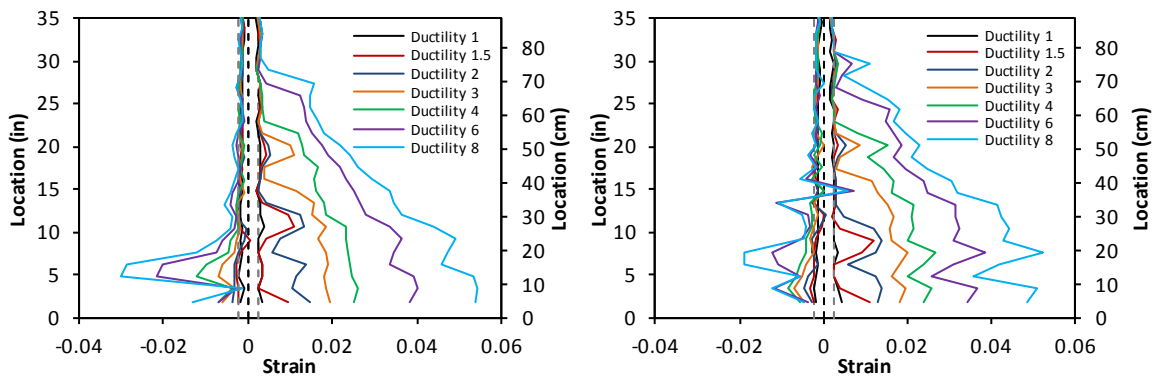
Figure 3.6. Strain Profiles of Longitudinal Reinforcement in Plastic Hinge Region

Figure 3.7 shows the propagation of the inclined flexure-shear cracks for increasing levels of displacement ductility. A free body diagram is established along an inclined flexural-shear crack in Figure 3.5. The moment is linear and shear is uniform along the length of the column. The inclined flexural-shear crack results in a cracked inclined section

where the tensile zone is higher than the compressive zone. To maintain moment equilibrium of the free body, the tensile force from the reinforcement is related to the moment at the height of the compressive zone which refers to M1 instead of M2 in Figure 3.5. This causes a concentration of the compressive strain at the lower level of the column while the tensile strain propagated further up the column as shown in Figure 3.6.
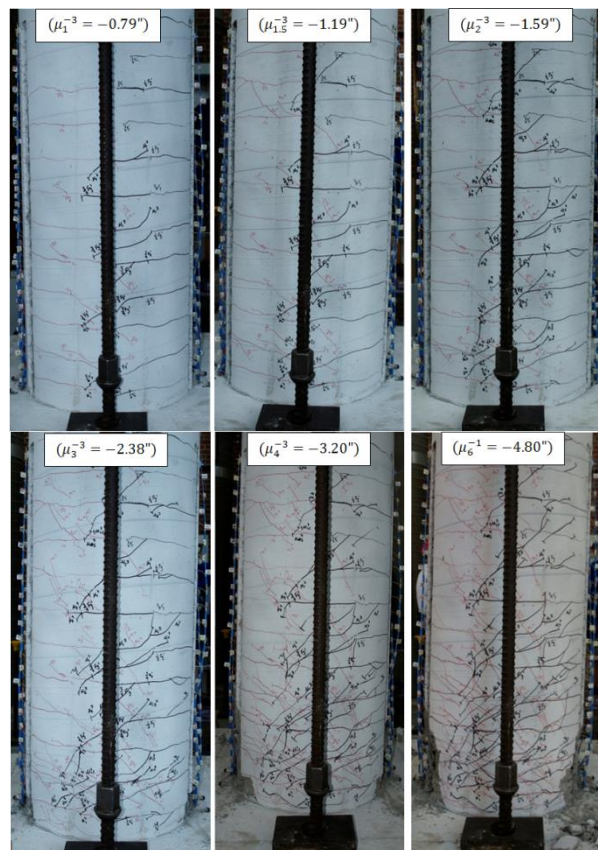
Figure 3.7. Crack Propagation from Experimental Tests Conducted at NCSU

In the force-based element the predefined force interpolation function governs the moment and the axial load at each integration point. Sectional analysis provides resultant deformations due to this moment and axial load distribution. As shown in Figure 3.5, assuming an integration point IP0 is located at the same level of the compressive zone of the

inclined section, sectional analysis will provide strain at the extreme tension fiber bar according to the magnitude of M1. However, the predicted strain represents the behavior of the longitudinal rebar at a higher level than the location of IP0. Therefore, the section at IP0 provides compressive strain at its level and tensile strain at a higher column level.

It is well established that the cracking angle is required to quantify the tension shift effect. It has been observed that for a flexural member, the crack angle varies from the tensile side of the column to the compressive side of the column. At any specific point of the crack, the direction of the principal tensile strain depends on the combination of the longitudinal strain component from flexural behavior and the shear strain component. A simple example is the horizontal crack at the extreme tensile fiber which is caused only by the large uniaxial strain from flexure. However, as the crack propagates into the mid-section, shear stress increases while the tensile strain decreases. Therefore, cracks become steeper at the center of a column, as shown in Figure 3.7.

3.3.2 Proposed Method to Predict Strain Gradient

Crack angles vary due to the unique strain condition at each location of the section. The Modified Compression Field Theory (MCFT) developed by Vecchio and Collins (1986) is utilized to compute the crack angle distribution along the section. Vecchio and Collins (1988) utilized lay-up analysis to calculate the shear strength of a shear member. The MCFT is utilized in this chapter since it accounts for impact of the longitudinal and transverse reinforcement on the cracking angle of concrete. Sectional analysis is conducted to obtain a strain distribution along the section. A shear stress distribution will be assumed based on the flexural behavior. A combination of the strain distribution and the shear stress distribution will be applied to the section, as shown in Figure 3.8. A unique solution of the crack angle distribution can be obtained which will be integrated to derive the tension shift height in an inclined section. To apply this method, the following assumptions are made.

1. The influence of flexural-shear interaction on sectional analysis is neglected.

2. Cracks propagate from extreme tensile fiber to the neutral axis of a flexural section.

3. No bond slip between the concrete and the reinforcement occurs (from MCFT).

4. Both longitudinal and transverse reinforcing bars are uniformly distributed over the element (from MCFT).

Several modifications were made to the method from Vecchio and Collins (1988) to increase the accuracy of the crack angle prediction. First, the longitudinal strain is used as the demand instead of reinforcing bar stress. Cracking of concrete occurs when the principal strain exceeds the cracking strain. As a section deforms into nonlinear range, stress in the reinforcement may not vary significantly while the strain will keep increasing with the deformation. Therefore, it is more reliable to utilize the strain for the crack angle calculation. Second, the three point Gauss-Legendre integration scheme is utilized to reduce the computational effort. Crack angles of the section in three locations from the extreme tensile fiber to the neutral axis are derived. Locations and weights of integration points are determined by the Gauss-Legendre rule. The complete procedure to calculate the tension shift height is shown in Figure 3.9.
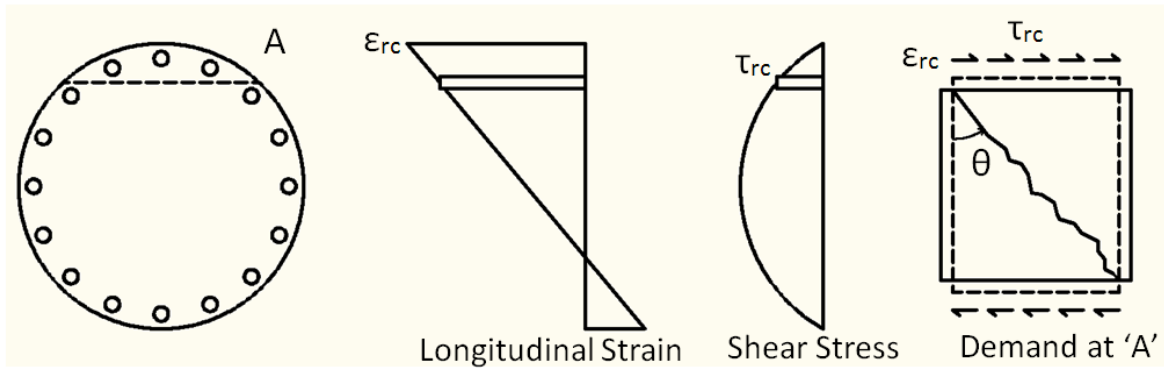
Figure 3.8. Crack Angle θ from Longitudinal Strain and Shear Stress at Location 'A' of a Section

```
┌─────────────────────────┐
│  Determine moment demand │
│      of the section      │
└─────────────────────────┘
            │
            ▼
┌─────────────────────────┐              ┌─────────────────────────┐
│ Conduct sectional analysis│             │  Determine shear demand  │
└─────────────────────────┘              │      of the section      │
            │                            └─────────────────────────┘
            ▼                                        │
┌─────────────────────────┐                          ▼
│  Obtain longitudinal strain│             ┌─────────────────────────┐
│      distribution        │              │    Assume a shear stress │
└─────────────────────────┘              │      distribution        │
                                         └─────────────────────────┘
```

Figure flowchart:

- Determine moment demand of the section → Conduct sectional analysis → Obtain longitudinal strain distribution
- Determine shear demand of the section → Assume a shear stress distribution
- → Select an IP and obtain its associated longitudinal strain and shear stress demand
- Select another IP →
- Utilize MCFT to obtain crack angle
- Integrate crack angles on the tensile side of section to obtain tension shift height

Figure 3.9. Method of Predicting Tension Shift Height

The purpose of obtaining the tension shift height is to then allow the prediction of tensile strain gradient in the plastic hinge region. Fiber-based models provide longitudinal strain information at each section. The strain and the assumed shear stress at the three sectional integration points are extracted. A unique combination of shear stress and longitudinal strain at each point will results in a unique crack angle under MCFT. Three crack angles, θ_1, θ_2 and θ_3, are derived for each fiber-based section. The tension shift height can be calculated utilizing Eq. 3.3 and 3.4 where w_1, w_2, and w_3 are the integration weights of the angles

respectively. H_{ts}, D_C, and C represent tension shift height, column diameter and neutral axis depth of a section respectively. For the convenience of calculating the tension shift height, this chapter uses the angle between crack and longitudinal direction, as shown in Figure 3.9.

A deformation gradient can be established with multiple element integration points placed in the plastic hinge region. Sections along the force-based element directly provide multiple points on the distribution of compressive strain. The tensile strain distribution can then be obtained by considering the tension shift effect. The implementation of this method will be shown later.

$$H_{ts} = \int_0^{D_C-C} \tan\theta dx = w_1\cot\theta_1 + w_2\cot\theta_2 + w_3\cot\theta_3 \qquad 3.3$$

$$D_C-C = w_1 + w_2 + w_3 \qquad 3.4$$

3.3.3 Method to Include Strain Penetration

Cracking was observed on the footing surface during experimental tests as expected and shown in Figure 3.10. When the column was subjected to large flexural deformation, a crack initiated near the tensile side of the column. This is due to the strain penetration of the longitudinal reinforcement into the footing. Because the longitudinal reinforcement has large tensile strains in the plastic hinge region, a strain gradient will exist inside the footing to allow the reinforcement strain to maintain strain compatibility. Globally, the reinforcement will slip from the footing by a certain amount of displacement which depends on the strain gradient level in the footing. A small portion of the footing surface concrete, which is bonded to the reinforcement, cracks to accommodate this bond slip displacement.

In experimental tests, the bond slip displacement of reinforcement can be obtained by monitoring the vertical movement of the LED markers. Figure 3.11 portrays the bond slip hysteretic response at the lowest LED marker level on the reinforcement. Since the monitored marker is located about 1.0 in (25.4 mm) above the footing surface, the bond slip displacement may include a portion of plastic elongation of the reinforcement.
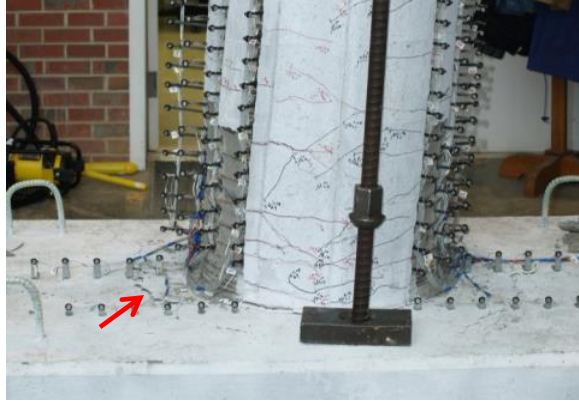
Figure 3.10. Crack on the footing near the tension side
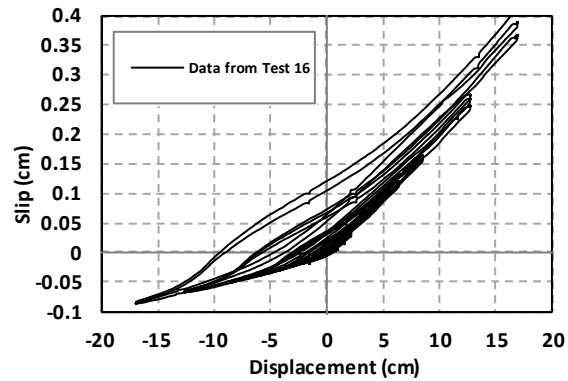
Figure 3.11. Bond slip hysteretic response

In the fiber-based analysis, a zero length section element is located at the base of the column element to include the bond slip behavior, as presented in Figure 3.12. The zero length element serves as a nonlinear rotational spring which accounts for the additional rotation at the base column section due to bond slip. The behavior of the zero length element depends on the associated fiber section. The fiber section consists of regular concrete fibers and special reinforcement fibers which are represented by a bond slip material. Zhao and Sritharan (2007) developed the bond slip material which implemented a stress-slip relationship to account for strain penetration. Both monotonic and cyclic stress-slip relationships were developed on the basis of experimental tests results. The bond slip is represented by the slip displacement in the material which depends on the stress in the reinforcement, as shown in Figure 3.13. Zhao and Sritharan (2007) had shown the bond slip material's highly accuracy on predicting the debonding behavior of reinforcement.
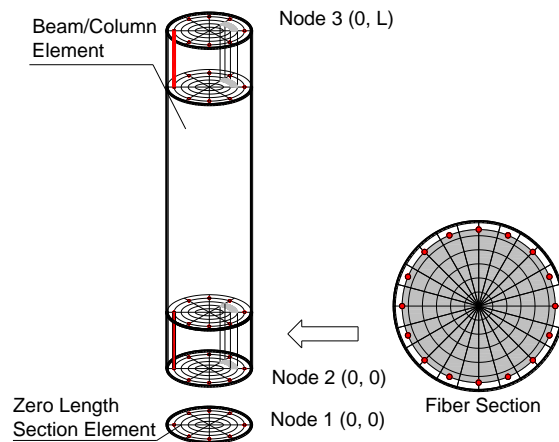
Figure 3.12. Model Lay-out with the zero section element
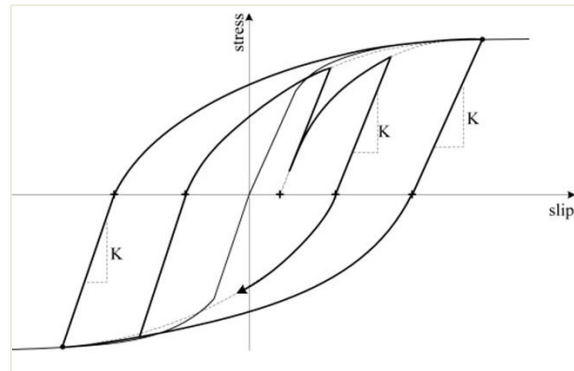
Figure 3.13. Stress-slip relationship from Zhao and Sritharan (2007)

3.3.4 Benchmark Method to Capture Nonlinearity in RC Member with Fiber-Based Model

A common approach to capture nonlinearity in reinforced concrete members is to use the plastic hinge integration methods, as developed by Scott and Fenves (2006). The plastic hinge integration methods lumps the plasticity at a single integration point which is often at the end of the element, as shown in Figure 3.14. This method is very reliable for obtaining force-deformation response and maximum strain since it avoids the localization of plasticity – a common problem in simulation of RC members. A typical plastic hinge integration method – 'beam with hinges' element is selected to be the benchmark method because it is computationally efficient and dynamically robust, as shown later in this chapter. The model with nine integration point force-based element is evaluated by comparing its performance to this benchmark method. To reduce the computational cost, an elastic region is defined at the interior portion of the 'beam with hinges' element. The elastic properties, such as elastic modulus, cross sectional area and moment of inertia, are required within the interior region. It has been observed in the experimental tests that cracked regions cover most of a reinforced concrete column. As a result, a cracked section moment of inertia was used to model the elastic portion of the element.
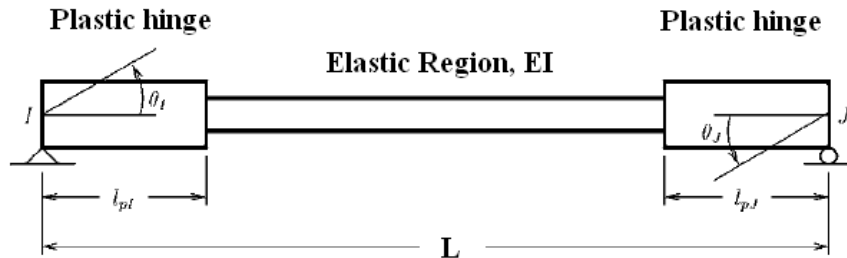
Figure 3.14. Beam with Hinges Element from (M. Scott and F. Fenves (2006))

3.4 Calibration and Application of the Fiber Model

Two independent fiber-based models were established both of which combine a force-based column element and a zero length section element for the strain penetration. One of the models utilized a nine integration point force-based element for the purpose of obtaining distributed plasticity in the plastic hinge, while the other model implemented the 'beam with hinges' element. The material constitutive models were calibrated with recorded data from material tests. Predictions of large-scale static column tests, and shake table tests were conducted. The model combining the 'beam with hinge' element and strain penetration simulation is the solution with high computational efficiency in predicting the force-deformation response, maximum strain at the critical section, and dynamic response. Its performance was assessed with test data. However, to produce the strain distribution in the plastic hinge region, the reinforced concrete column is simulated with the nine integration point force-based element (Gauss-Lobatto integration). The strain data was then post-processed to provide the strain gradient within the plastic hinge.

3.4.1   Calibration on Material Constitutive Models

A number of bar cyclic tests were conducted to ensure proper steel material behavior modeling. The steel constitutive material model from Filippou et al. (1983) was defined with the yield strength of 68 ksi (469 MPa) from monotonic material test result. The tensile and compressive hardening ratio in the steel model is adjusted to ensure the prediction matched the cyclic bar test result, as illustrated in Figure 3.15. The concrete compression strength was obtained from cylinder tests. The monotonic behavior of confined concrete was derived with the stress-strain model proposed by Mander et al. (1988). The concrete cyclic behavior was simulated using the constitutive model developed by Yassin (1994), as presented in Figure 3.16. The tensile strength of concrete was neglected.
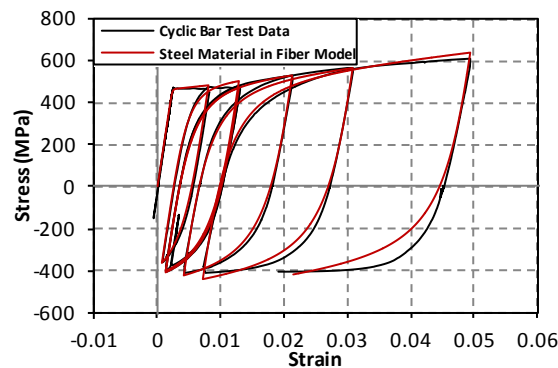
Figure 3.15. Comparison of steel Material behavior in fiber model and tests
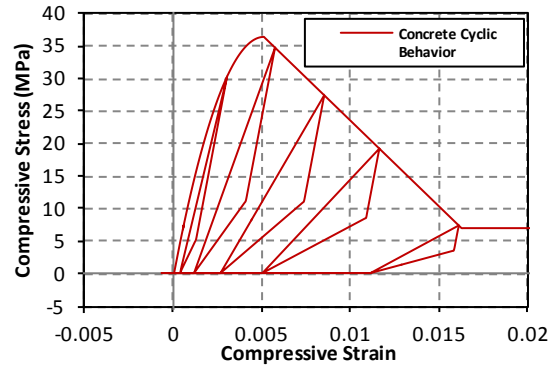
Figure 3.16. Cyclic behavior of unconfined concrete

3.4.2 Prediction on Force and Strain from Static Tests

Both models were utilized to predict test data from the eighteen column tests where the strain information is available up to reinforcement buckling. Definition of bond slip material in the zero length element ensures appropriate moment capacity compared to the column section. With the bond slip material, the zero length section element allows the correct amount of deformation to propagate into the element and avoids localization of deformation at the strain penetration model. In the case of a strain penetration model with underestimated strength, most of the deformation will migrate into the zero length section element. Therefore, the fiber-based model could underestimate curvature and the resultant strain at the plastic hinge of the column element.

The plastic hinge length controls the extent of plasticity in the 'beam with hinges' element. The plastic hinge length can be specified by an empirical relationship proposed by Priestley et al. (2007), as shown in Eq. 3.5 to 3.7

$$L_{SP} = 0.022 f_y d_{bl} \qquad\qquad 3.5$$

$$k = 0.2\left(\frac{f_u}{f_y} - 1\right) \leq 0.08 \qquad\qquad 3.6$$

$$L_P = kL_C + L_{SP} \geq 2L_{SP} \qquad\qquad 3.7$$

where L_{SP}, L_P and L_C are the strain penetration length, the plastic hinge length, and the column length, f_y, f_u and d_{bl} are yield strength in MPa, ultimate stress in MPa and diameter of longitudinal reinforcement in mm respectively. Shown in Figure 3.17 is the comparison of force-deformation responses of the fiber-based model using the 'beam with hinges' element and bond slip model, with test data from a 3-cycle-set load history and three earthquakes (

Table 3.1). Information on the experimental tests is listed in Table 1. The section-by-section-based equilibrium in the force-based element ensured an accurate prediction of response. The bond slip model contributes to the proper unloading and reloading stiffness of the model. However, the cycle to cycle strength degradation in the 3-cycle-set is not captured because of the absence of the cumulative damage in concrete. Figure 3.18 shows the predictions from the proposed model which has a force-based element with nine integration point as well as a zero section element. This model also has robust nonlinear behavior.

Table 3.1. Test Information

Test	Load History	D (mm)	L/D	Long. Steel (ρ_l)	Spiral Detailing (ρ_s)
9	3-Cycle-Set	610	4	16 #6 bars (1.6%)	#3 at 2" (1%)
10	Chichi 1999	610	4	16 #6 bars (1.6%)	#3 at 2" (1%)
11	Kobe 1995	610	4	16 #6 bars (1.6%)	#3 at 2" (1%)
12	Japan 2011	610	4	16 #6 bars (1.6%)	#3 at 2" (1%)

#6 and #3 bars have 19 mm and 9.5 mm diameter respectively
ρ_l = longitudinal reinforcement ratio
ρ_s = volumetric ratio of transverse reinforcement
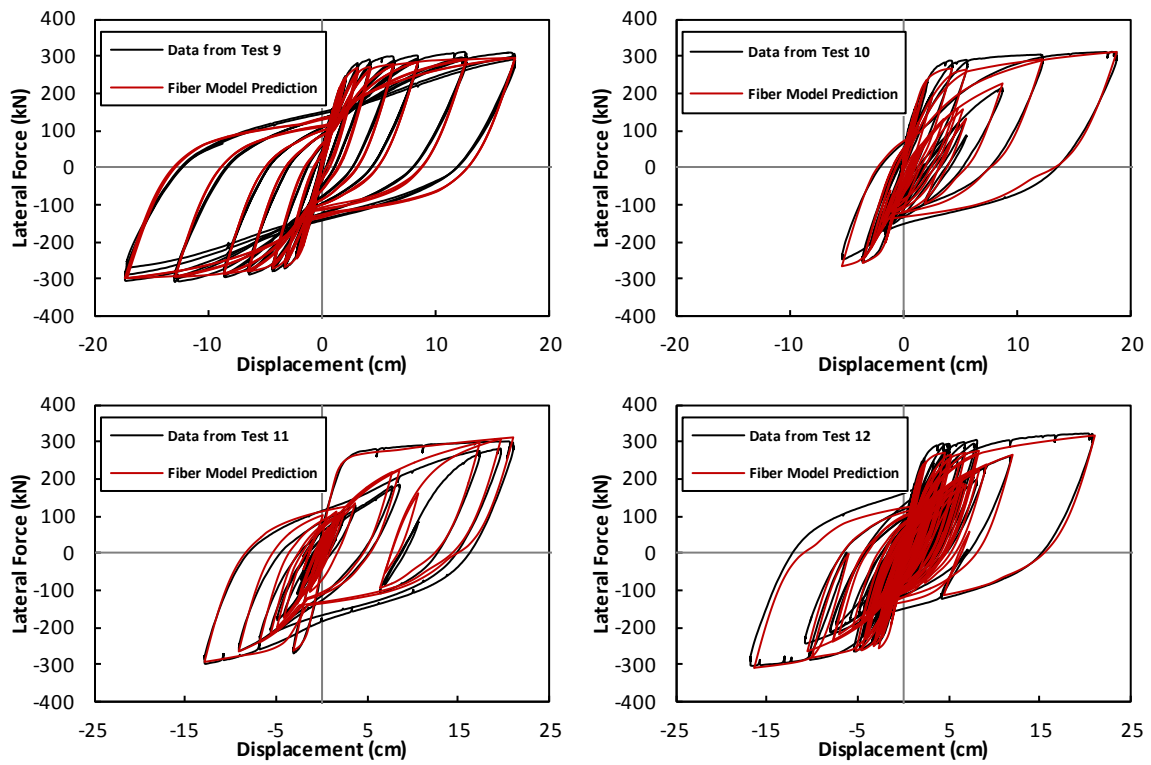
Figure 3.17. Comparison of force-deformation responses from the fiber model and test data
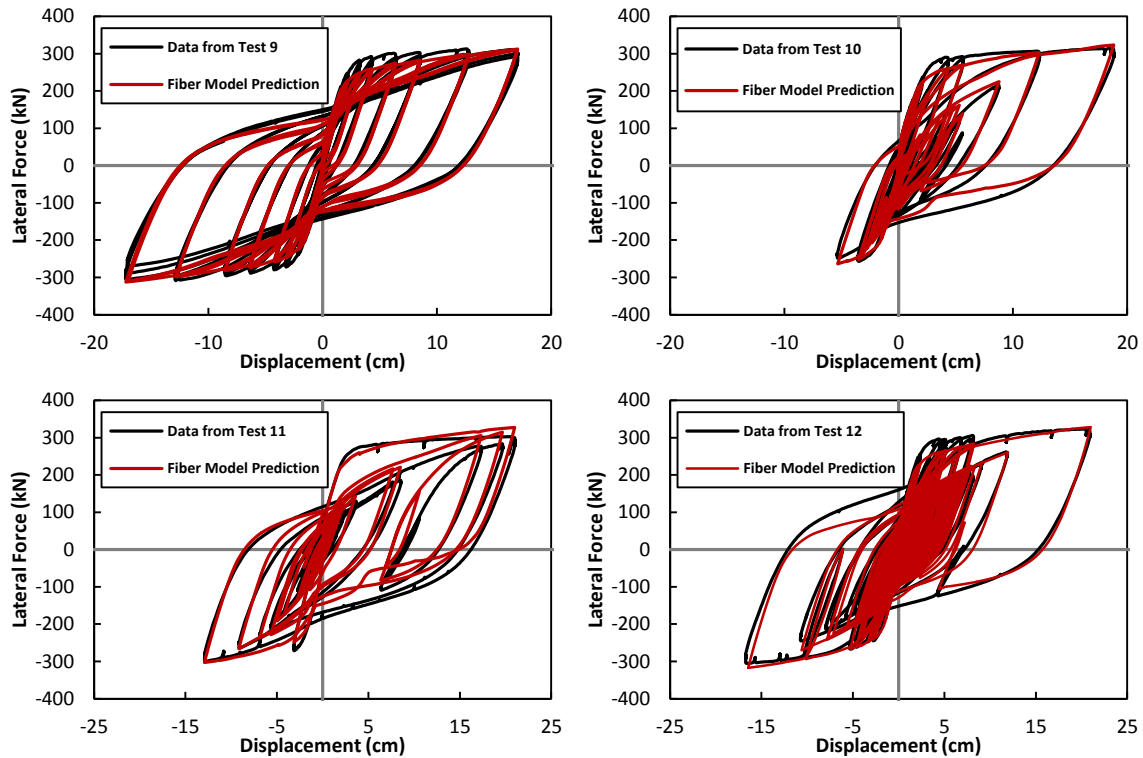
Figure 3.18. Comparison of strain hysteretic response from the fiber model and test data

The force-based element with nine integration points is combined with strain penetration simulation to predict the strain gradient in the plastic hinge region. Implementation of the proposed method allows the tension shift height to be calculated. The shear stress is assumed to have a parabolic distribution across the section.

The tensile strain profile is plotted including the tension shift. As shown in Figure 3.19, the predicted strain gradient is plotted against the strain profile from Test 9 to12. Tensile strain gradients (four on left) included the tension shift effect. The solid lines are the strain gradients at each significant peak displacement from experiments. Predictions are plotted in a dashed line with the same color at that displacement level. It is seen in both the model prediction and the test data that the plasticity spreads to a high level of displacement which

appears to be larger than the plastic hinge length calculated from Eq. 3.5. However, the compressive strain concentrates at the base of the column.

The model with the 'beam with hinges' element utilizes a single element to represent the nonlinear behavior in the plastic hinge. As a result, this model can only represent the linear distribution of the curvature where the material plasticity is controlled by the strain at the critical section. In the case of the cantilever column, the maximum strain in the fixed end section is the most important parameter to assess the performance of the structure. The 'beam with hinge' element could still provide the relationship between column displacement and sectional strain, although it fails to predict high order curvature distribution. As shown in Figure 3.21, the top column displacement is measured as the structural deformation and the strain is obtained from the plastic hinge region. The comparison in Figure 3.20 shows good agreement between the model prediction and test data, especially, at the peak strain level. However, the residual strain at zero displacement level is consistently underestimated by the model. Therefore, the accumulation of reinforcement strain over multiple cycles is not captured precisely. The solution to overcome this issue could be the development of an advanced reinforcement material model to include the low cycle fatigue behavior of steel since most current constitutive models are calibrated by material testing with limited cycles.

Figure 3.19. Prediction of Strain Gradients
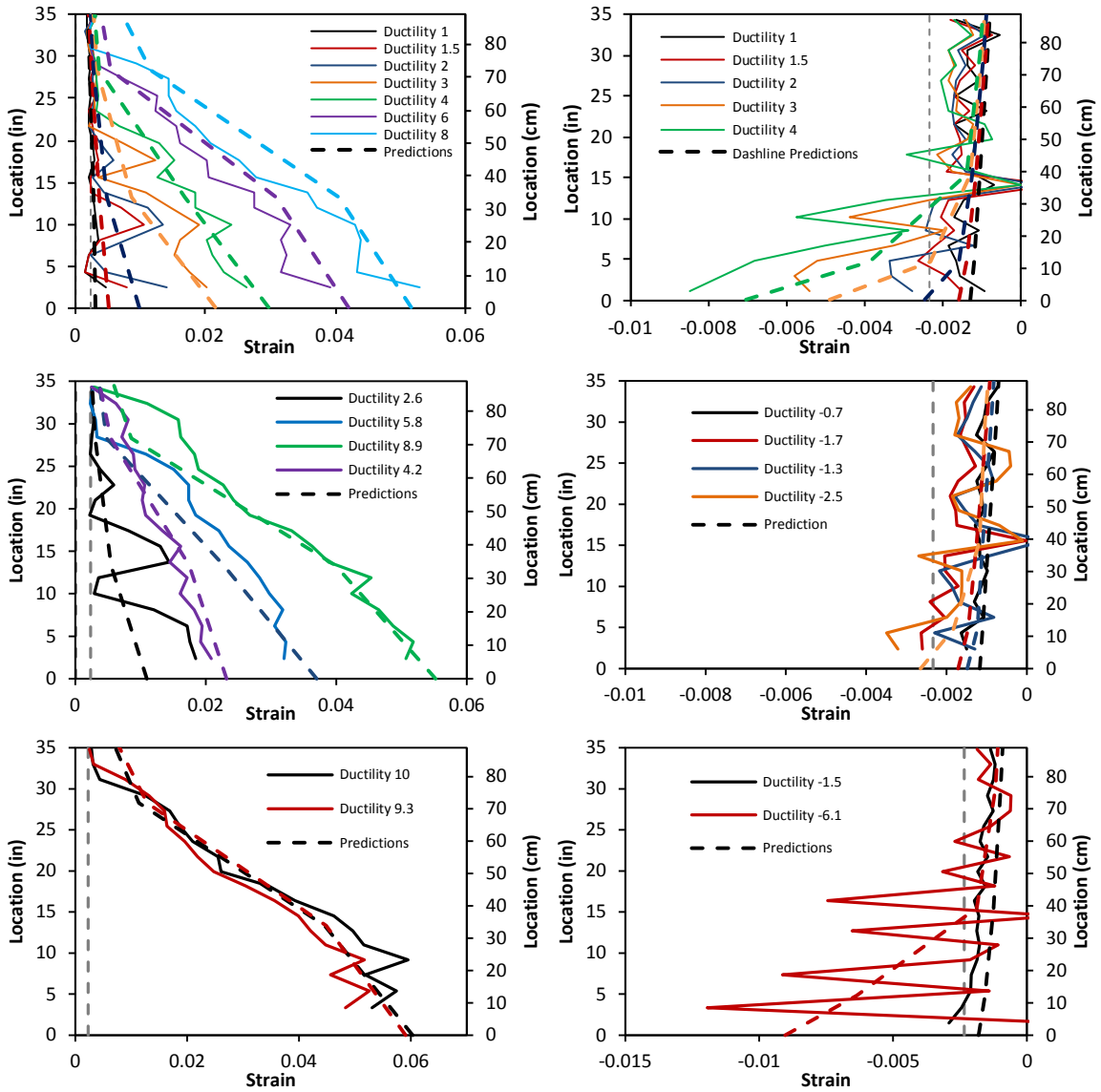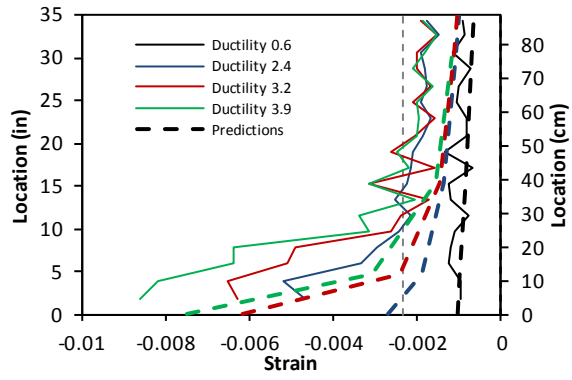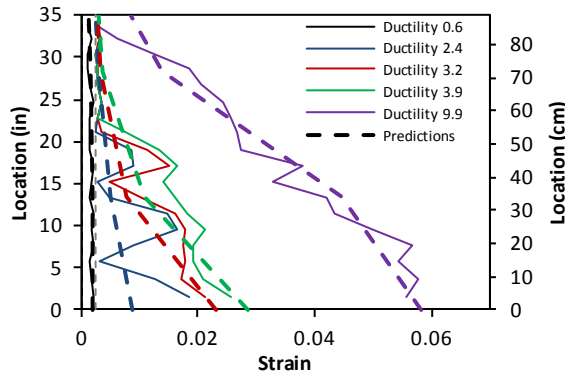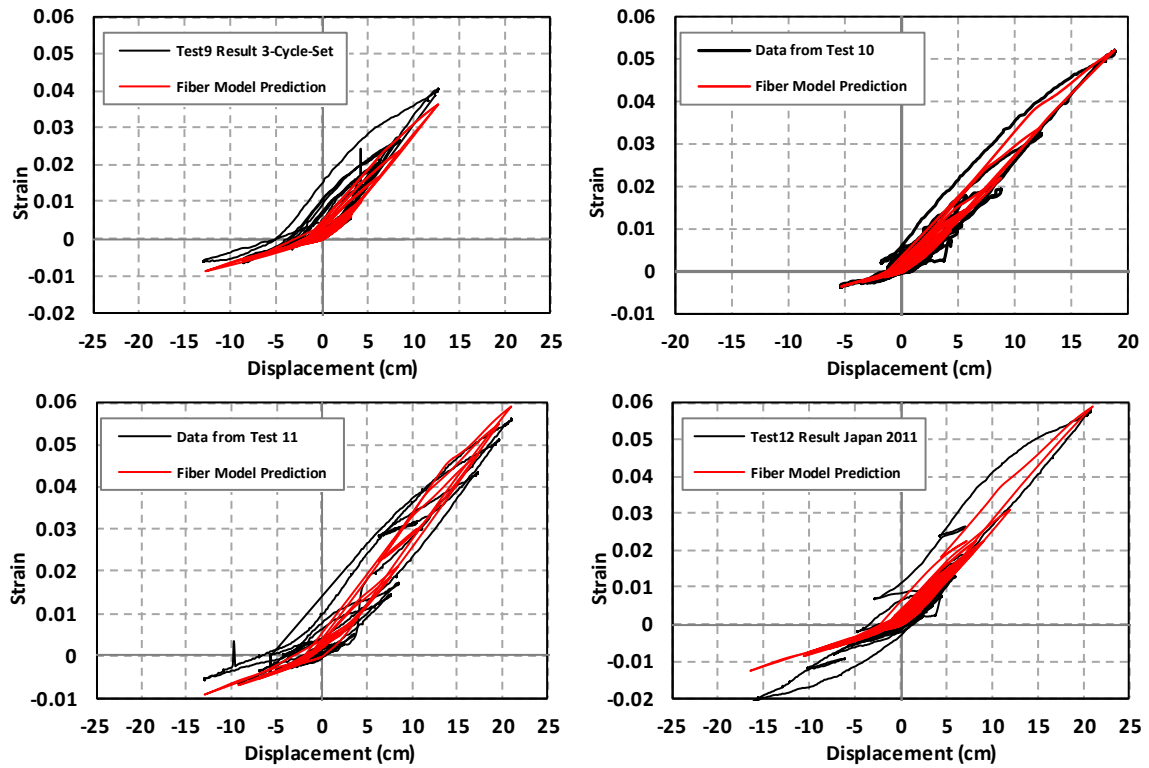
Figure 3.20. Comparison of strain hysteretic response from the fiber model and test data

Figure 3.21. Locations of displacement measurement and associated strain measurement (red arrow)

3.4.3   Prediction on Response of Shake Table Tests

The dynamic performance of the fiber-based models must be assessed such that the model may be used for further parametric studies. Therefore, both fiber-based models with 'beam with hinge' element as well as the nine IP force-based element were implemented to predict the displacement response of two shake-table tests. In fiber-based time history analysis, Petrini et al. (2008) presented that no additional damping should be added, since the hysteretic damping has been included at the material level. Therefore, there is no viscous damping applied to the model.

Petrini et al. (2008) conducted a shake-table test at the Centre of Research and Graduate Studies in Earthquake Engineering and Engineering Seismology where a hollow reinforced concrete column was subjected to the Morgan Hill earthquake. The Pacific Earthquake Engineering Research Centre (PEER) in conjunction with the Network for Earthquake Engineering Simulation (NEES) sponsored the Concrete Column Blind Prediction Contest (2010) at University of California, San Diego (UCSD). A full scale reinforced concrete bridge column was tested under a series of six ground motions from the Loma Prieta (1989) and Kobe earthquakes (1995). The comparisons of the displacement responses from the

fiber-based models and from the shake table tests are shown in Figure 3.22. Both fiber-based models capture most of the major peaks in the displacement response. However, they underestimate the residual displacement. In the UCSD shake table test, the underestimation of the residual displacement is due to lack of consideration of cumulative damage in concrete. The extensive residual displacement in the shake table test at the ROSE school is likely a result of local damage in the plastic hinge region, such as reinforcement buckling and concrete crushing or spalling. This column also ultimately suffered collapse due to a large P-Delta moment. The 'beam with hinge' element model yielded slightly better predictions for the dynamic responses.
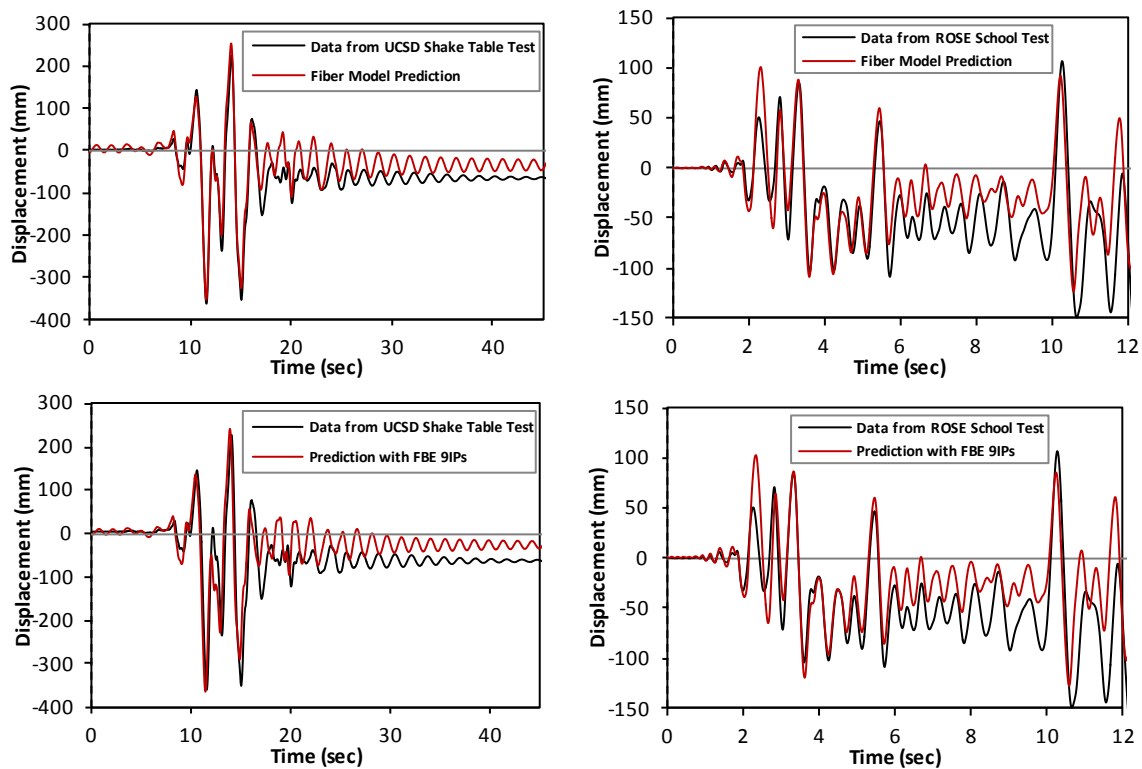
Figure 3.22. Comparisons of displacement response from fiber model and test data

3.5   Chapter Conclusions

In performance-based seismic engineering, engineers frequently use strain to assess performance of a structure. Strain values serve as a direct indicator of the local damage in modern engineering structures. Proposed modeling approaches fulfill the desire of strain information assessment. Their robust static and dynamic performances ensure the accuracy of prediction under various demands.

In a circular bridge column, the strain gradient can be well predicted using the post-processing approach with MCFT to quantify the tension shift effect of strain responses from the fiber-based model. The model combines a nine integration point force based element and a zero length element. The tension shift effect can be calculated from the crack angle distribution along the section and should be considered for the tensile strain distribution. As a computationally efficient method, which consists of a 'beam with hinges' element and the strain penetration simulation, is recommended while the strain magnitude or strain history at critical section is of paramount importance. However, this method requires the implementation of an empirical plastic hinge calculation to determine the length of spread of plasticity. Both models provided accurate force-deformation response and dynamic response as compared to the test results. It is worth noting that the approach to predict the angle distribution of the inclined flexural-shear cracking is suggested to be used for flexural members, such as beams and columns in a moment frame. Generally, both fiber based modeling approaches mentioned in this chapter can be applied to assemble a bridge and to assess the longitudinal bar strain along columns under earthquakes loading.

Chapter 4: Load History Effect on Relationship between Strain and Displacement

4.1 General Discussion

Given an RC bridge column, the one-to-one relationship between strain and displacement can be altered by the load history effect. At a given level of displacement magnitude, a variety of load histories may lead to different performance levels in a structure, which is often indicated by strain. For example, a load history with a large number of load cycles before reaching the peak displacement may result in more damage in the plastic hinge region, when compared to a monotonic pushover test. The strain is often selected as an indicator of performance since it directly relates to several damage mechanisms, such as concrete cracking, cover concrete spalling, core concrete crushing, and longitudinal bar buckling and subsequent rupture. The plastic hinge method by Priestley et al. (2007) combined with sectional analysis allows engineers to relate the strain to structural displacements. The structural configuration and sectional detailing determine the relationship between the strain and displacement. However, cyclic loading may also affect the local strain-global displacement relationship. To address this issue, the fiber-based model is utilized to study the effect of load history on the relationship between the strain and displacement.

4.2 Ground Motion Selection

This research specifically focuses on real earthquake load histories. Ground motions from different earthquakes, even from the same earthquake but at different stations, can be quite distinct. The key aspects of earthquake ground motions include peak ground acceleration (PGA), number of large acceleration pulses, magnitude of the large acceleration pulses, and the duration of strong shaking. While the ground motions were applied to a

structural system, the resultant structural displacement response (load history) will have corresponding features including the number of large displacement pulses, magnitude of the large displacement pulses, and the energy dissipation. A few examples of load histories are shown from Figure 4.1 to Figure 4.5. Figure 4.6 illustrates the profound difference in energy dissipation for different load histories. The acceleration in the ground motions of these examples were scaled to force the displacement response reaching the same magnitude, as a result of which allows the load history to be the sole variable.

Forty earthquake ground motions with a PGA greater than 0.4g were selected, as listed in Table 4.1. The load history effect on the limit state of longitudinal bar buckling is the other task of this research. Therefore, the ground motions with large PGAs were selected to permit bar buckling without significant scaling of the ground motions.
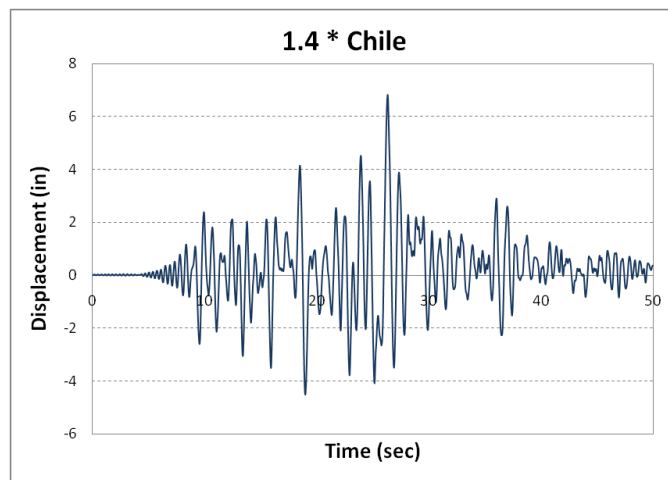
Figure 4.1 Load History from Chile Earthquake
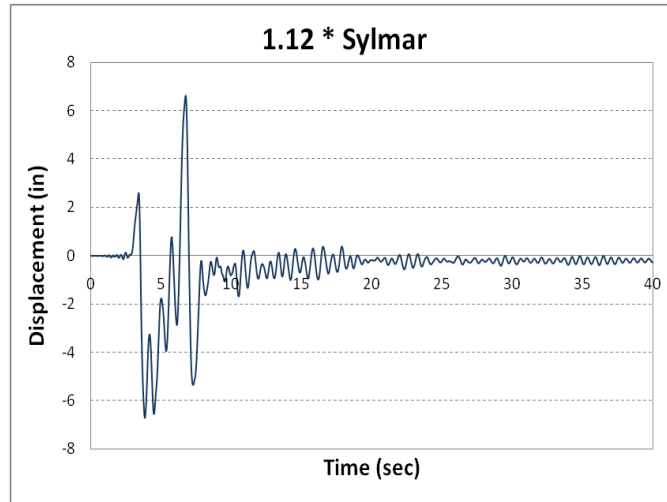
Figure 4.2 Load History from Northridge Earthquake (Sylmar Station)
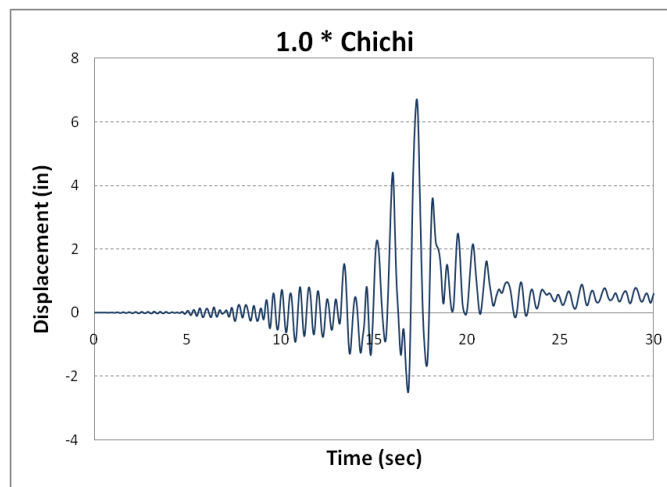
Figure 4.3 Load History from Chichi Earthquake
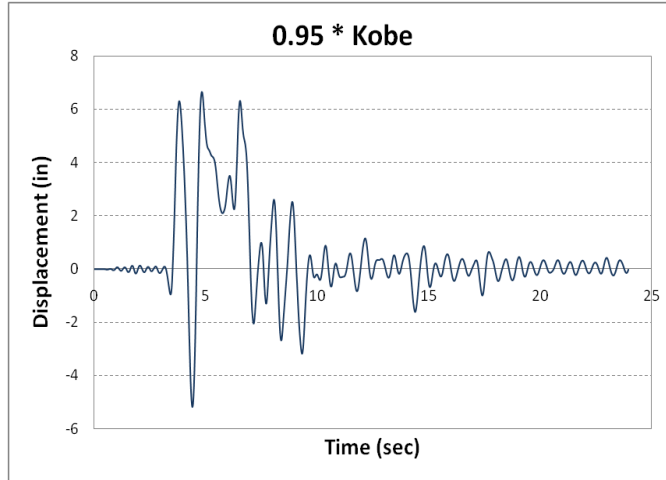
Figure 4.4 Load History from Kobe Earthquake
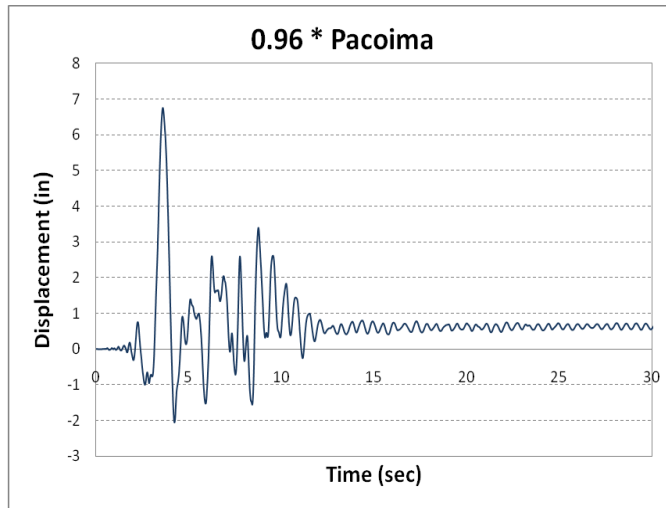
Figure 4.5 Load History from Northridge Earthquake (Pacoima Dam Station)
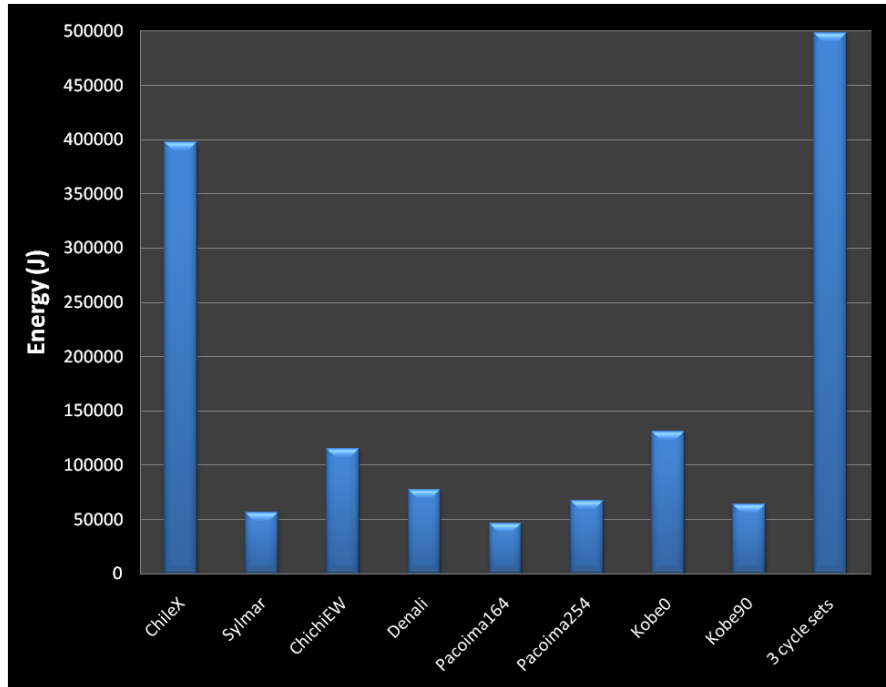
Figure 4.6 Energy Dissipation in the Example Load Histories

Table 4.1 Large Earthquake Ground Motion Database

Earthquake	Year	Station	PGA(g)
Chile	2010	N.A.	0.6
Japan	2011	TCGH	1.22
Kobe	1995	N.A.	0.82
Chichi	1999	N.A.	0.65
		No1197	0.8
		No1231	1
		No1503	0.8
		No1507	0.6
		No1517	1.2
		No2658	1
		No3474	0.8
Tabas	1978	N.A.	0.84
Northridge	1994	SylmarCSE	0.83
		Pacoima Dam	1.6
Darfield(NZ)	2010	GDLC	0.72
Christchurch(NZ)	2011	LPCC	0.88
Calexico	2010	Array11	0.6
Landers	1992	N.A.	0.8
Duzce	1999	Duzce	0.5
		Lamont	0.9
Erzican	1992	N.A.	0.5
Big Bear	1992	N.A.	0.5
Imperial Valley	1979	No160	0.8
		No180	0.5
		No183	0.6
Superstitions Hills	1987	No727	0.8
Managua	1972	No95	0.4
Victoria	1980	No265	0.6
Morgan Hill	1984	No451	1.2
Chalfant	1986	N.A.	0.45

Table 4.1 Continued

		No230	0.45
Mammoth Lake	1980	No231	0.4
Dinar	1995	No1141	0.45
Cape Mendocino	1992	No825	1.5
		No828	0.7
Nihanni	1985	N.A.	1
Loma Prieta	1989	N.A.	0.5
San Fernando	1971	N.A.	1.2
Coalinga	1983	N.A.	0.6
North Palm Springs	1986	N.A.	0.7

4.3   Parametric Study

For RC bridge columns with different detailing, a large number of NTHAs were conducted with all the ground motions from the database. The variables considered in this parametric study include load history, aspect ratio, axial load ratio, and reinforcement ratio. As presented in Table 4.2, columns with various configurations, reinforcement detailing and axial load ratio (ALR) are simulated with fiber-based elements. The transverse steel consists of a #3 spiral at 2 inch pitch in all columns. The fiber-based model with "beam with hinges" element was utilized to model the column, since this element is a more accurate model compared to the one with nine integration points. In addition, the maximum strain in the plastic hinge region determines the likelihood of bar buckling, while there is no direct evidence showing that the strain distribution in adjacent regions affects bar buckling. As a result, the load history effect on the relationship between maximum strain and displacement is investigated rather than the relationship between the strain distribution and displacement. The method to generate strain distribution is utilized to obtain 3D interaction surfaces of axial strain, shear stress, and crack angle, given a location of the section. The interaction surfaces are shown in the Appendix I.

All ground motions in the database are applied to each fiber-based column model in the NTHAs. The load history effect on the relationship between strain and displacement is studied by comparing the strain hysteretic response to the strain versus displacement curve

from monotonic analysis. The strain difference at the same displacement level between a monotonic analysis and a time history analysis then indicates the impact of the earthquake load history on the relationship between strain and the displacement.

Table 4.2. Details of Columns

Column #	L (ft)	D (ft)	ALR	d_{bl}(in)	# of Bars	P_s (%)
1	8	2	5.3	0.75	16	0.9
2	12	2	5.3	0.75	16	0.9
3	16	2	5.3	0.75	16	0.9
4	8	2	10	0.75	16	0.9
5	8	2	15	0.75	16	0.9
6	8	2	20	0.75	16	0.9
7	8	2	5.3	0.75	12	0.9
8	8	2	5.3	0.75	20	0.9

Figure 4.7 and Figure 4.8 show an example of a strain hysteretic response which is compared to the strain and displacement relationship under monotonic loading. The influence of load history on the peak tensile strain value of a load history will change the likelihood of bar buckling which often occurs upon reversal from the large tensile strain (Moyer and Kowalsky (2003)). The magnitude of the tensile strain is believed to determine whether instability of a bar will occur upon reversal. Therefore, the peak tensile and compressive strain points were plotted against the monotonic strain and displacement relationship in Figure 4.8 to show the load history effect.
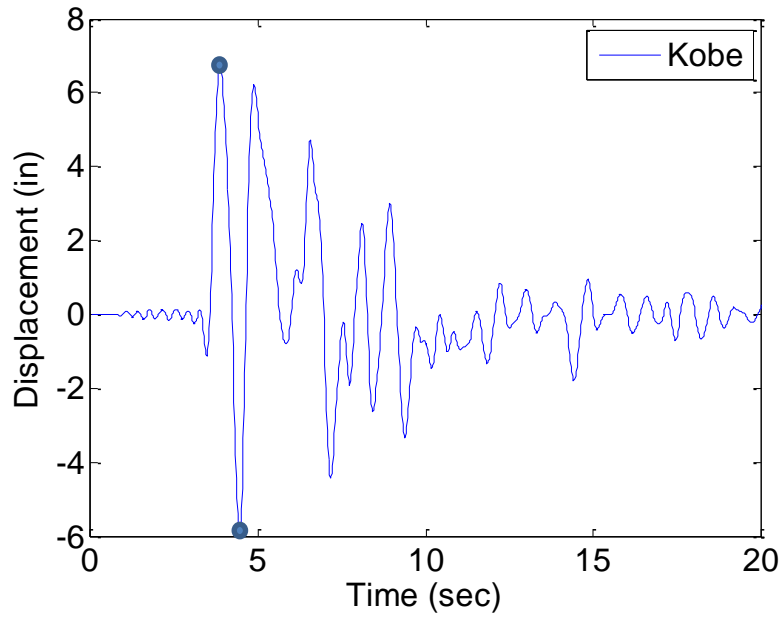
Figure 4.7 Displacement Response under Kobe Earthquake Ground Motion
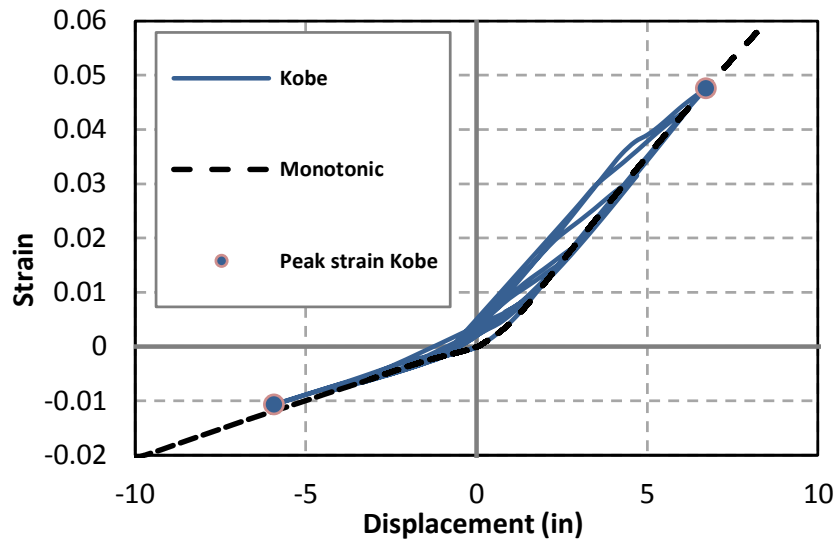
Figure 4.8 Strain Hysteretic Response

4.3.1   Strain Comparison for Column #1

Column #1 is considered as the benchmark column since multiple specimens with identical detailing were tested, and whose results were utilized to calibrate the fiber-based models. Therefore, the model predictions on dynamic displacement and strain response with this column have very high accuracy. As mentioned, the peak strain points for extreme fiber bars were plotted against the relationship between strain and the displacement under monotonic loading. In addition, a linear regression line (solid line in the figure) is also generated and shown in Figure 4.9.
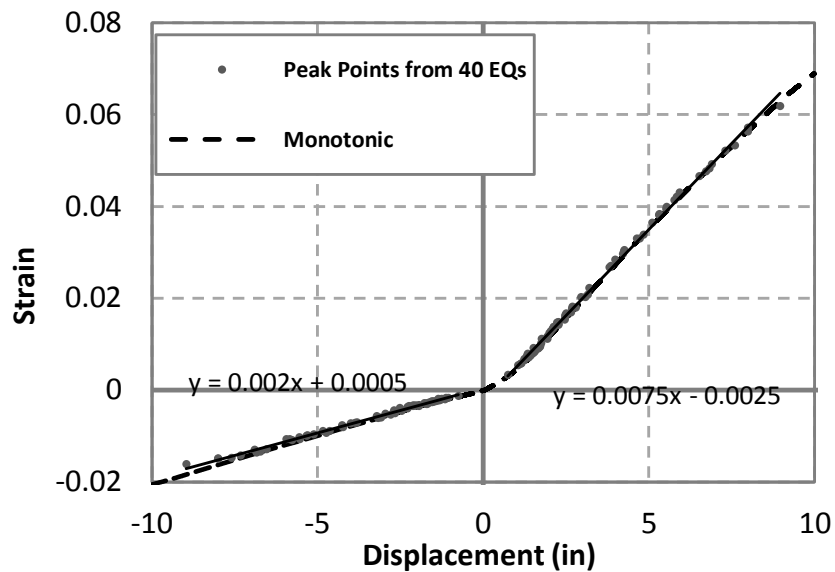
Figure 4.9 Peak Strain Values from Earthquakes for Column #1

Figure 4.9 presents a relative linear relationship between strain in extreme fiber bars and the displacement at the top of column. In addition, the monotonic strain-displacement curve

is able to predict very close values for the peak strain points from earthquake load histories. Moyer and Kowalsky (2003) illustrated that load cycles will increase the tensile strain by imposing an additional growth strain in the bar at each cycle. However, Figure 4.9 shows that different load histories still generate a similar strain value as others at a given displacement level. Load cycles do not alter the peak strain significantly.

4.3.2   Strain Comparison for Column #2

Column #2 has a larger aspect ratio (L/D=6) compared to the benchmark column. Due to the increase of flexibility, strain value at the similar displacement level is lower than the one from Column #1. A longer column requires less sectional deformation to reach the same displacement. The aspect ratio has apparent impact on the relationship between strain and the displacement which can be simply studied with the plastic hinge method (Priestley et al. (2007)) and will not be investigated here.

On the other hand, the earthquake load history fails to affect the relationship between strain and the displacement. The peak strain points still follow the monotonic strain-displacement curve at all deformation levels.
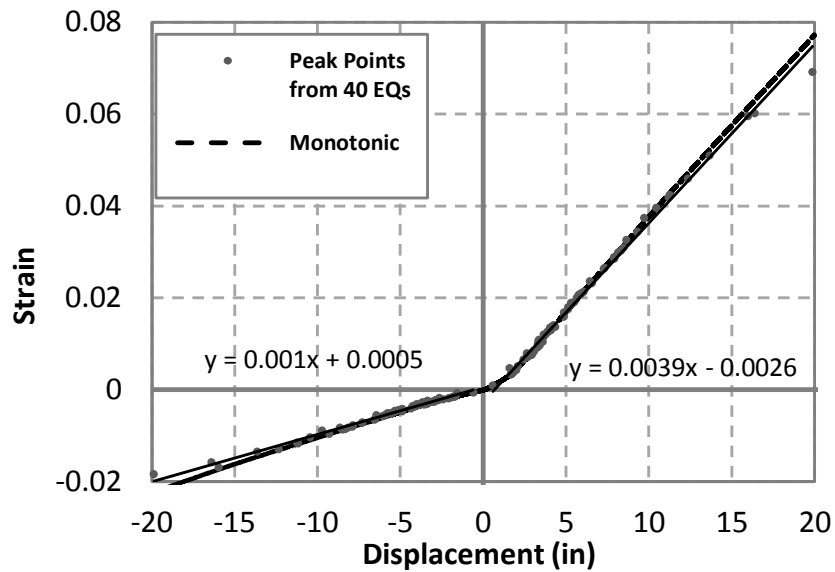
Figure 4.10 Peak Strain Values from Earthquakes for Column #2

4.3.3   Strain Comparison for Column #3

With a large flexibility at aspect ratio of 8, strain in the base section of Column #3 has a low magnitude compared to all previous columns. Again, no significant impact from load history is observed in the relationship between strain and the displacement.
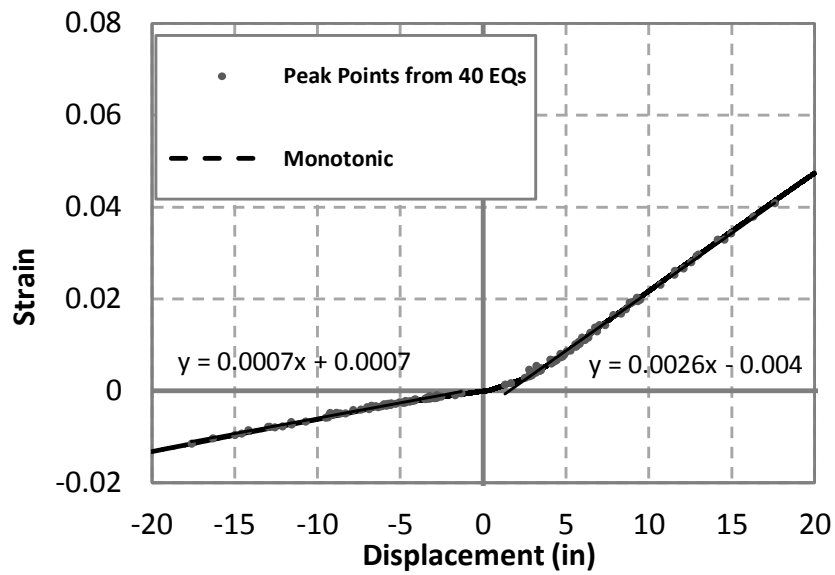
Figure 4.11 Peak Strain Values from Earthquakes for Column #3

4.3.4   Strain Comparison for Column #4

The axial load ratio in Column #4 was increased to 10% from the 5.3% of the benchmark column. The change of axial load ratio will increase the P-Delta effect and the sectional behavior in the fiber-based element. Comparing Figure 4.12 with Figure 4.9, the compressive strain in the section significantly increased due to a larger axial load. The impact of axial load on the sectional deformation and strain value has been studied with moment-curvature analysis and plastic hinge method.

Generally, the load history is not able to alter the relationship between strain and the displacement which still follows the monotonic curve.
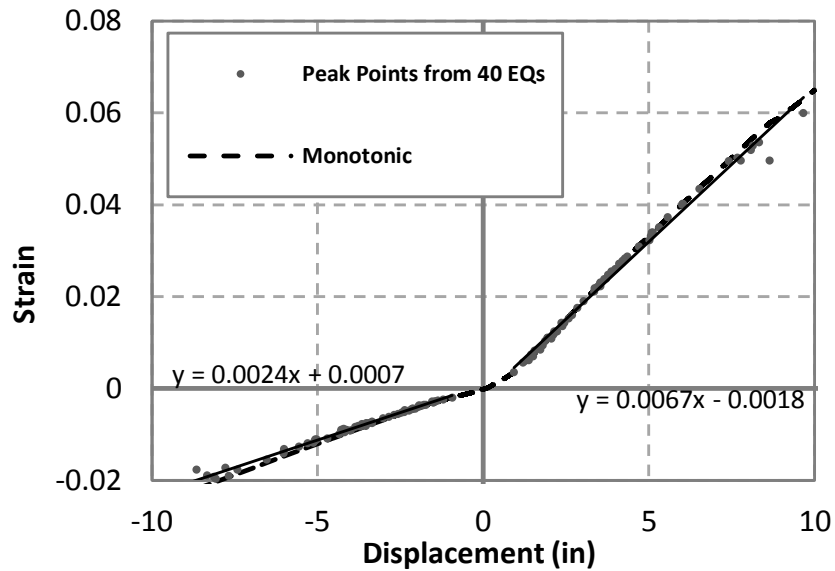
Figure 4.12 Peak Strain Values from Earthquakes for Column #4

4.3.5   Strain Comparison for Column #5

Significant increase of axial load in Column #5 leads to reduction of tensile strain at a given displacement level, as presented by the least square error line in Figure 4.13. Deviation occurs between the tensile strains from monotonic curve and some of the peak strain points from earthquakes. However, the monotonic strain-displacement curve still serves as a good prediction for the peak strain points from most of the earthquakes.
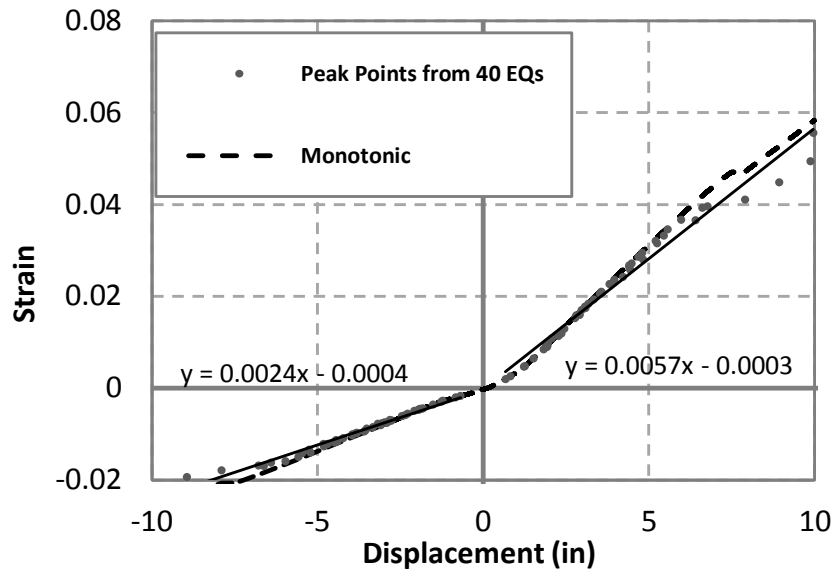
Figure 4.13 Peak Strain Values from Earthquakes for Column #5

4.3.6   Strain Comparison for Column #6

A large axial load ratio of 20% in Column#6 is an extreme case for a regular RC bridge column. At displacements larger than 5 in (Figure 4.14), the monotonic curve generally predicts 10% to 15% larger strain values compared to the peak points from NTHA. In design, over-prediction of strain from a monotonic curve is on the conservative side, so it is not necessary to include the load history effect only for the case with excessive large axial load.
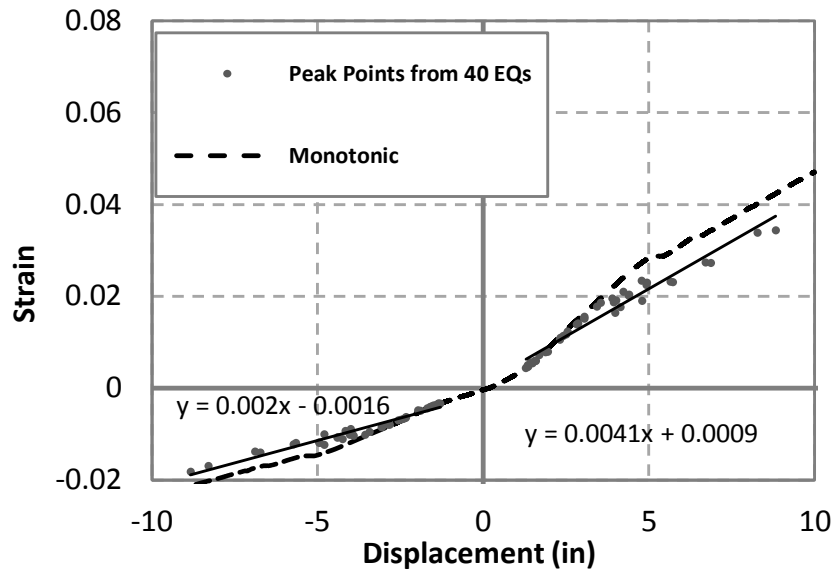
Figure 4.14 Peak Strain Values from Earthquakes for Column #6

4.3.7   Strain Comparison for Column #7

The number of bars in Column #7 is reduced from 16 to 12 and results in a corresponding reinforcement ratio 1.2%. This column represents an extremely low reinforced case. Again, the monotonic strain-displacement curve provides extremely close prediction for the peak strain points from all the earthquakes. Load history still fails to influence the relationship of strain and the displacement.
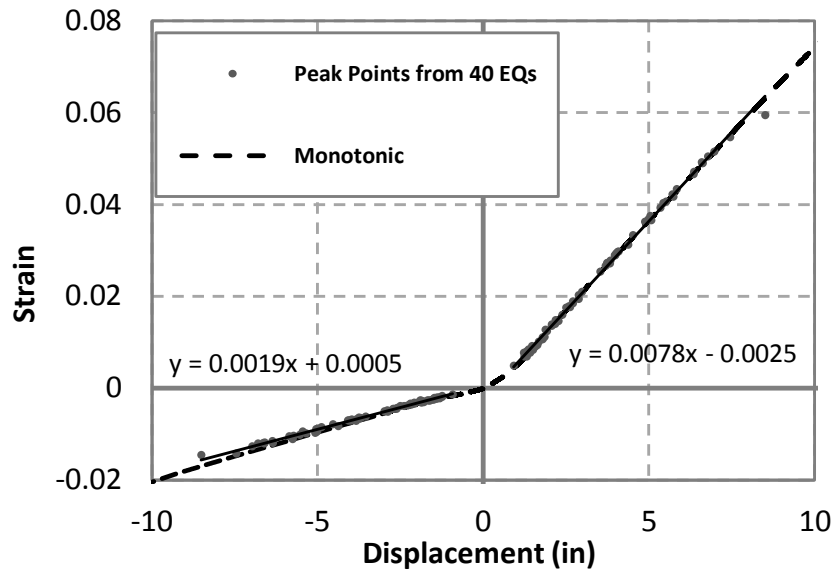
Figure 4.15 Peak Strain Values from Earthquakes for Column #7

4.3.8 Strain Comparison for Column #8

Column #8 has a reinforcement ratio 2% and represents a heavily reinforced case. It is observed in the both Figure 4.15 and Figure 4.16 that the reinforcement ratio does not change the relationship between strain and the displacement, while the bar diameter remains the same. In the case of altering the bar diameter to achieve the desired reinforcement ratio, the pre-defined plastic hinge length of the 'beam with hinges' element will be change, which is likely to affect the relationship between strain and displacement. The effect of bar diameter can also be studied with the plastic hinge method. The load history also fails to force the peak strain values deviate from the prediction of monotonic curve.
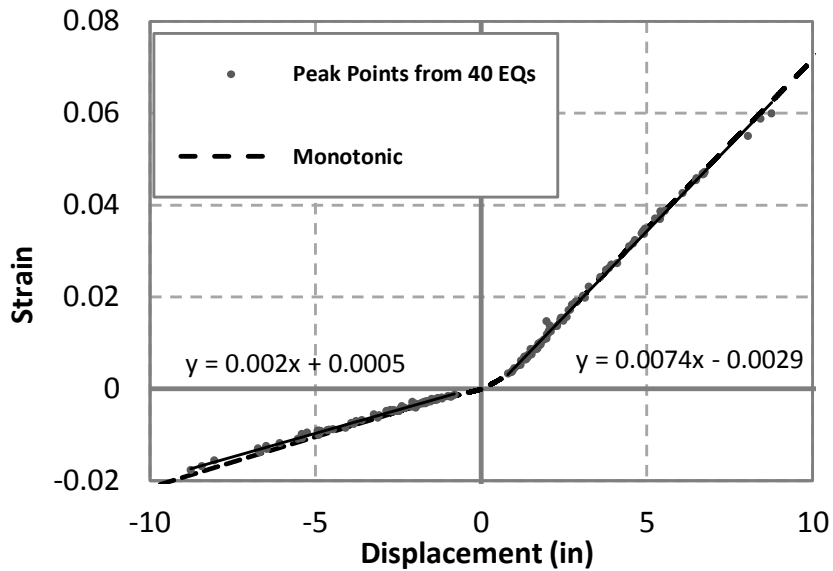
Figure 4.16 Peak Strain Values from Earthquakes for Column #8

4.4 Chapter Summary

A large number of NTHAs were conducted with 8 columns which considered the variables including axial load ratio, aspect ratio and reinforcement ratio. The load history effect on the relationship between strain and the displacement was investigated with each column. It was shown that very limited effect was imposed on the relationship by all the load histories. Instead, the structural parameters themselves had more impact on the strains at the critical section. It is not necessary to include the load history effect on the relationship between strain and the displacement in design or assessment, although, as noted in Volume 1 of this report (as well as in Chapter 5 and 6 of Volume 3), loading history does impact the strain limits associated with performance limit states such as bar buckling.

Chapter 5: Development of Finite Element Model for Bar Buckling

5.1 Introduction

As an important limit state for earthquake engineering, reinforcing bar buckling is generally regarded as the condition beyond which a structure requires replacement. For example, the current practice of the California and Alaska Departments of Transportation is to replace structural members that exhibit a high degree of reinforcing bar buckling. This is the result of the likely fracture that occurs following the development of micro-cracks at the onset of local bar buckling (Restrepo-Posada, 1994) that tend to propagate with increasing strains (Erasmus, 1981). As a consequence, accurate models to predict the onset of bar buckling are critical for seismic design, but generally absent in the literature. While empirical models to predict bar buckling exist, and serve as a useful purpose for design, they are nonetheless limited by the boundaries of the data used in their generation. Furthermore, from the perspective of developing a fundamental understanding of behavior, accurate prediction of longitudinal bar buckling requires either analytical or computational solutions that are supported by experimental evidence.

A number of researchers have related bar buckling to monotonic loading in compression and some studies considered the effect of cyclic loading on bar buckling. Rodriguez et al. (1999) found that longitudinal bars are most prone to buckling upon reversal from cycles of significant tension. Moyer and Kowalsky (2003) concluded that the tensile stain demand has a large impact on bar buckling upon subsequent compressive reversals. Therefore, bar buckling should include the effect of the entire loading history. It has also been observed in experiments (Goodnight and Kowalsky (2012)) that cyclic load history has a significant effect on tensile strains which lead to buckling upon reversal. In addition, reinforcing bars often buckle before concrete cracks close. Berry and Eberhard (2005) established a practical performance model to predict the deformation level where bars buckle. The model includes

the effect of the confinement ratio, axial-load ratio, aspect ratio, and longitudinal bar diameter on the required deformation for bar buckling.

It is difficult to numerically simulate a RC structural member including the inelastic buckling of longitudinal reinforcing bars. Modeling localized nonlinear behavior and the complicated boundary conditions, as well as their interactions with the reinforcing bar, requires extensive computational cost, as failure of convergence often occurs in analysis. However, the localized behavior must be simulated appropriately to study the effect of loading history and section detailing on bar buckling. Numerous modeling approaches have been developed to capture bar buckling in reinforced concrete structures. Mau and El-Mabsout (1989) developed a beam-column element to carry out inelastic analysis of reinforcing bars to generate the stress-strain behavior of buckled bars. Dhakal and Maekawa (2002) utilized the finite element method to establish the stress-strain relationship including post buckling behavior and implemented it into a fiber-based model. Masukawa et al. (1999) presented a classic bar buckling model in which a beam-column element was utilized to simulate the bar and springs modeled the boundary condition at the hoops. The model was applied to study the inelastic buckling stress. Zong and Kunnath (2008) compared the stress-strain behavior of reinforcing bars in both a full column finite element model and an independent bar-with-springs model. Bar buckling over multiple spiral layers was considered in this study. However, the full column finite element analysis assumed the concrete to be elastic which is actually representing a bearing foundation of longitudinal bars and spirals. Calladine (1972) and Bae et al. (2005) both studied the impact of imperfections on inelastic bucking of longitudinal bars.

In most cases, the goals of these studies were to investigate the effect of reinforcing bar buckling on stress-strain behavior, or the force-deformation response of the structural member. Independent bar buckling models were developed to include the post-buckling behavior on the stress-strain relationship. The typical modeling approach simulated the bar with one or multiple beam-column elements with fixed ends and converted the hoops or spirals into springs to restrain out-of-plane deformation. The beam-column elements behaved

uniaxially until the buckling load was reached, and the out-of-plane deformation activates the restraining spring. Therefore, the buckled bar retained load carrying capacity because of the presence of the lateral restraint. These models provided a general idea of the post buckling behavior and a coarse prediction of buckling load in some cases, but the simplified boundary conditions do not consider the dilation of the concrete core and its effect on bar buckling. In addition, the effect of cyclic load history and reinforcement detailing, such as spiral pitch and bar diameter, has not been studied.

5.2   Research Objective

Presented in this chapter is a hybrid finite element method to accurately predict bar buckling in RC members. The approach contains a fiber-based model to predict the strain history at the local region, which results from global force or displacement demand on the structural member. A finite element model with solid elements simulates the potential buckling region of a bar and the boundary condition from adjacent hoops and concrete. The fiber-based model produces the local strain history which is then applied to the finite element model of the local area in the plastic hinge region. The overall objective of this model is to generate recommendations on seismic design considering longitudinal bar buckling as the limit state. To accomplish this objective, it is of obvious importance to study the effect of load history and sectional detailing, such as transverse steel details, reinforcing bar diameter, axial load ratio and column aspect ratio, on inelastic bar buckling. A parametric study using the two-step approach described in this chapter will fulfill this requirement.

5.3 Experimental Observation on Inelastic Bar Buckling upon Reversal of Loading

Moyer and Kowalsky (2003) observed the influence of tension strains on the eventual buckling of longitudinal bars, and described a tension-based buckling mechanism. Moyer and Kowalsky (2003) illustrated the distinct features of the tension-based bar buckling mechanism summarized as follows. First, buckling of reinforcement requires reversal of loading. Second, significant tension strain is required to activate the tension-based bar buckling mechanism at a later cycle. Third, the accumulation of tensile strain over multiple loading cycles impacts longitudinal bar buckling. Lastly, since bar buckling eventually occurs under compression, it is important to quantify the compressive load capacity associated with bar buckling.

Figure 5.1(a) displays an idealized reinforced concrete column and location of its extreme fiber bars. At the bottom location of the column, Bar 2 on the left side of the column will be subjected to tensile strain under a load towards the right. In contrast, Bar 1 on the right side of the column will experience a compressive strain. The uniaxial strains in reinforcing bars change their sense upon reversal of the lateral loading.

Figure 5.1 (b) represents the force-deformation relationship of a complete loading cycle. Bar 2 is under tension when the column is loaded from the origin to State A. Upon reversal from State A to State E, the strain in Bar 2 changes to compression, while Bar 1 experiences a tensile strain. Large flexural cracking on the tensile side of the column will occur. As a result, Bar 2 represents the only source for compressive stability at State B, where the reinforcement is prone to buckle. Bar 1 may also suffer from buckling upon reversal from State E. Moyer and Kowalsky (2003) stated that the different loading history of Bar 1 from Bar 2 led to growth strain. The growth strain caused a larger total tensile strain than the one from monotonic loading, which in turn likely results in instability upon reversal.

(a) Idealized RC column

(b) Idealized Response

State A   State B   State C   State D   State E

(c) Critical states of deformation
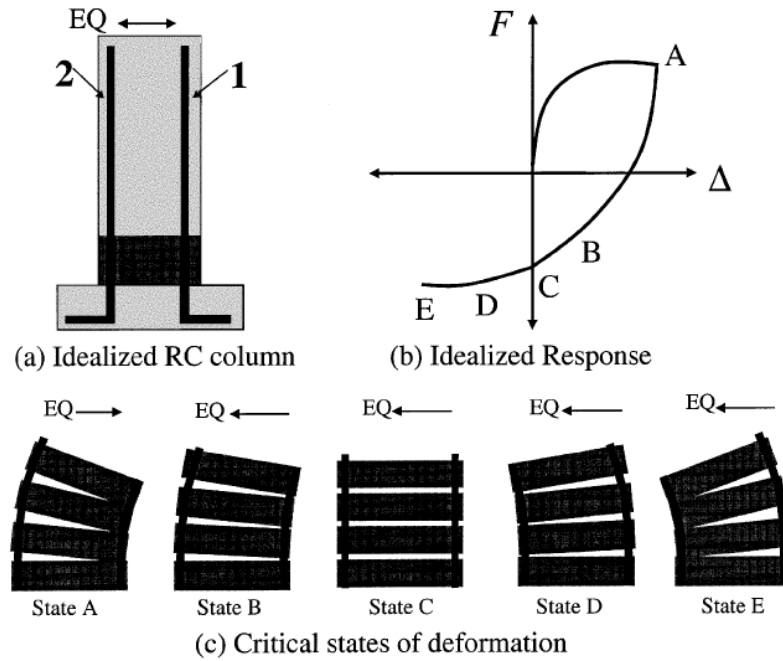
Figure 5.1. Tension-Based Buckling Mechanism from Moyer and Kowalsky (2003)

5.4 Theoretical Inelastic Column Buckling upon Reversal of Loading

Euler's method to calculate the critical buckling load of an elastic column is shown in Eq. 5.1 where the E_s, I, K and L represents the Young's modulus of steel, moment inertia of the column, column effective length factor, and the length of column, respectively. In order to estimate the inelastic buckling force, Engesser (1889) applied a modification to Euler's theory by replacing the Young's modulus with the tangent modulus E_T, as shown in Eq.5.2 However, Jasinski (1895) stated that the modulus varies along the buckled column section because of the strain variation in the section. A reduced modulus method (double modulus) was then developed by Engesser (1891) and Karman (1910) to account for the modulus variation along the section in a buckled column. However, numerous experiments have shown that test results matched the prediction from tangent modulus theory. The load increase after buckling predicted by the reduced modulus theory was hardly observed. Shanley (1946) acknowledged that the tangent modulus equation should be used as a basis for determining the buckling force of a member in the inelastic range, although the reduced modulus theory represents the exact behavior of inelastic buckling. It is worth noting that all of these investigations considered inelastic buckling under monotonic compressive load.

$$P_{cr} = \frac{\pi^2 E_S I}{(KL)^2} \qquad\qquad 5.1$$

$$P_T = \frac{\pi^2 E_T I}{(KL)^2} \qquad\qquad 5.2$$

5.5 Theoretical Case Study on Inelastic Bar Buckling

To quantify the buckling load, the tangent modulus theory is utilized in this section to explain the tension influence on inelastic bar buckling. Two idealized RC columns as shown in Figure 5.2 are considered. The sectional detailing is shown in Table 5.1. The two columns are displaced to different magnitudes of deformation at State A, then are both reversed to the

same displacement at State E. It is assumed that the left bar (denoted as Bar 2 in Figure 5.1) reaches a tension strain 0.04 while the other left bar has a tensile strain 0.02 at State A. The stress-strain responses of the two bars are shown in Figure 5.2, by implementing the reinforcing steel constitutive model from Dodd and Restrepo-Posada (1995). Corresponding to Eq. 5.3, the buckling stress (fcr) curves are portrayed in Figure 5.2 (dashed lines) for the two stress-strain response. It can be observed that the bar which experienced strain history 1 buckled before the crack closure at State D. This explains Moyer and Kowalsky's (2003) statement that significant tensile strain is required to activate the tension-based buckling, since reversal from a larger tensile strain imposes a more severe reduction in tangent modulus and a larger increase in nominal bar stress. Both of the phenomena increase the likelihood of bar buckling.

$$f_{cr} = \frac{P_T}{A_b}$$

5.3

Moyer and Kowalsky (2003) also stated that the crack closure at zero strain (State D) engages the concrete and enhances the compression zone stability, thus postponing buckling. As the structure continuous to load from State D in Figure 5.2, the compressive stress increase in the Bar 2 will be limited because of the concrete contribution in compression. Theoretically, it is possible to generate bar buckling after crack closure as the buckling stress (blue dashed line) curve in Figure 5.2 will intersect with the stress-strain response eventually. However, it often requires a large sectional curvature as well as a large structural deformation to accomplish the required compressive stress. Similarly, bar buckling in a reinforced concrete column is hardly seen under monotonic loading since the section fails to provide the required compressive stress in the bars. The degradation of tangent modulus and the increase in nominal bar stress under monotonic compression is much lower than those from a large reversal strain. The structural system will fail under bar fracture on the tensile side of the section before the onset of buckling in compressive bars. To predict bar buckling, a model is required to relate the structural load history to sectional cyclic behavior which eventually determines the strain history on longitudinal bars. In addition, the effect of the

axial load ratio and the aspect ratio on the relationship between the structural deformation history and the bar strain history should be investigated. Fiber-based elements are implemented in this chapter to provide a tool for this purpose.

In summary, the tangent modulus theory explains the influence of tensile strain magnitude on longitudinal bar buckling. However, both Moyer and Kowalsky (2003) and Kunnath and El-Bahy (1996) observed a large impact of the number and characteristics of the load cycles on the required deformation ductility to initiate bar buckling. This cannot be explained by the idealized column behavior with tangent modulus theory. Therefore, a computational finite element model is proposed to overcome this problem.

Table 5.1. Parameters in the Case Study

Parameters	Values	Units
Spiral Spacing	100	mm
K	0.5	N.A.
E_s	200000	MPa
f_y	470	MPa
d_b(#6 bar)	19	mm
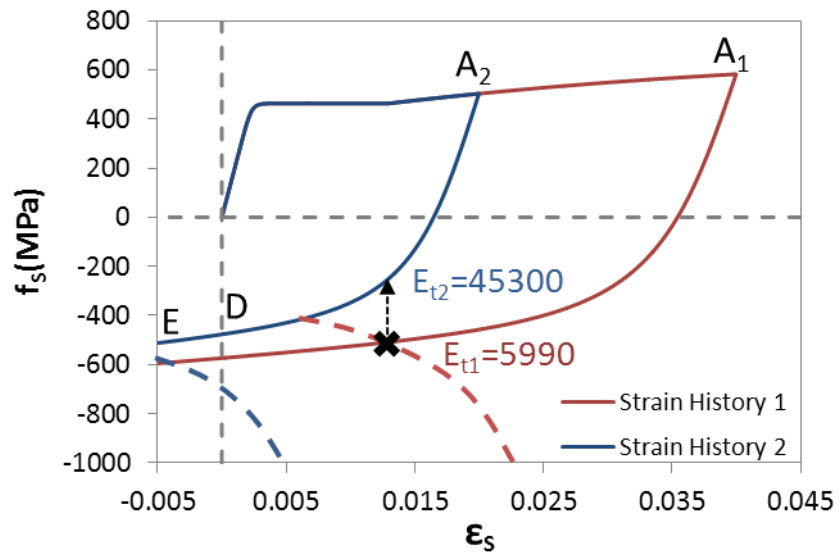
Figure 5.2. Stress-Strain Responses upon Reversal from Tension

5.6 Fiber-Based Modeling of Reinforced Concrete Structures

The onset of reinforcing bar buckling depends significantly upon the strain history. However, structural demand is often expressed in terms of loads or deflections. It is therefore important to establish a reliable relationship between global loading and local strain response. A fiber-based element model is utilized to evaluate local resultant strain under static or dynamic loading. Feng et al. (2012) introduced the fiber-based method to capture the nonlinear behavior of reinforced concrete columns. The model was shown to accurately predict dynamic displacement response and local strain via comparison to multiple static column tests and dynamic shake table tests. To obtain strain response from an earthquake load history, a nonlinear time history analysis will be conducted with the fiber-based model.

As shown in Figure 5.3, the fiber-based element technique consists of a force-based element and a zero length element. The force-based element represents the reinforced concrete column itself while the zero length element captures the strain penetration behavior into the footing. By modeling strain penetration, the inelastic strains that develop below the footing-column interface and the associated impacts on total column deformation will be captured. Otherwise, the material strains would be overestimated for a given column lateral displacement. Figure 5.4 shows the accurate prediction of the hysteretic strain response this model provides when subjected to a given loading history. Figure 5.5 illustrates the locations at which the structural displacements and longitudinal bar strains are measured.
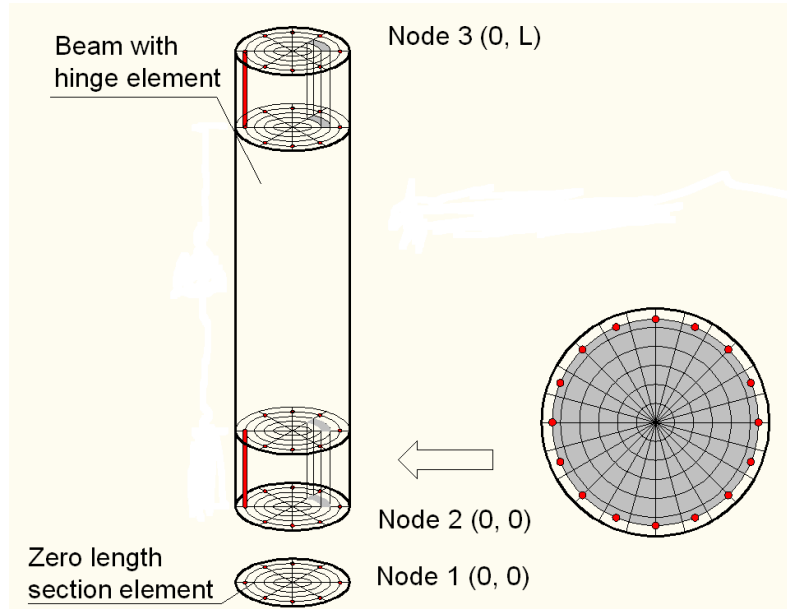
Figure 5.3. Fiber-Based Model from Feng et al. (2012)
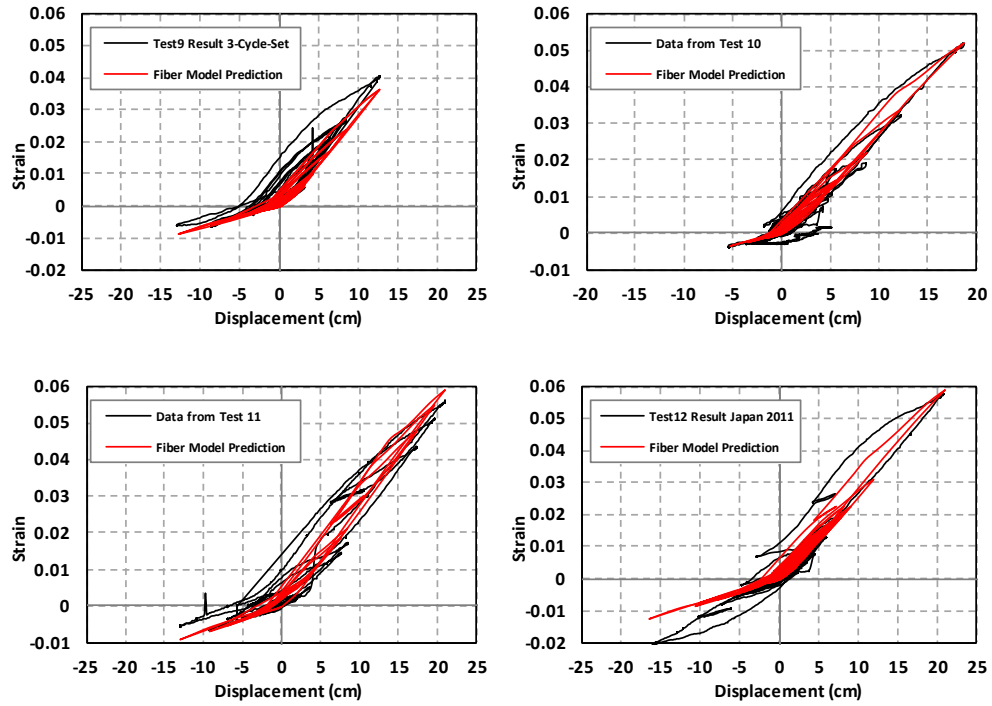
Figure 5.4. Comparison of strain hysteretic response from the fiber model and test data

Figure 5.5. Locations of displacement measurement and associated strain measurement

(red arrow)

5.7 Proposed Finite Element Bar Buckling Model (Strain-Based)

5.7.1 Goal of Simulation

As previously described, longitudinal bar buckling occurs within the plastic hinge region, upon reversal from a tensile strain which leads to the bars serving as the sole source for compression zone stability. The reversal strain causes a large compressive stress demand and reduction of tangent modulus where the bars are then prone to buckling until the cracks close. In addition, the number and magnitude of cycles from a load history or strain history also affects inelastic bar buckling (Moyer and Kowalsky (2003) and Kunnath and El-Bahy (1996)). The level of tensile strain that may be sustained prior to buckling is impacted by the boundary conditions that support the longitudinal reinforcing bars in the potential buckling region, which in turn depend on the local reinforcement detailing and sectional geometry. For example, even upon reversal from a large tensile strain, a smaller spiral pitch can reduce the unsupported length of the bar and postpone buckling.

On the other hand, the boundary conditions are impacted by compressive strain which causes dilation of the concrete core and yielding of the transverse steel. The yielding of transverse steel leads to permanent plastic elongation and eventually increases the unsupported length of bars at subsequent loading cycles. It is the goal of the model presented in this section to capture all of these effects.

5.7.2 Geometric Detailing and Boundary Conditions

To capture localized behavior, the geometry of the finite element model must reflect the conditions in the plastic hinge region precisely. This chapter considers a circular RC column with 2.4 m height and 0.6 m diameter. Longitudinal reinforcement consists of 16 # 6 bars (1.9 cm diameter) and transverse reinforcement is a # 3 spiral (0.95 cm diameter) at 50 mm pitch. As shown in Figure 5.6, a segment of the extreme fiber bar in the plastic hinge region is modeled with Abaqus (software for finite element analysis) since it will experience the

most severe strain demand. One of the most important dimensions in the model is the unsupported length of the longitudinal bar. A number of researchers, including Bae et al. (2005) and Mander (1984), suggested that bar buckling over an unsupported length of 6 times bar diamter should be avoided to maintain ductile behavior of the structural member. As a result, unsupported lengths exceeding 6 times bar diameter are not considered in this model. (The unsupported length of a #6 bar over 50 mm spiral pitch is $2.7d_b$). However, it has been observed in multiple experimental tests (Goodnight et al. 2013) that longitudinal bars could buckle over more than one spiral layer. To include bucking over multiple spiral turns, the length of the bar modeled above the top of footing is 17.8 cm which contains three spiral layers. The corresponding length to diameter ratio is 9.3. This length to diameter ratio is large enough to cover the possible buckling length suggested by Bae et al. (2006). In the case of a larger bar diameter, a similar length to diameter ratio should be used. The width of the concrete core is equal to the circumferential spacing of the longitudinal bars, as shown in Figure 5.6. The bottom portion of the bar is inserted into a concrete tube to simulate the development of the reinforcement in the footing and to model the bond slip. The development length 8.6 cm in the concrete tube is determined by matching the magnitude of slip at the specific strain level to test results. The cover concrete is not modeled since it is likely to spall under cyclic loading before bar buckling occurs cover concrete provides little resistance to outward bar displacement. Transverse reinforcement is located against the core concrete and the longitudinal bar to provide lateral restraint. To avoid overestimation of the restraint from the transverse steel, the modeled spiral is extended to the location of adjacent bars and fixed at their locations. Since both the model itself and the loading are symmetric, only half of the system is analyzed.

The spirals or hoops are the primary source of resistance for bar buckling. In addition, the spiral provides confinement for the core concrete. Therefore, it is important to ensure an accurate model of lateral stiffness from the transverse steel. In a reinforced concrete column, the spiral turns are in firm contact with the longitudinal reinforcement. Theoretically, the contact area is infinitely small if both the spiral and bar have ideal circular cross sections. To define the interaction between the longitudinal bar and spiral in the finite element model, a

contact area is required to transfer the stresses. The ideal infinitesimal contact area should be avoided to prevent stress concentration. As a result, the spiral in the model is treated as a square section which has identical area and moment of inertia as shown in Figure 5.7. The cross sectional area and moment of inertia determine the axial and flexural stiffnesses respectively. Therefore, the equivalent square spiral provides identical lateral restraint to bar buckling and confinement of the core concrete.
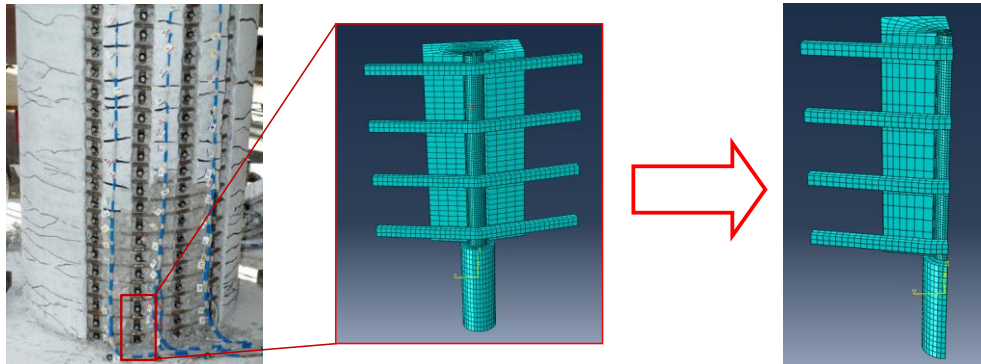
Figure 5.6. Geometry of the Model
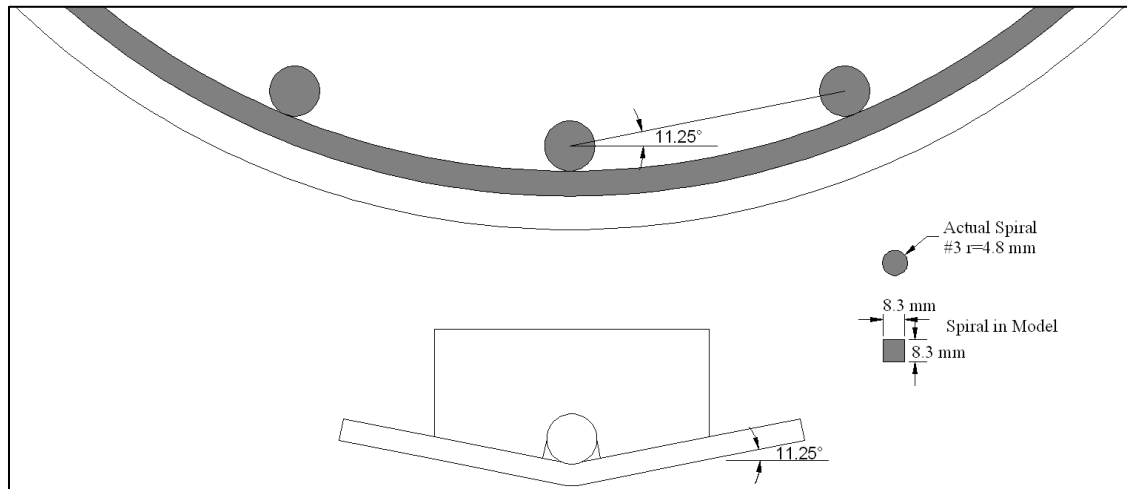
Figure 5.7. Spiral Configurations

5.7.3 Material Models

As shown in Table 5.2, different materials are assigned to the parts of the bar buckling model. The plasticity model developed by Lemaitre and Chaboche (1990) is utilized to define the inelastic behavior of the reinforcing bar and transverse steel. The evaluation and shift of the yield surface are defined by several hardening factors, as shown in Figure 5.8. The kinematic hardening behavior of the steel is defined using the data from material tests for both longitudinal bar and spiral. There is usually very limited isotropic hardening behavior observed in the structural steel. Therefore, no isotropic hardening is considered in the spiral, while the steel material in the longitudinal bar contains a limited amount of isotropic hardening, according to Nip et al. (2010). The concrete material is simulated with a combination of elastic and plastic models based on the modification of Lee and Fenves (1998) to the plasticity model proposed by Lubiner et al. (1989). Under compressive stress,

the resultant lateral expansion of the core concrete loads the spiral and consequently alters the boundary condition. The plasticity theory implements the non-associated potential plastic flow with a Drucker-Prager hyperbolic function to simulate the material behavior under multi-directional confinement. The dilation angle in the Drucker-Prager hyperbolic function dominates the expansion behavior of the concrete under uniaxial loading. While there is not a commonly accepted value of the dilation angle, Malm (2006) showed that a dilation angle ranging from 20 to 40 degrees has only a minor impact on the structural response. However, excessive expansion of concrete under low axial compressive loads has been observed at dilation angles larger than 30 degrees. In addition, Alejano and Alonso (2005) stated that increasing the degree of confinement and plastic strain reduces the dilation angle. Since the hyperbolic function assumes a constant dilation angle, a small value should be utilized and, in this study, the dilation angle is assumed to be 20 degrees. The Damaged Plasticity Concrete model in Abaqus considers damage in terms of a combination of the degradation of material stiffness on reloading and the rapidity of strength recovery as shown in Figure 5.9. The strength degradation has been represented approximately with the unique loading method discussed later. Therefore, no additional damage of the concrete material was defined. Lastly, damage in the footing concrete is assumed only in terms of bond slip. The concrete in the footing is assumed to remain elastic.

Figure 5.8. Limit of Yield Surface Development from Abaqus Analysis User's Manual

6.11 (2010)

Figure 5.9. Recovery of Compression from a Tensile Loading Cycle from Abaqus

Analysis User's Manual 6.11 (2010)

Table 5.2. Material Properties

Material	Parameter	Value (MPa)
Concrete	Compressive Strength	42
	Elastic Modulus	30680
Steel in the Longitudinal Bar	Yield Strength	469
	Elastic Modulus	200000
Steel in the Spiral	Yield Strength	510
	Elastic Modulus	200000

5.7.4 Interactions

Interactions between the different parts of the model are defined in terms of normal behavior and tangential behavior. The normal behavior of all interactions is considered as hard bearing which allows separation but prohibits penetration of the two contacting objects. The tangential behavior of all the interactions is defined in terms of friction. The bond between the reinforcing bar and the core concrete will be severely damaged under large tensile strains which results in large flexural cracks. Therefore, very low tangential friction is modeled in the interaction between the longitudinal bar and core concrete. In contrast, assuming less damage is in the footing, a much larger coefficient of friction on the tangential behavior between the longitudinal bar and footing tube is defined.

5.7.5 Loading Method

The loading on the finite element model is static displacements at the top of the longitudinal bar and the concrete block with displacements which produce an average bar strain of the desired magnitude. To limit computational time, prediction of concrete cracking, its spacing and location, is not simulated in the model. However, capturing the longitudinal bar bucking mechanism requires the presence of cracks to cause instability in the

reinforcement according to Moyer and Kowalsky (2003). Both confining and restraining effects of the spiral are passive mechanism which will be activated by core concrete dilation and the onset of longitudinal bar buckling. Moyer and Kowalsky (2003) concluded that longitudinal bar buckling was likely to occur before cracks close, where bars serve as the sole source of stability. In contrast, the confining effect can only be activated while concrete is under compression. In summary, the impacts of cracks on longitudinal bar buckling are to cause instability in reinforcement upon reversal from significant tensile loading prior to the confining effect in concrete.

The recovery of compressive strength after crack closure was indicated in the test results from Goodnight et al. (2012). A loading cycle of force-deformation response from an experimental test is displayed in Figure 5.10. At the reversal of loading from point A to point C in Figure 5.10, the stiffness increases at Point B where crack closure was observed. The recovery of compressive strength of concrete was also observed in the fiber-based model prediction. It is noted that the stiffness increase at the crack closure point is more profound in the prediction as shown in Figure 5.10. The fiber-based model assumes the cracked section remains plane such that the crack will close as soon as the curvature of this section (or concrete strain) becomes zero upon reversal from tension. At this point, the concrete compressive stiffness will increase rapidly. However, the occlusion of aggregates in a cracked RC member is not as perfect as the model assumes. As a result, the recovery of stiffness during crack closure in a test is a relatively smooth process and not as sudden as the model predicts.

To capture longitudinal bar buckling, the model must duplicate the crack closure boundary condition upon reversal of loading. The model utilizes a simple solution which assumes that the concrete has cracked and that only the reinforcing bar resists tension. On the subsequent compressive cycle, the concrete block is not compressed until the displacement at the top of the bar reaches the top of the concrete block. Both the bar and the concrete core will be compressed to the target strain level from this crack closure point. As discussed in the tension-based bar buckling theory, the onset of bar buckling will occur before the concrete

block is under compression. Therefore, out-of-plane deformation from the onset of bar buckling is expected to be observed before cracks close. However, this deformation is usually small and will become much more obvious as the compressive loading increases.
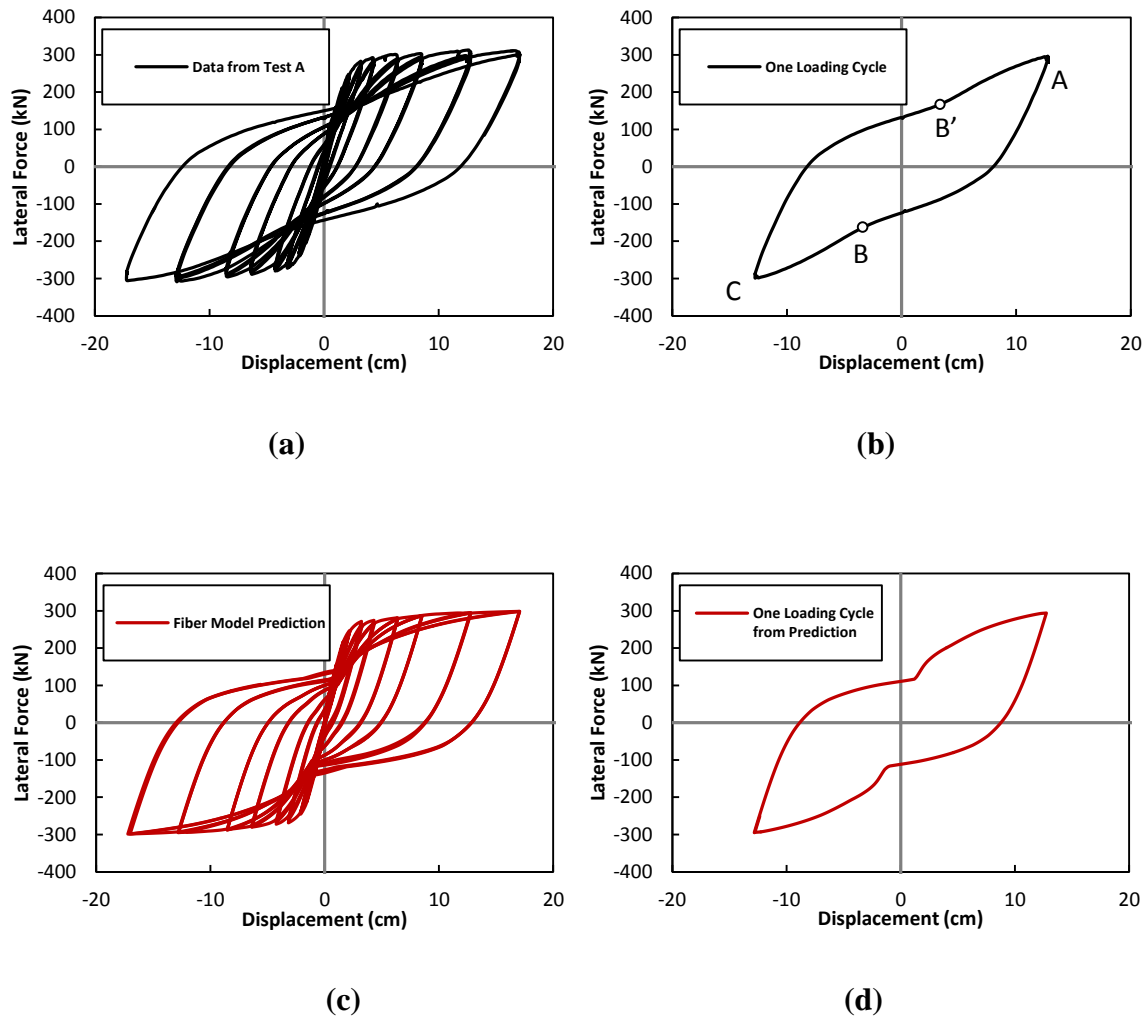
Figure 5.10. Force-Deformation Response from Test 9 and Simulation

5.8 Model Validation

A research program on load history effects is ongoing at North Carolina State University. This program consists of extensive large scale tests on reinforced concrete bridge columns and analytical studies using finite element methods. More than 20 circular columns, as shown in Figure 5.11, were subjected to quasi-static tests with a series of column top displacement histories. The displacement histories include the three-cycle-set and earthquake displacement histories. Nonlinear time history analyses were conducted with a fiber-based model and selected ground motions from large magnitude earthquakes. The displacement response from the column model was utilized as the control displacement for the tests. The experimental data are implemented to calibrate both the fiber-based model and finite element bar buckling model. Goodnight et al. (2012) described the Optotrak sensor system used in these tests to record the displacements at a series of points along exposed reinforcing bars. The strain profiles along a reinforcing bar were generated by calculating the difference in position between two adjacent LED markers. Specimens were loaded until longitudinal bar buckling occurred. To validate the finite element bar buckling model, the strain history which a buckled bar experienced in the experiment was applied to the bar buckling model.

5.8.1 Introduction of Test Results

The experimental data from two tests was implemented to validate the behavior of the bar buckling model. Strain histories from Tests A and B were utilized as input into the finite element bar buckling model. The behavior of the model was compared to the observations from both tests. The specimens in both tests had identical geometry and reinforcement detailing.

Test A and B were selected because of their distinct loading histories. Test A employed a three cycle set load history, which represents an extreme case of an earthquake with multiple loading reversals and large energy input, as shown in Figure 5.12. The average strain from the bottom three gauges was imposed on the bar buckling model in an attempt to capture the bar buckling. The reinforcement in the specimen of Test A experienced a large

number of loading cycles before it reached the critical tensile strain prior to buckling upon load reversal. In contrast, the load history of Test B is from the Kobe, 1994 Japan earthquake and contains a limited number of large displacement pulses. Therefore, the results from these two tests represent extreme cases of displacement history. In addition, the extreme fiber at the two faces of the specimens in Test A and B experienced different tension-compression strain histories. One of the extreme fiber bars in Test B sustained a large tension strain and a subsequent compression strain while the other extreme fiber bar was subjected to a large compression strain first, a subsequent tension strain and then a compression strain again. Therefore, buckling of the two extreme fiber bars was observed in different loading cycles, as shown in Figure 5.12 and Figure 5.13. The displacements towards the south in Figure 5.12 were considered to be positive.
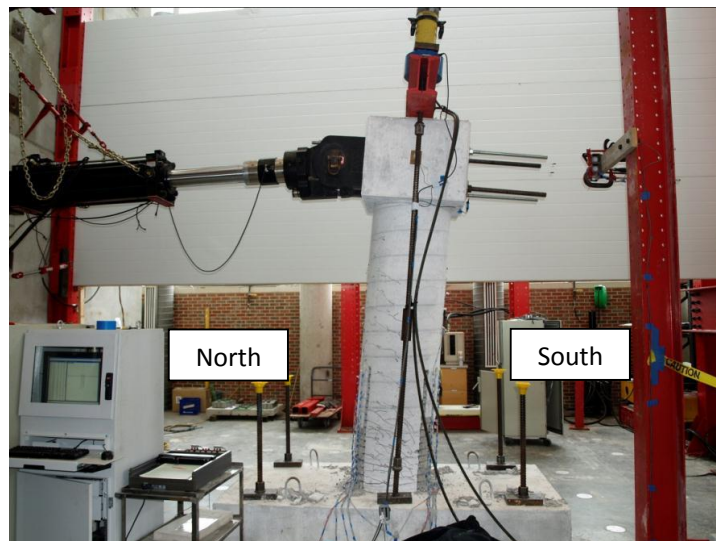
Figure 5.11. Setup of Experimental Tests
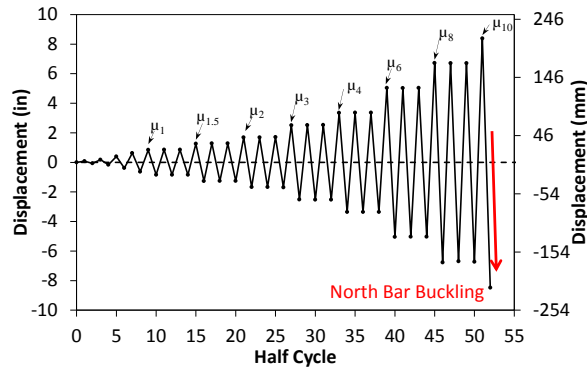
(a)
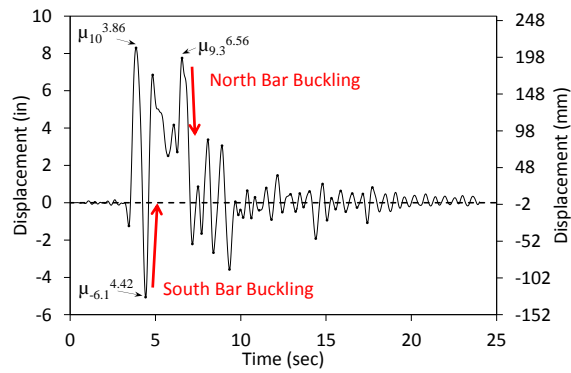
(b)

Figure 5.12. Loading History from Test A (a) and Test B (b)

(a)

(b)

Figure 5.13. Reinforcement Buckling in Test A (a) and Test B (b)

5.8.2 Comparison between Model Prediction and Observation of North Bar from Test B

In Test B, the extreme fiber bar on the north side of the specimen was observed to buckle after a few cycles of loading. Figure 5.5 showed that the reinforcement on the north side of the specimen would be subjected to tension under the loading in south direction

(positive). The Kobe load history has a large positive (south) displacement cycle at the beginning as displayed in Figure 5.12. Therefore, the extreme fiber bar on the north side of the specimen was subjected to a large tensile strain, and upon reversal, bar buckling was expected. However, the bar did not buckle until reversal of loading from the displacement ductility 9.3 at 6.56 sec shown as $\mu_{9.3}^{6.56}$ in Figure 5.12.

As discussed, the strain history up to the time that bar buckling was applied to the finite element model. For the bar on the north side of specimen B, there were four displacement ductility levels before the bar buckled, including $\mu_{-1.5}^{3.44}$, $\mu_{10}^{3.86}$, $\mu_{-6.1}^{4.42}$ and $\mu_{9.3}^{6.56}$. Figure 5.14 displays the corresponding strain profiles of the north extreme fiber bar at the four displacement ductility levels. The strain demand applied to the buckling model is obtained by averaging the strain data points at the three bottom gauges, as shown in Table 5.3. A strain history of -0.0025, 0.055, -0.004, 0.051, and -0.0018 was applied to the bar buckling model, as shown in Figure 5.14. A complete loading cycle consists of two branches of monotonic loading. The half cycle number is thus utilized to define the loading in Figure 5.14 and subsequent figures. An ideal computational result would include the following: 1) no buckling upon reversal from $\mu_{10}^{3.86}$, 2) buckling upon reversal from $\mu_{9.3}^{6.56}$, and 3) spiral yielding when the longitudinal bar buckles.

Figure 5.15 shows the model behavior and longitudinal plastic strain distribution at each peak loading point. The stages of loading are denoted by the average strain on the longitudinal bar. Figure 5.15(b) shows that no plastic strain was developed at the average strain -0.0025. The strain distribution in the bar is relatively uniform at the average strain -0.055, as shown in Figure 5.15(c), and large plastic strains in the longitudinal bar are observed. For the compressive cycle at the average strain -0.004, the non-uniform strain distribution in the longitudinal bar was developed. Dilation of the core concrete activated the confining effect of the spirals, but did not yield the spiral. The longitudinal bar buckled upon reversal from the average tensile strain 0.051, as shown in Figure 5.15(f). The plastic strain distribution is significantly non-uniform in the buckled region. Tensile strain is observed at

the outside face even in this compressive cycle and large compressive strains are concentrated on the inner face of the bar.

As shown in Figure 5.16, the model predicts the buckling to occur at the same cycle as observed in the experimental test. In addition, the model illustrates the accumulation of strain non-uniformity across the longitudinal bar upon reversals from tensile strains. The strain non-uniformity developed upon reversal from the average tensile strain of 0.055 to -0.04 and caused a minimal deformation in the longitudinal bar. Loading upon reversal from the average tensile strain of 0.051 led to an eccentricity of the compressive load which resulted in inelastic bar buckling. Bae et al. (2008) also showed the effect of 'minimal bar deformation' or 'eccentricity' on the required buckling stress. Unlike the model described in this chapter, they induced fictitious deformations in the bar, while the strain history leads to bar deformations in the finite element model. Spiral yielding in the buckled region was also captured (Figure 5.17). Bar buckling occurs with large out-of-plane deformation and plastic strains in spiral layers.

Table 5.3. Strain History Values

	Compressive Strain					Tensile Strain			
Time	Gauge 1	Gauge 2	Gauge 3	Avg.	Time	Gauge 1	Gauge 2	Gauge 3	Avg.
3.44	-0.0029	-0.0024	-0.0021	-0.0025	3.86	NA	0.053	0.057	0.055
4.42	0.0015	-0.012	-0.0014	-0.0040	6.56	NA	0.048	0.053	0.051
7.16	NA	NA	NA	-0.0018					
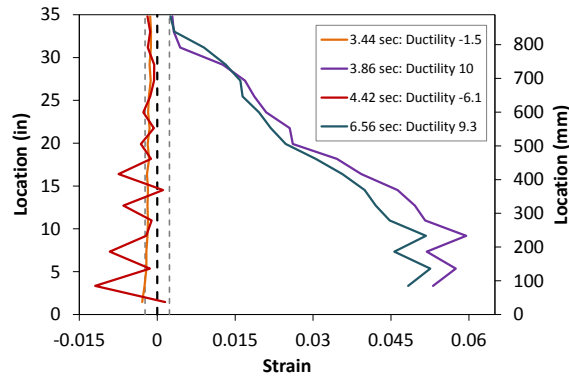
(a)
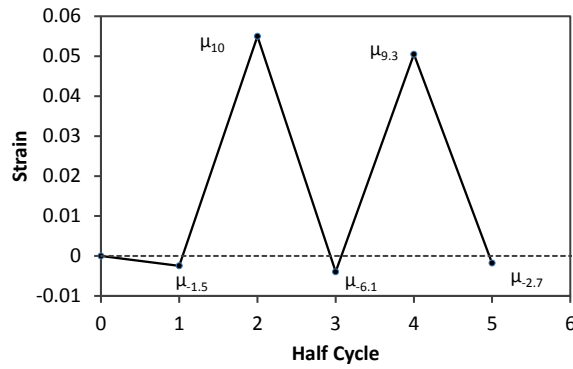
(b)

Figure 5.14. Strain Profile (a) and Strain History (b) of North Extreme Fiber Bar from Kobe Load History
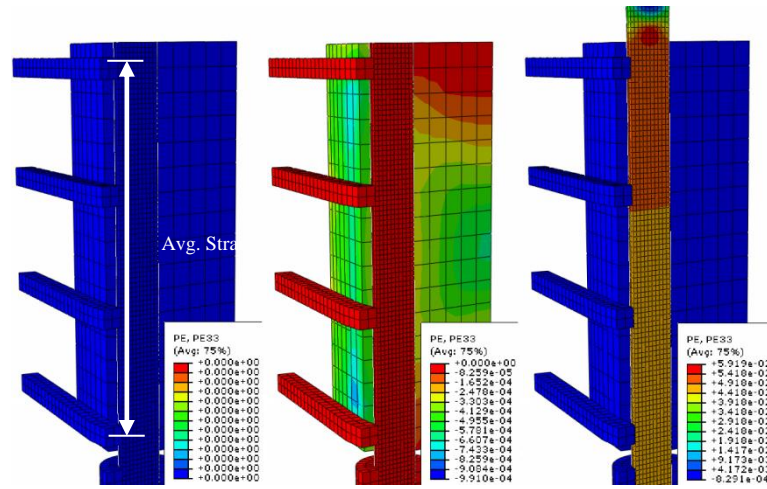
(a) Strain: 0   (b)Strain: -0.0025   (c)Strain: 0.055
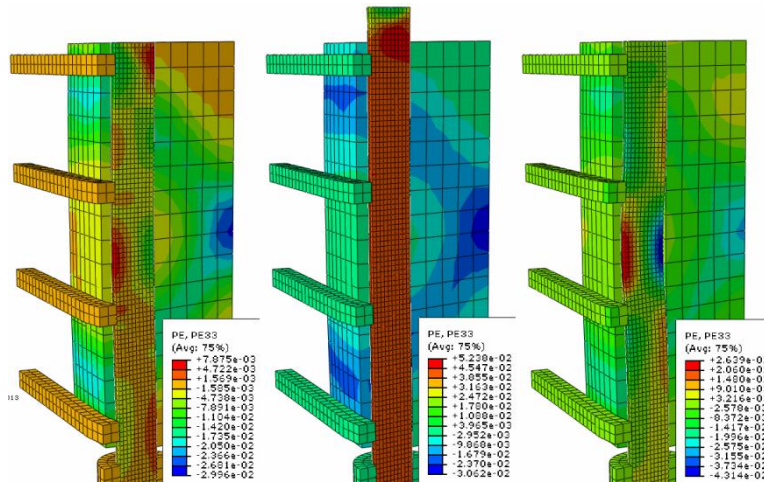
(a) Strain: -0.004 (b)Strain: 0.051   (c)Strain: -0.0018

Figure 5.15. Loading Process with Strain History from Test B (North Bar)
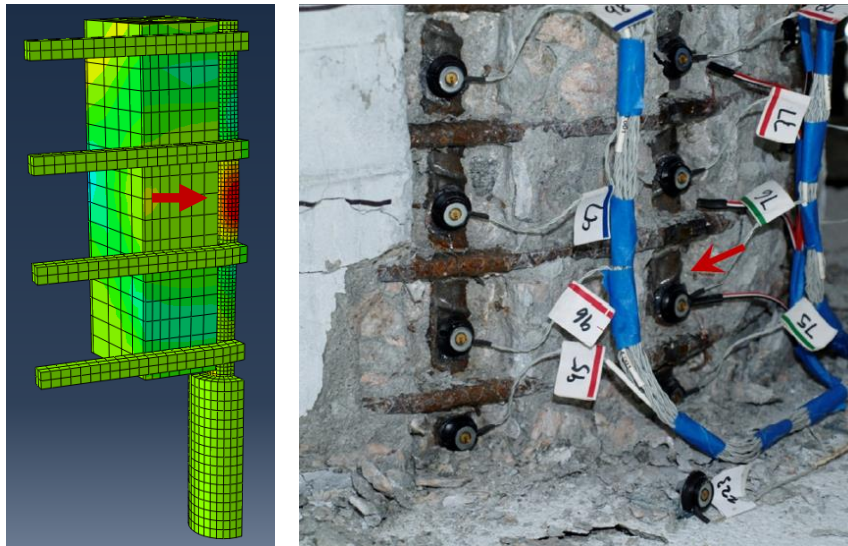
Figure 5.16. Predicted and Observed Longitudinal Bar Buckling
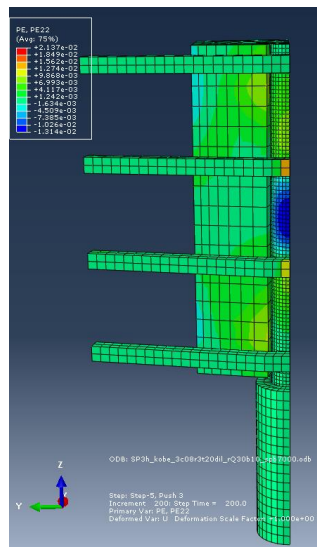
Figure 5.17. Yielding of Spiral in the Buckled Region

5.8.3 Comparison between Model Prediction and Observation of South Bar from Test B

In multiple experimental tests, the reinforcing bars buckled at the location where the spiral yielded in a previous loading cycle. The extreme fiber bar on the south side of the specimen for Test B buckled under these conditions. The measured strain history of the south extreme fiber bar was applied to the model to assess its ability to capture spiral yielding prior to buckling when subjected to this load history.

Figure 5.18 shows the strain gradient in the plastic hinge at peak displacement ductility level of 10 (8.4in, 21cm) and peak displacement ductility of -6.1 (5.1in, 13cm). As shown in Table 5.4, the strain levels at the bottom three gauges (2in, 50mm gauge length) from the strain profiles were extracted from the data and averaged. The target strain in the third cycle, which refers to 4.84 sec in the original time history response, is not available from the Optotrak system data since the bar had already buckled. The difference in position of two adjacent LED markers does not correspond to engineering strain since the bar no longer deforms uniaxially. Therefore, as shown in Eq.5.4 the peak displacement at 4.84 sec was used to linearly interpolate the stain from the loading cycle of 3.86 sec. Again, the recorded strain history from Test B was applied to the finite element bar buckling model. As before, the results from the bar bucking model are compared to the observations from the test to assess its performance.

$$\frac{\Delta_1}{\Delta_2}\varepsilon_2 = \frac{5.5}{8.4} \times \text{-}0.023 = \text{-}0.015$$

5.4

The model behavior and plastic strain distribution at each peak loading point is shown in Figure 5.18. Two spiral layers yielded under a compressive strain of -0.023 as observed in the test, as shown in Figure 5.21. The plastic deformation of the spirals from this compressive cycle increased the unsupported length of the bar which resulted in development of inelastic bar buckling before crack closure. The model predicted the onset of buckling before any compressive load on the concrete was applied, as shown in Figure 5.19(d). In

addition, profound outward deformation confirms bar buckling at the peak compressive strain of -0.015. The predicted and observed buckling deformations are compared in Figure 5.20.

(a)   (b)
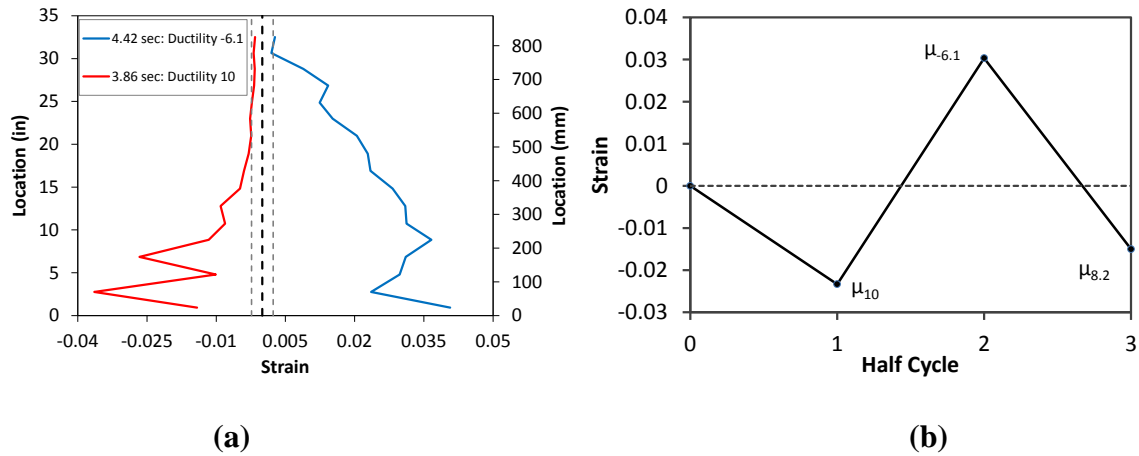
Figure 5.18. Strain Profile (a) and Strain History (b) of South Extreme Fiber Bar in

Kobe Load History
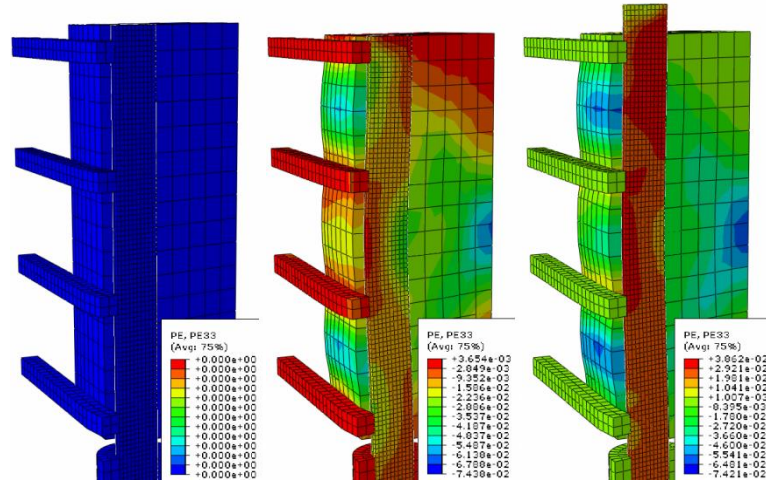
(a) Strain: 0   (b)Strain: -0.023   (c)Strain: 0.031
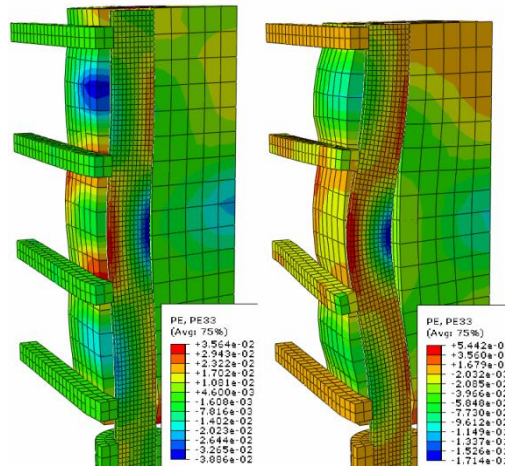
(d)Crack Closure   (e)Strain: -0.015

Figure 5.19. Loading Process with Strain History from Test B (South Bar)
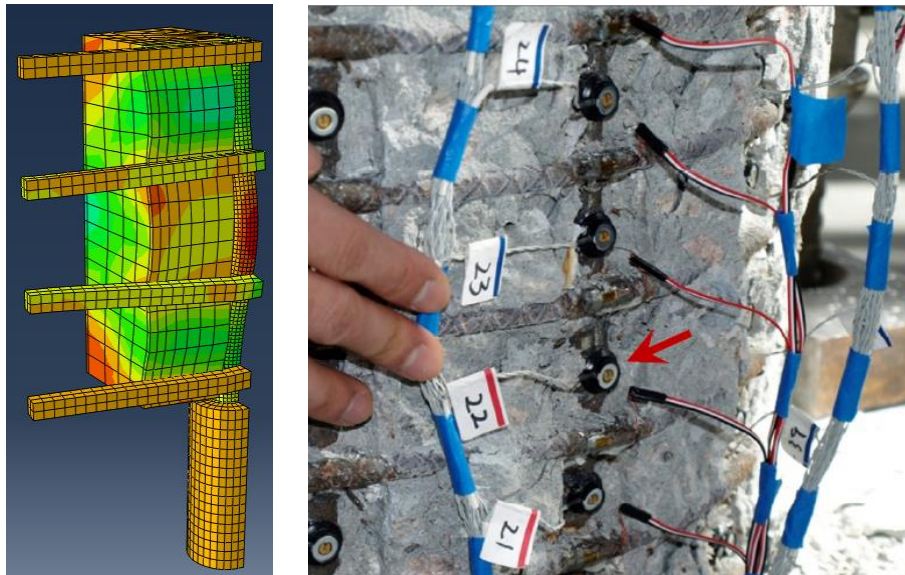
Figure 5.20. Predicted and Observed Longitudinal Bar Buckling

Table 5.4 Target Strain Values

Compressive Strain					Tensile Strain				
Time	Gauge 1	Gauge 2	Gauge 3	Avg.	Time	Gauge 1	Gauge 2	Gauge 3	Avg.
3.86	-0.037	-0.013	-0.02	-0.023	4.42	0.027	0.031	0.033	0.031
4.84	N.A.	N.A.	N.A.	-0.015					
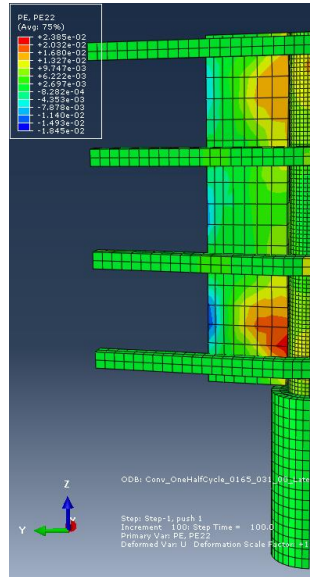
Figure 5.21. Yielding of Spiral at the Compressive Strain -0.023

5.8.4 Comparison between Model Prediction and Observation of North Bar from Test A

The column specimen of Test A was subjected to a three-cycle-set loading history. Figure 5.12 showed the loading history of the top column displacement. Compared to Test B, more damage was observed in the plastic hinge before buckling, such as cover concrete crushing and spalling. A large number of loading cycles at displacement ductility 2 and 4 did not cause yielding of the spiral. However, cumulative plastic strains were observed at each loading cycle at displacement ductility 6, as shown in Figure 5.23. The extreme fiber bar on the north side of the column buckled upon reversal from a displacement ductility of 8.

Figure 5.22 portrays strain profiles of the extreme fiber bar on the north side of the column. As discussed, the strain history applied to the bar buckling model was obtained by

averaging the strain within the six inch region above the column-footing interface. Since strain profiles do not change significantly from cycle to cycle at the same ductility level, the average strains are assumed to be constant in all three cycles at the same displacement ductility. Elastic cyclic loadings and cycles at displacement ductility 1 were neglected. However, for the three-cycle-set, the strain history needs to include most of the peak strains because every specific strain level is equal or larger than the strain in previous cycles.

As previously discussed, it is not reliable to use strain data from the Optotrak system at the first compressive cycle of ductility 8 where the bar buckled. Eq. 5.4 was utilized to linearly extrapolate the strain from the previous cycle. Table 5.5 lists all the strain values from three base gauges of the strain profile. The target strain history is shown in Table 5.5.

As shown in Figure 5.24 (b), the dilation of the core concrete caused a non-uniform strain distribution in the longitudinal bar, at a displacement ductility level of 2. The non-uniform strain and small deformation in the bar can be considered as an imperfection or eccentricity in subsequent loading cycles. The transverse reinforcing steel restrained the bar from buckling at low ductility levels. As marked by the red ellipse in Figure 5.24(i), the strain along the outside surface of the bar remains in tension during compressive loading cycles. This residual tensile strain at the outer surface of the bar accumulated cycle by cycle. Similarly, the residual compressive strain accumulates around the inside surface of the bar. The degree of eccentricity increased from cycle to cycle, and a large restraining capacity from spirals was required to prevent buckling. In addition, both the test result and model prediction show that the plastic strain in the spiral accumulates at loading cycles corresponding to displacement ductility of 6 as portrayed in Figure 5.23. As the plastic deformation in the spiral increases, the unsupported length of the bar is altered. Bar buckling occurs at the first compressive cycle of displacement ductility 8 due to the reduction of buckling stress from the accumulation of the imperfection and spiral deformation. The comparison of bar buckling in the model and the experimental test is displayed in Figure 5.25. Note the yielding in several turns of the spiral, as shown in Figure 5.26 and plotted in Figure 5.23.

(a)   **(b)**
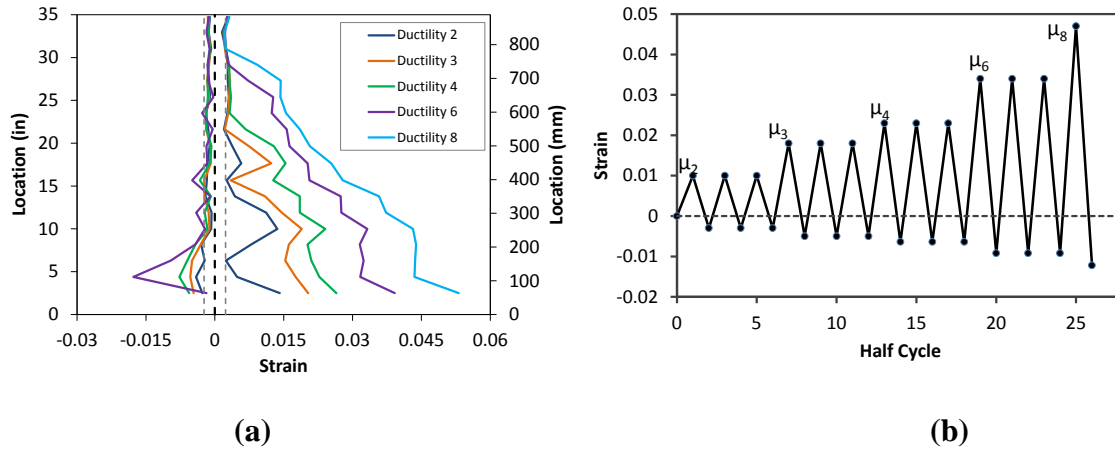
Figure 5.22. Strain Profile (a) and Strain History (b) of North Extreme Fiber Bar in

Test A

Table 5.5. Target Strain Values

	Tensile Strain					Compressive Strain			
Ductility	**Gauge 1**	**Gauge 2**	**Gauge 3**	**Avg.**	**Ductility**	**Gauge 1**	**Gauge 2**	**Gauge 3**	**Avg.**
2	0.014	0.005	0.012	0.010	-2	-0.0027	-0.0041	-0.0022	-0.0030
3	0.02	0.018	0.015	0.018	-3	-0.0046	-0.0054	-0.005	-0.0050
4	0.026	0.023	0.021	0.023	-4	-0.0056	-0.0077	-0.006	-0.0064
6	0.039	0.032	0.032	0.034	-6	-0.0018	-0.0177	-0.0096	-0.0092
8	0.053	0.043	0.044	0.047	-8	N.A.	N.A.	N.A.	-0.0122
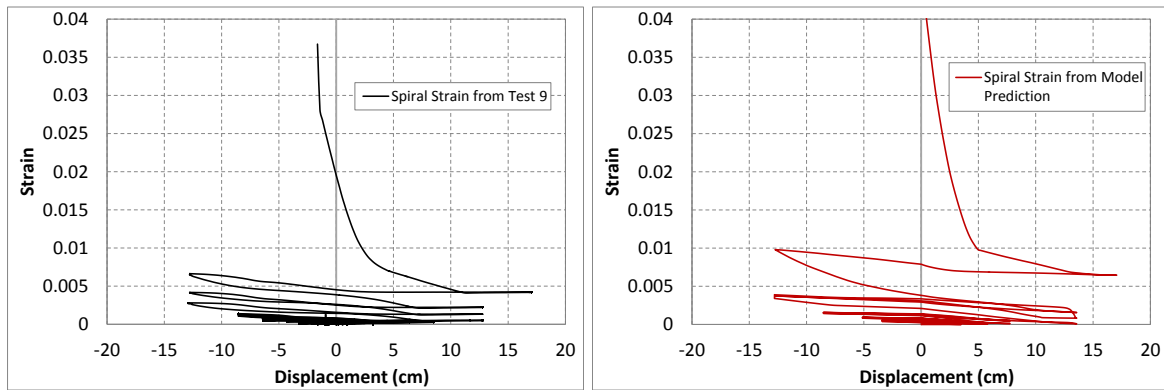
Figure 5.23. Spiral Strain Hysteretic Response

Figure 5.24. Loading Process with Strain History from Test A (North Bar)
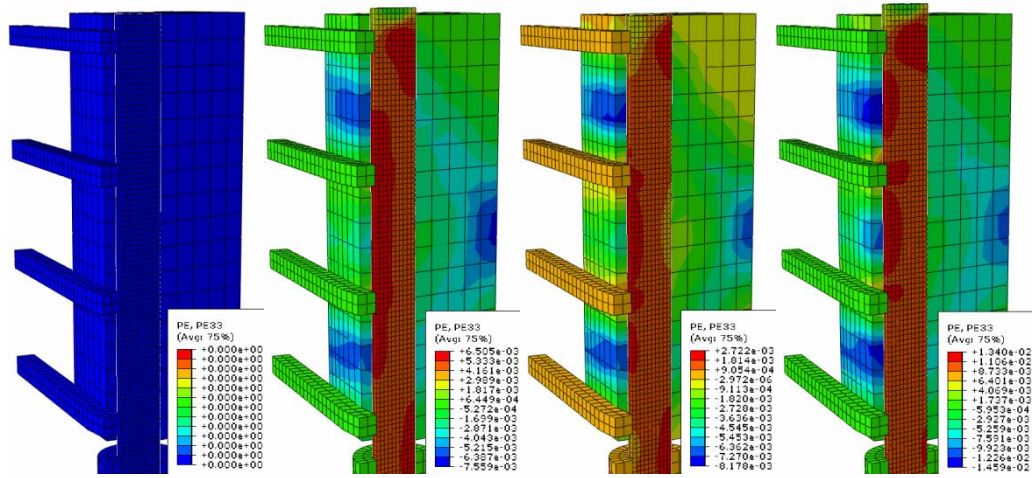
(a)Strain: 0   (b)Strain: 0.01   (c)Strain:-0.003   (d)Strain:0.018
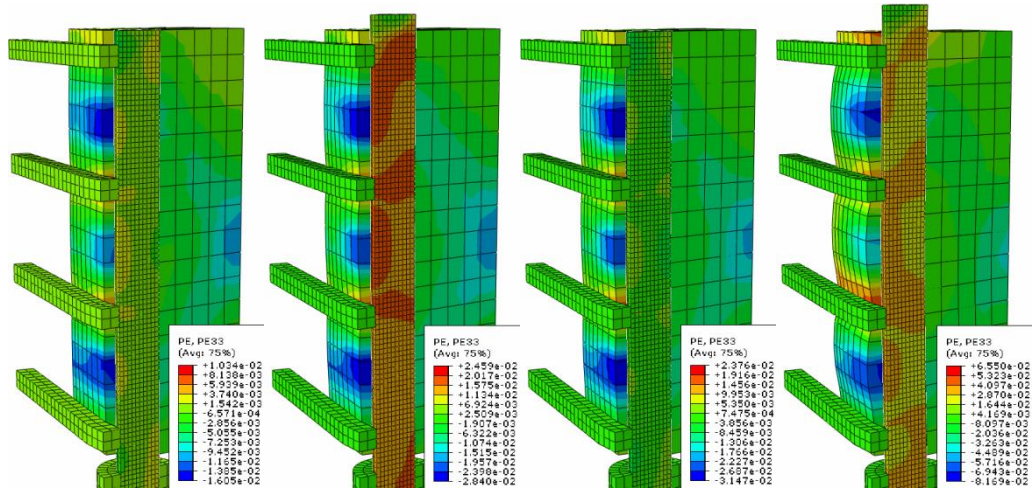
(e)Strain: -0.005   (f)Strain: 0.023   (g)Strain: -0.0064   (h)Strain: 0.034

(i)Strain: -00.0092   **(j)Strain: 0.047**   **(k)Strain: -0.0122**
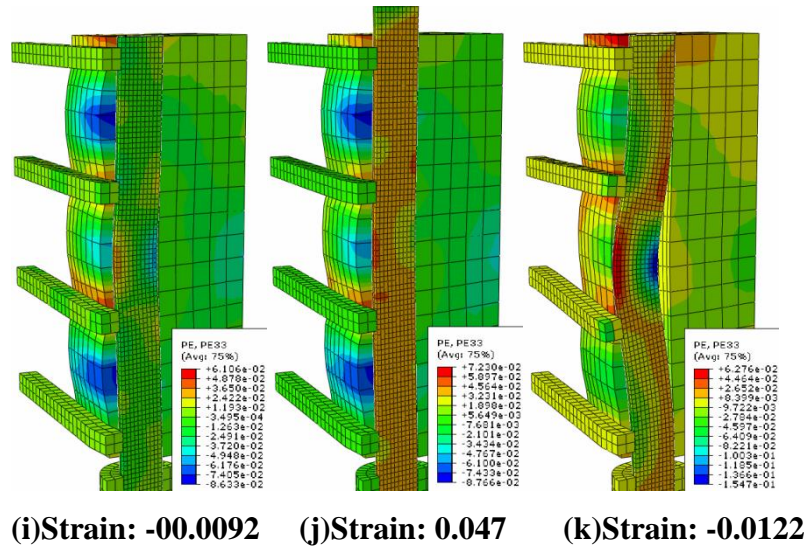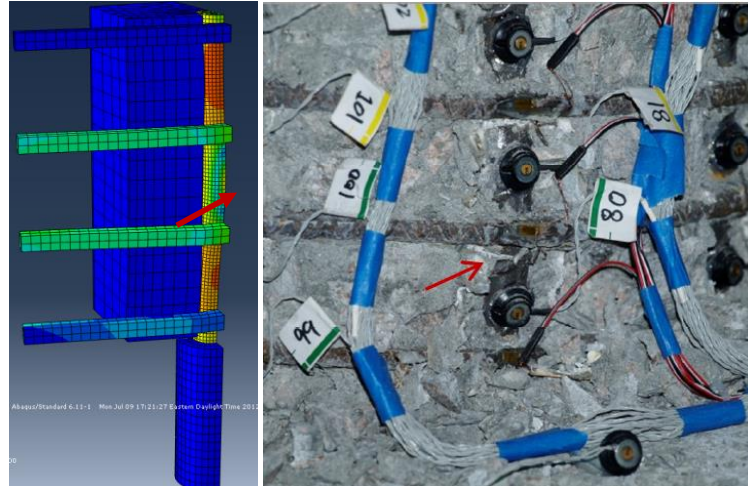
Figure 5.25. Comparison of Bar Buckling between the Test Result and Model

Prediction
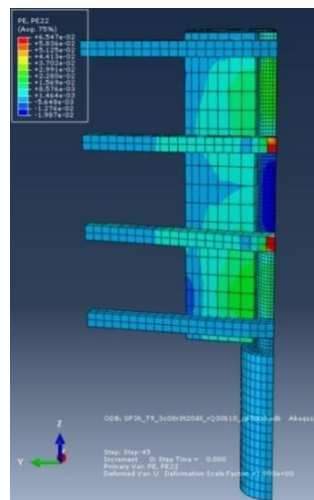
Figure 5.26. Yielding of Spiral at Buckling Region

5.9   Summary of Findings

Several factors have been found to determine the inelastic bar buckling in RC members, as listed in

Table **5.6**. It has been suggested by the finite element analysis that the compressive strain in core concrete can cause imperfection in the longitudinal bars which lead to large plastic deformations of the spiral which, in turn, alters the unsupported length at later loading cycles. The case study with tangent modulus theory for inelastic bar buckling explains the importance of reversal from a significant tensile strain on both the reduction of the tangent modulus and the increase of compressive stress in the bar. As the steel material is simulated appropriately, the finite element model also captures the impact of tangent modulus on inelastic buckling. Most importantly, the plastic deformation of spiral turns can cause significant increase of unsupported length of the bar for later compressive cycle. On the other hand, the diameter of the bar and the spiral pitch determine the bar moment of inertia and the original unsupported length respectively. The proposed finite element model will also be able to include the effect of reinforcement detailing on inelastic bar buckling.

Table 5.6. Factors Affecting Inelastic Bar Buckling

Factors	Load/Strain History Related or Not	Evidence
Magnitude of Bar Stress	Yes	Tangent Modulus Theory
Tangent Modulus	Yes	Tangent Modulus Theory
Unsupported Length	Yes	Finite Element Model
Imperfection/Eccentricity	Yes	Finite Element Model

5.10 Chapter Conclusions

Inelastic bar buckling in RC members is a complicated behavior since idealized uniaxial monotonic behavior does not exist. Theoretically, it is impacted by the bar diameter, spiral pitch and stress strain behavior under cyclic loading. However, either the tangent modulus theory or the double modulus theory only explains the inelastic buckling at the material level assuming an idealized uniaxial behavior. The finite element model showed that the strain history affects the unsupported length and imposed imperfections in the bar. The model was established for the purpose of capturing the effect of load history and reinforcement detailing on the inelastic bar buckling.

Presented in this chapter was also a two-step numerical method to accurately predict longitudinal bar buckling under seismic loading. Nonlinear time history analysis with a fiber-based model provides the displacement response of a structure and the associated strain history response in the plastic hinge region. The strain history is then used as the loading for the finite element model to predict bar buckling. The finite element bar buckling model must consider local geometry of the structural member and reinforcement detailing. An earthquake load history will have three major characteristics, including number, magnitude, and degree of symmetry of the loading cycles. Considering these features of a loading history, three strain histories from experimental tests were selected and imposed on the finite element bar buckling model. The model was shown to accurately capture the load history effect on inelastic bar buckling. It is more important that the analytical result decomposed the load history effect into the follow findings: 1) a significant tensile strain is required to activate buckling upon reversal, 2) a single large compressive cycle prior to the tensile cycle can alter the unsupported length of the bar and can create imperfections resulting in subsequent eccentricity, and 3) the cyclic loading causes accumulation of spiral plastic deformations and bar imperfections. All of these load-history-based factors have been shown to influence the onset of inelastic bar buckling.

This numerical method will be implemented to further quantify the effects of the seismic load history and reinforcement detailing on bar buckling. A parametric study with the proposed analysis method is underway, and will include a variety of load histories. The effect of spiral pitch, axial load ratio, aspect ratio and reinforcing bar diameter on bar buckling is also being investigated with the proposed method.

Chapter 6: Deformation Limit States for Longitudinal Bar Buckling

6.1 Introduction

For Performance-Based Seismic Design, accurate estimates of structural performance are of paramount importance. In the case of reinforced concrete bridge columns, a key performance limit state is the onset of reinforcing bar buckling because many engineers consider this damage level as the condition beyond which a structure may require replacement. Previous research (Rodriguez et al. (1999)) has shown that bar buckling is more likely to occur under cyclic loading. In addition, Kunnath and El-Bahy (1997) and Moyer and Kowalsky (2003) observed that the characteristics of cyclic loading impacted the required deformation to produce bar buckling. While empirical models exist that have been developed on the basis of the existing column test database, as presented by Berry and Eberhard (2005), direct consideration of the effect of loading history on reinforcing bar buckling has not been previously included in design.

Modeling of RC structures to capture local damage, such as reinforcing bar buckling, has been shown to be difficult in the past. Several researchers have focused on modeling inelastic bar buckling under monotonic loading, such as Mau and El-Mabsout (1989), Dhakal and Maekawa (2002), Bae et al. (2005), and Urmson and Mander (2012). Zong et al. (2013) observed the buckled shape of reinforcing bars over multiple hoop layers and investigated the stress-strain behavior of bars in a full column finite element model. Independent "Beam-on-Springs" models were also developed to obtain the bar stress-strain behavior after buckling given different reinforcement detailing. Zong et al. (2013) concluded that the post-buckling bar stress-strain response on compression depends on the ratio of buckled length to bar diameter.

Moyer and Kowalsky (2003) observed the influence of tensile strains on the onset of bar buckling, and described a tension-based buckling mechanism. Moyer and Kowalsky (2003)

illustrated the distinct features of the tension-based bar buckling mechanism summarized as follows. First, buckling of reinforcement requires reversal of loading. Second, significant tensile strain is required to activate the tension-based bar buckling mechanism upon reversal. Third, the accumulation of tensile strain over multiple loading cycles impacts longitudinal bar buckling. Lastly, since bar buckling in the end occurs under compression, it is important to quantify the compressive load capacity associated with bar buckling. In order to capture nonlinear bar buckling under cyclic loading, this chapter utilizes a finite element model developed by Feng et al. (2013)[2] to conduct nonlinear analysis of RC bridge columns. The goals of the research discussed in this chapter are to define tensile strain limits and to develop a corresponding design approach for the reinforcing bar buckling limit state that considers the effect of load history.

6.2 Finite Element Model to Capture Bar Buckling

Recent research by Feng et al. (2013)[2] summarized the factors which have the potential to impact inelastic bar buckling. These factors, including the magnitude of bar stress, tangent modulus reduction, unsupported bar length, and bar axial force eccentricity, are strongly related to the loading history that the member is subjected to, and the corresponding strain history of the individual reinforcing bar. As a result, a hybrid finite element method was introduced to study the impact of load history on inelastic bar buckling in RC bridge columns. Feng et al. (2013)[2] utilized fiber-based elements to simulate reinforced concrete columns and conducted nonlinear time history analysis (NTHA) to obtain column displacement response as well as the strain history response of the individual reinforcing bars. The strain history of the longitudinal bars obtained from the NTHA was then used as the forcing function in a local finite element model developed using solid elements, where bar buckling was captured and the effect of strain history on buckling was investigated. Figure 6.1 shows the model mesh and geometry from Feng et al. (2013)[2] which reflect the local detailing in a RC bridge column.

Based on the analysis results, Feng et al. (2013)[2] decomposed the characteristics of load history and their impact on bar buckling in RC members into the following observations: 1) a significant longitudinal bar tensile strain is required to activate buckling upon subsequent loading in compression; 2) a large level of compressive strain demand on the longitudinal reinforcing bar prior to bar buckling alters the unsupported length of the longitudinal bar as the dilation of the core concrete under compression may lead to plastic spiral elongation; 3) additional cycles of loading may cause accumulation of hoop plastic deformation and longitudinal bar imperfection (eccentricity). These load-history-based factors have been shown to influence the required tensile strain which results in inelastic bar buckling upon reversal of loading.
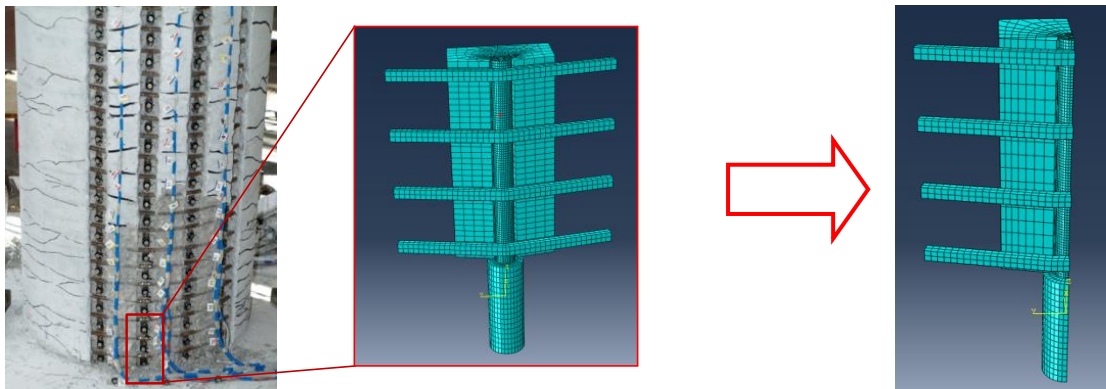
Figure 6.1. Finite Element Model for Bar Buckling from Feng et al. (2013)[2]

6.3 Selection of Ground Motions

Ground motions from large earthquakes were collected from several sources for use in NTHA of the research discussed in this chapter. The ground motions selected were intended to cover several large historical seismic events. Forty ground motions from different earthquakes, including subduction events and strike-slip events, were selected and are shown in Table 6.1. All ground motions have peak ground accelerations greater than 0.4 g. During

the course of the analysis, the ground motions were scaled as much as 150% in order to generate response large enough to initiate bar buckling in the finite element model.

Table 6.1. Ground Motion Database

Earthquake	Year	Station	PGA(g)
Chile	2010	N.A.	0.6
Japan	2011	TCGH	1.22
Kobe	1995	N.A.	0.82
Chichi	1999	N.A.	0.65
		No1197	0.8
		No1231	1
		No1503	0.8
		No1507	0.6
		No1517	1.2
		No2658	1
		No3474	0.8
Tabas	1978	N.A.	0.84
Northridge	1994	SylmarCSE	0.83
		Pacoima Dam	1.6
Darfield(NZ)	2010	GDLC	0.72
Christchurch(NZ)	2011	LPCC	0.88
Calexico	2010	Array11	0.6
Landers	1992	N.A.	0.8
Duzce	1999	Duzce	0.5
		Lamont	0.9
Erzican	1992	N.A.	0.5
Big Bear	1992	N.A.	0.5
Imperial Valley	1979	No160	0.8
		No180	0.5
		No183	0.6
Superstitions Hills	1987	No727	0.8
Managua	1972	No95	0.4
Victoria	1980	No265	0.6
Morgan Hill	1984	No451	1.2
Chalfant	1986	N.A.	0.45

Table 6.1 Continued

Mammoth Lake	1980	No230	0.45
		No231	0.4
Dinar	1995	No1141	0.45
Cape Mendocino	1992	No825	1.5
		No828	0.7
Nihanni	1985	N.A.	1
Loma Prieta	1989	N.A.	0.5
San Fernando	1971	N.A.	1.2
Coalinga	1983	N.A.	0.6
North Palm Springs	1986	N.A.	0.7

6.4 Impact of Load History on Buckling Mechanism

Previous researchers (Moyer and Kowalsky (2003) and Kunnath and El-Bahy (1997)) have shown the impact of load history on reinforcing bar buckling. While longitudinal and transverse bar diameters and bar spacing have long been known to impact the onset of bar buckling, for initial analysis, load history was the only variable. Analyses were conducted on a circular RC column 2.4 m in height and 0.6 m in diameter. Longitudinal reinforcement consists of 16 #6 bars (1.9 cm in diameter) and transverse reinforcement is a #3 spiral (0.95 cm diameter) at 5 cm pitch.

The column was modeled using fiber-based elements, the details of which are noted in Feng et al. (2013)[1] and NTHA was conducted to obtain top column displacement response and reinforcing bar strain history. Each analysis under the effect of a specific ground motion provided two strain histories, one for each of the two bars located furthest from the section center since these bars are more vulnerable to buckling than other bars in the section. Therefore, a total of 80 strain histories were collected for use in the finite element bar buckling model, the details of which are discussed in Feng et al. (2013)[2]. If the strain history failed to generate bar buckling in the finite element bar buckling model, the associated ground motions were scaled up to 1.5 times the original record. However, there were a number of ground motions that still failed to provide severe strain history and cause bar buckling in the finite element analysis. Only the ground motions and their corresponding load history which were able to generate bar buckling under limited scaling factor were utilized to study the effect of load history on reinforcing bar buckling. Over-scaling and arbitrary manipulation of ground motions were avoided in order to maintain the load history characteristics of real earthquake events.

As discussed, the strain histories from the fiber-based analyses results were used as the displacement-controlled loading input into the finite element bar buckling model developed by Feng et al. (2013)[2]. In the work described in this chapter, bar buckling was said to have occurred if the outward displacement of the longitudinal bar reaches 0.1 times the bar

diameter. The outward displacement limit is empirical and is based on the work of Massone and Morader (2009) and Bae et al. (2005) where a large reduction of bar strength was observed after buckling with an eccentricity larger than 0.1 times the bar diameter.

6.4.1   Load History Analysis Results

The results from the finite element analysis showed that bar buckling occurred under 14 strain histories (Figure 6.2), which were from 12 of the 40 NTHAs. This means that twelve earthquakes successfully lead to bar buckling while only two of them (Kobe and Chichi Station 1503) buckled both extreme fiber bars in the column. The arrow on the load histories in Figure 6.2 refers to the loading cycle in which bar buckling was observed in the analysis. The location of Bar 1 and Bar 2 with respect to the displacement direction is shown in Figure 6.3. Table 6.2 lists the earthquake ground motions which generated bar buckling.

Table 6.2. Earthquakes Causing Bar Buckling

Earthquake	Station	Scaling Factor	Buckled Bar
Tabas	N.A.	1	Bar 2
Darfield	GDLC	1	Bar 2
Chichi	No 1197	1.1	Bar 1
Chichi	No 1503	1.1	Both
San Fernando	N.A.	1.2	Bar 2
Northridge	Sylmar(CSE)	1.2	Bar 2
Kobe	N.A.	1.2	Both
Japan 2011	TCGH	1.2	Bar 2
Morgan Hill	No 451	1.3	Bar 1
Duzce	Duzce	1.4	Bar 1
Cape Mendocino	No 828	1.4	Bar 2
Coalinga	N.A.	1.4	Bar 1

Figure 6.2. Longitudinal Bar Strain Histories and Buckling

(a)

(b)

(c)

(d)

(e)

(f)

(g)

(h)

(i)

(j)

(k)

(l)

(m)

(n)
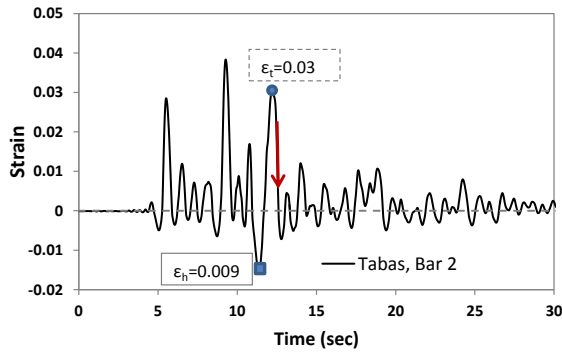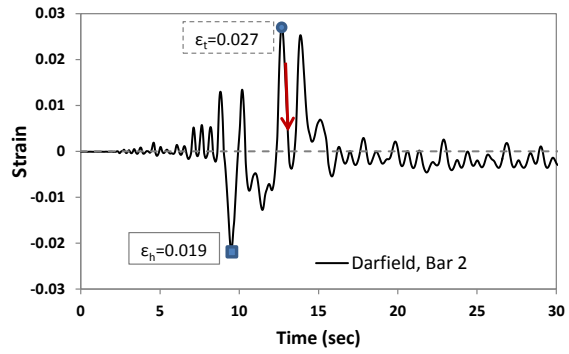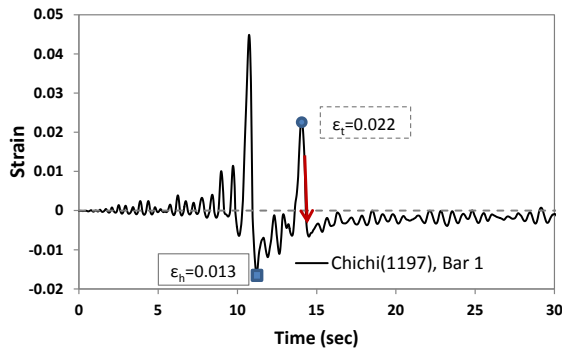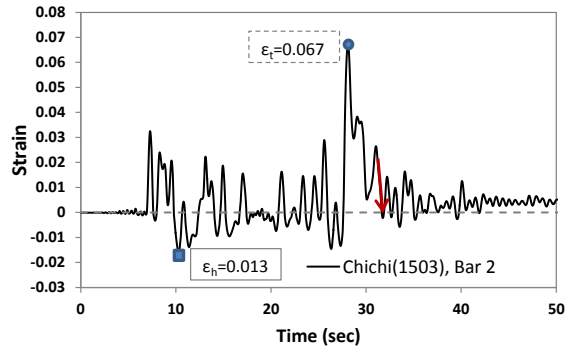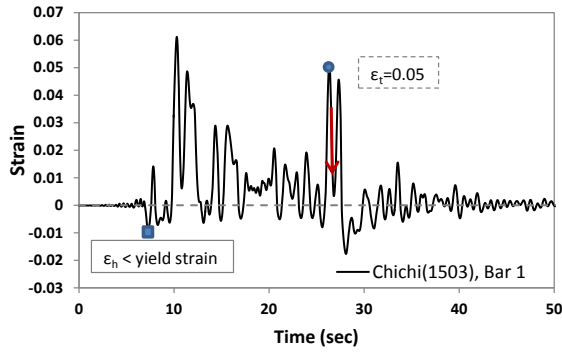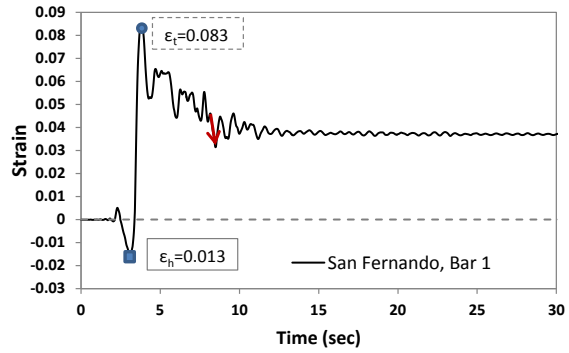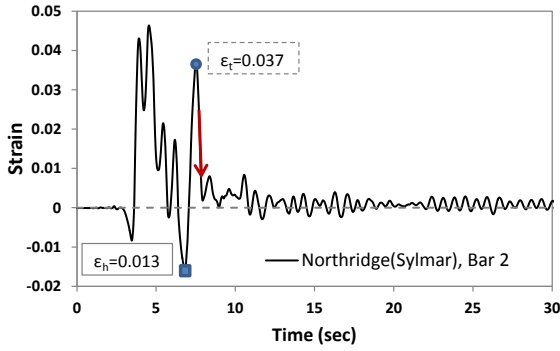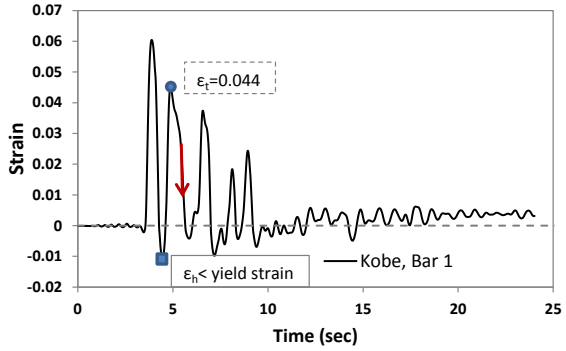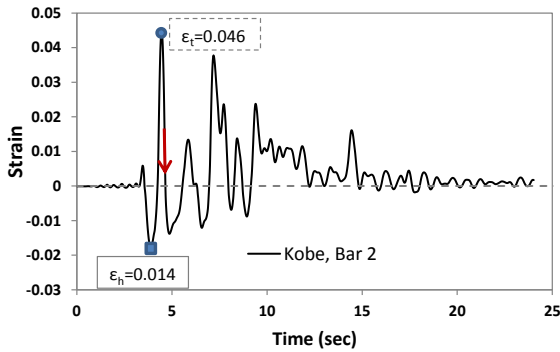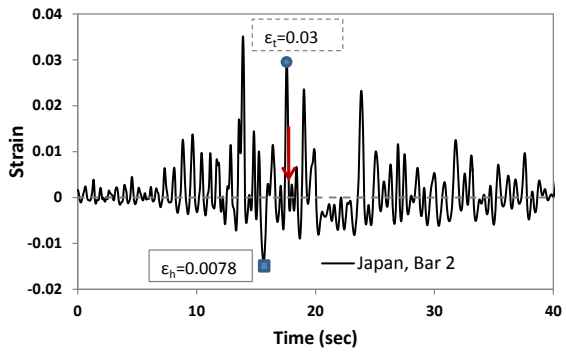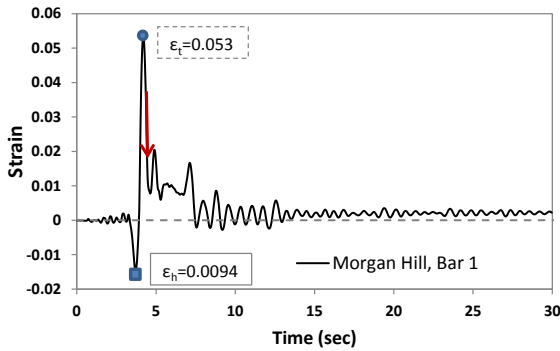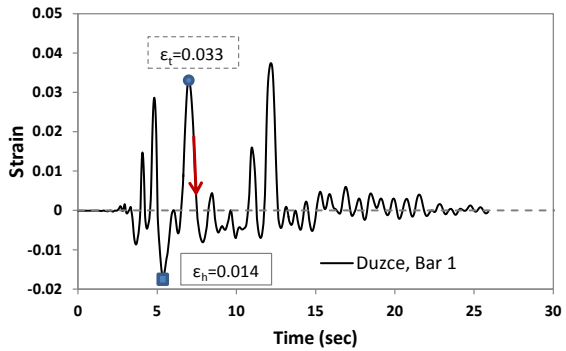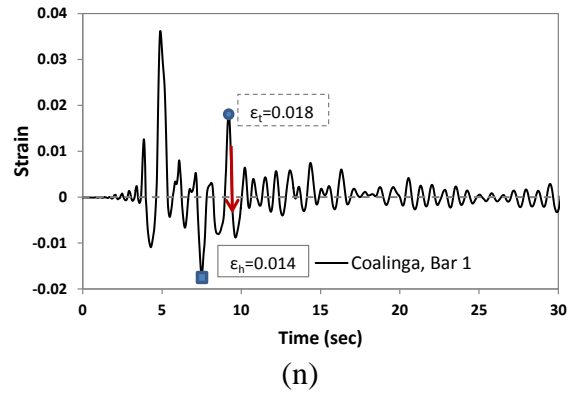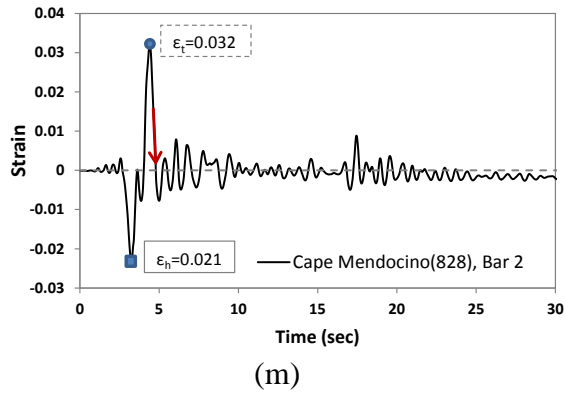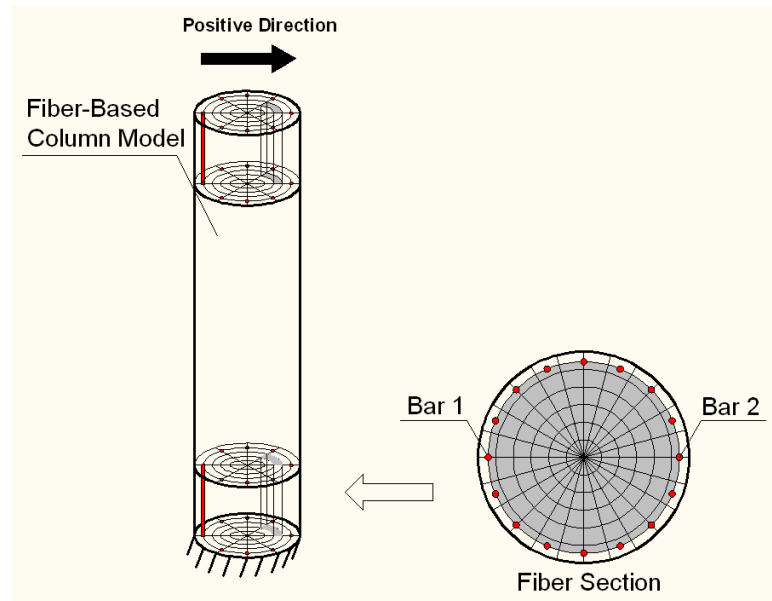
Figure 6.3. Locations of Bars

6.4.2 Key Findings from Load History Analysis Results

Although bar buckling is known as a compressive phenomenon, Moyer and Kowalsky (2003) described a tension based buckling mechanism which revealed severe bar instability upon reversal from a large tensile strain in RC members. In addition, the compressive cycle in a strain history, which does not buckle the longitudinal bar, may change the boundary condition of the bar by plastically elongating the hoops, as discussed in detail by Feng et al. (2013)[2]. Therefore, the required tensile strain to result in instability during further compressive loading may be reduced at a larger unsupported length caused by the plastic elongation of hoops.

A significant outcome of the initial analysis is the role of previous compressive cycles on bar buckling. It is well established that the level of transverse bar restraint impacts the onset of bar buckling. For example, tighter spiral pitch provides larger lateral restraint against

bar buckling. However, what is less obvious is the transient nature of the restraint provided by the transverse steel. What follows below is a key revision to the Moyer and Kowalsky model (2003) to account for the transient nature of transverse steel restraint, which also was noted by Goodnight et al. (2013).

Consider Figure 6.4 which shows the plastic hinge region (without cover concrete) in an RC column subjected to combined flexure and axial load. Under counterclockwise moment (see Figure 6.4(a)), the left side of the column in the bottom plastic hinge region is placed in compression. This causes the concrete in the compressive zone to expand, thus activating the transverse steel, as shown in Figure 6.5. If the counterclockwise moment is sufficiently severe, the transverse steel will yield and the boundary conditions for supporting the longitudinal bars change. Now, consider the clockwise moment (see Figure 6.4(b)). The longitudinal bars previously in compression are now subjected to tensile strain and cracks form on the tensile side of the member. Upon a second counterclockwise moment (Figure 6.4(c)), the longitudinal reinforcing bars on the left become the sole source of compression zone stability before crack closure. The occurrence of buckling under this cycle of loading is dictated by the ability of the bar to carry compression, which in turn is a function of the detailing and the restraint provided by the transverse steel. During the loading in Figure 6.4(a), the restraint provided by the transverse steel is affected not only by the level of detailing, but also the impact of previous compressive loading on the member.
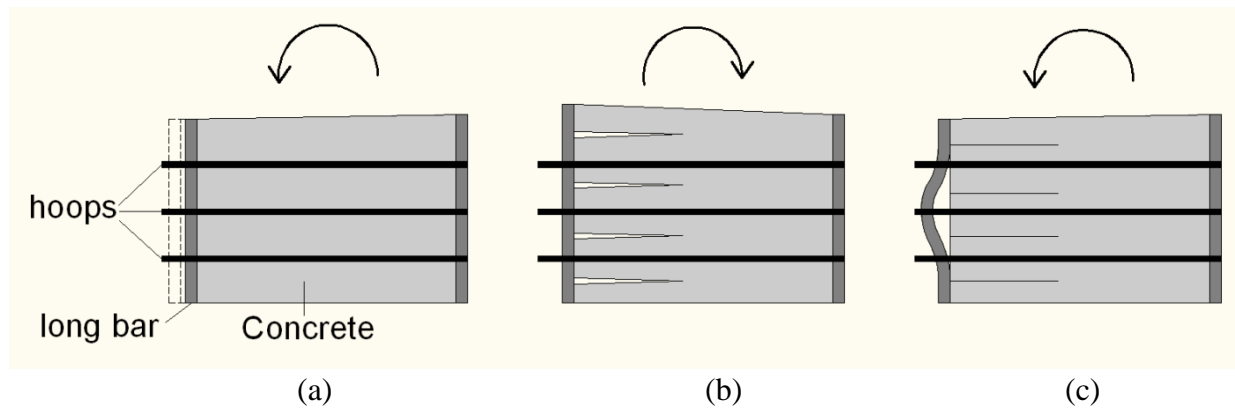
(a)   (b)   (c)
Figure 6.4. Plastic Hinge Region in Cyclic Loading
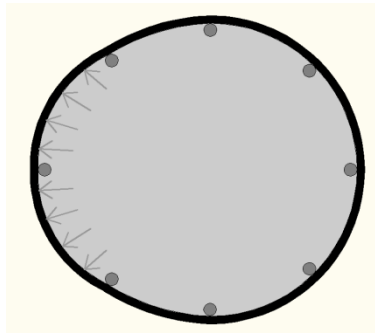
Figure 6.5. Sectional View under the Load in Figure4(a) (deformations are exaggerated)

In this series of analyses, twelve out of fourteen observed instances of bar buckling in the finite element analysis exhibited yielding of the transverse steel prior to bar buckling. The yielding of the transverse steel was caused by a single large compressive cycle prior to bar bucking. This is easily explained with reference to Figure 6.2 in which the arrows represent the loading cycle where reinforcing bar bucking was first observed in the analysis. Prior to the cycle that resulted in bar bucking, the peak tensile strain in the longitudinal bars, ε_t, is shown by the circular marker. Lastly, the magnitude of the transverse steel strain achieved in

the prior compression cycle is identified with the variable ε_h next to the square markers. As a consequence, it is observed that bar buckling occurs after reversal from the peak tensile strain following the yielding of the transverse steel in all cases. The importance of yielding in the transverse steel is further highlighted in Figure 6.2(a), (c), (g), (j), and (n) where the peak tensile strain demand occurs prior to yielding of the transverse steel, yet buckling was delayed to cycles later in the response (although still upon reversal from the peak tensile strain after yielding of the transverse steel).

Only the analysis depicted in Figure 6.2(e) and (h) resulted in reinforcing bar buckling without yielding of the transverse steel. In the case of Figure 6.2(e), there were extensive tensile cycles which resulted in the bar under axial compression upon reversal. When applying an axial load to the reinforcing bar, there will always be some degree of eccentricity due to imperfections in the bar. Analytically, it is of course possible to apply uniform compression to a longitudinal bar. However, in this finite element model, the boundary conditions on either side of the reinforcing bar are non-uniform. On one side, the concrete expands, bearing on the bar, and on the opposing side, the transverse steel provides restraint. This condition is the same as would be expected in a physical test. As a consequence, non-uniform stresses and strains will form along the bar cross section, which is shown in detail by Feng et al. (2013). The level of non-uniform stress increases upon each reversal from the large tensile strains. A similar argument can be made in the case of Figure 6.2(h), although only with 2 cycles of tensile loading, albeit a very high levels of tensile strain.

In summary, the initial analysis demonstrated that both compressive strain in the section (as it effects the degree of yielding in transverse steel and corresponding longitudinal boundary conditions), and tension strain (as it effects accumulation of non-uniform stress as well as the bar deformation that must be sustained upon reversal), are important variables impacted by load history. Given the apparent importance of compression loading and its impact on bar restraint, the remainder of this chapter will focus on a deeper exploration to quantify the effect of this variable, and how it may be considered in developing strain limits for reinforcing bar buckling for specific levels of detailing.

6.5 Parametric Study on Bar Buckling

As noted previously, the peak compressive strain in a section determines the degree of plastic elongation in transverse steel, and as a result the effective boundary conditions supporting a reinforcing bar, while the peak tensile strain represents the amount of deformation that must be sustained upon further reversals of loading in compression if a bar is to avoid buckling.

In order to study this phenomenon more closely, a series of 'single cycle' analysis were conducted. The analyses consisted of subjecting the finite element bar buckling model of Figure 6.1 to a prescribed compressive strain followed by a tensile strain, and then a second reversal in compression. For the given level of initial compressive strain demand, if the level of tensile strain did not initiate bucking, the analysis was re-run, with the tensile strain increased until bar bucking occurred upon reversal. Consider Figure 6.6 as an example, which shows this process for a given level of reinforcement detailing. In Figure 6.6(a), the model was subjected to a compressive strain of 1%. This was followed by loading in tension, and then a second reversal in compression. The level of tensile strain was increased until buckling occurred upon reversal in compression. In the case of Figure 6.6(a), a compression strain of 1% required a tensile strain of 3% to result in buckling upon reversal. The same iterative process was then employed for a larger initial compressive strain, as shown in Figure 6.6(b) where the model was subjected to a compressive strain of 2%. In this case, the required tensile strain to cause buckling upon reversal was only 2% as the increased level of compression resulted in an increase in spiral plastic strain and hence a reduction in the restraint provided to the longitudinal bar. Figure 6.6 shows a third example where the compressive strain was increased to 3%, which required an even smaller level of tensile strain to result in bar buckling upon reversal.
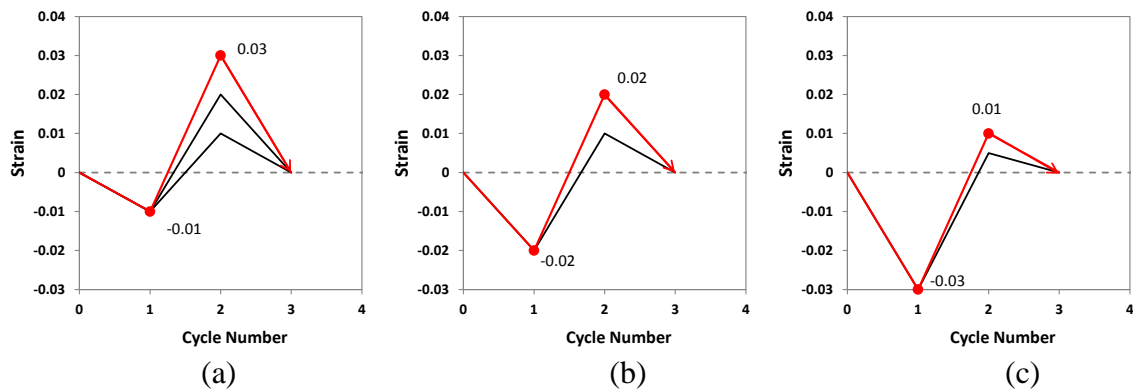
Figure 6.6. Reverse Cyclic Strain Histories

The analysis method described in Figure 6.6 was applied to sections with a variety of detailing as shown in Table 6.3. For the purpose of developing a design equation to define strain limits for reinforcing bar buckling, this chapter considers two key parameters: (1) The ratio of transverse steel spacing to the longitudinal bar diameter, and (2) The ratio of the hoop diameter to the longitudinal bar diameter. The first of these represents the original unsupported length which is one of the most critical factors in inelastic bar buckling. The second indicates the relative lateral restraint to resist bar buckling with respect to the bar diameter which determines the outward deformation demand on the restraint if bar eccentricity occurs. To vary the two ratios, the longitudinal bar diameter and hoop spacing were used as the variables. The spiral diameter was varied in the parametric study since altering the spiral diameter changes the interaction between hoops and the concrete block in the simplified finite element model from Feng et al. (2013)[2]. To capture the local confining effect accurately with a different spiral diameter, the thickness of the concrete block in the finite element model needs to be redefined based on the experimental results with the corresponding spiral diameters. As a consequence, only the bar diameter and spiral pitch were selected as the variables for consistency with the finite element model. Later in this chapter, comparisons to the existing column database which contains a large range of transverse bar diameters, will allow further study into the accuracy of the model.

For each detailing configuration, tensile and compressive strain limit curves were developed. Results of the analysis for the sections in Table 6.3 are shown in Figure 6.7. In each case, the thick black line with markers represents the relationship between imposed compressive strain and the required tensile strain to cause buckling upon reversal for the section under consideration. The thin grey line represents the strain in the transverse steel under corresponding compressive strain and the dashed line shows the yielding strain limit of transverse steel.

As expected, when the compressive strain demand in the section increases, the transverse steel strain increases, which results in reduced restraint against bar buckling and a corresponding reduction in the tensile strain limit in the longitudinal bar to initiate buckling upon reversal. The reduction of the tensile strain limit for bar buckling is more profound in sections 1 and 2, which correspond to Figure 6.7(a) and (b), when compared to section 3 (Figure 6.7(c)). Therefore, the compressive strain has more impact on the tensile limit state for bar buckling in sections that are heavily reinforced in the transverse direction. On the other hand, while the longitudinal bar diameter increases from Figure 6.7(a) to (d) and (e), the tensile strain limit becomes less sensitive to the impact of the compressive strain since the longitudinal bar itself is more stable.

Table 6.3. Sectional Variables in Parametric Study

Section Number	Spiral Pitch cm(in)	Spiral Diameter cm(in)	Bar Diameter cm(in)	Pitch/Bar Diameter s/d_{bl}	Spiral/Bar Diameter d_h/d_{bl}	Volumetric Ratio $\rho_{v\,(\%)}$
1	5 (2)	0.95 (0.375)	1.9 (0.75)	2.6	0.5	0.92
2	3.8 (1.5)	0.95 (0.375)	1.9 (0.75)	2	0.5	1.22
3	7.6 (3)	0.95 (0.375)	1.9 (0.75)	4	0.5	0.61
4	5 (2)	0.95 (0.375)	2.2 (0.875)	2.3	0.43	0.92
5	5 (2)	0.95 (0.375)	2.5 (1)	2	0.38	0.92

(a) Section 1

(b) Section 2

(b) Section 3

(d) Section 4

(e) Section 5
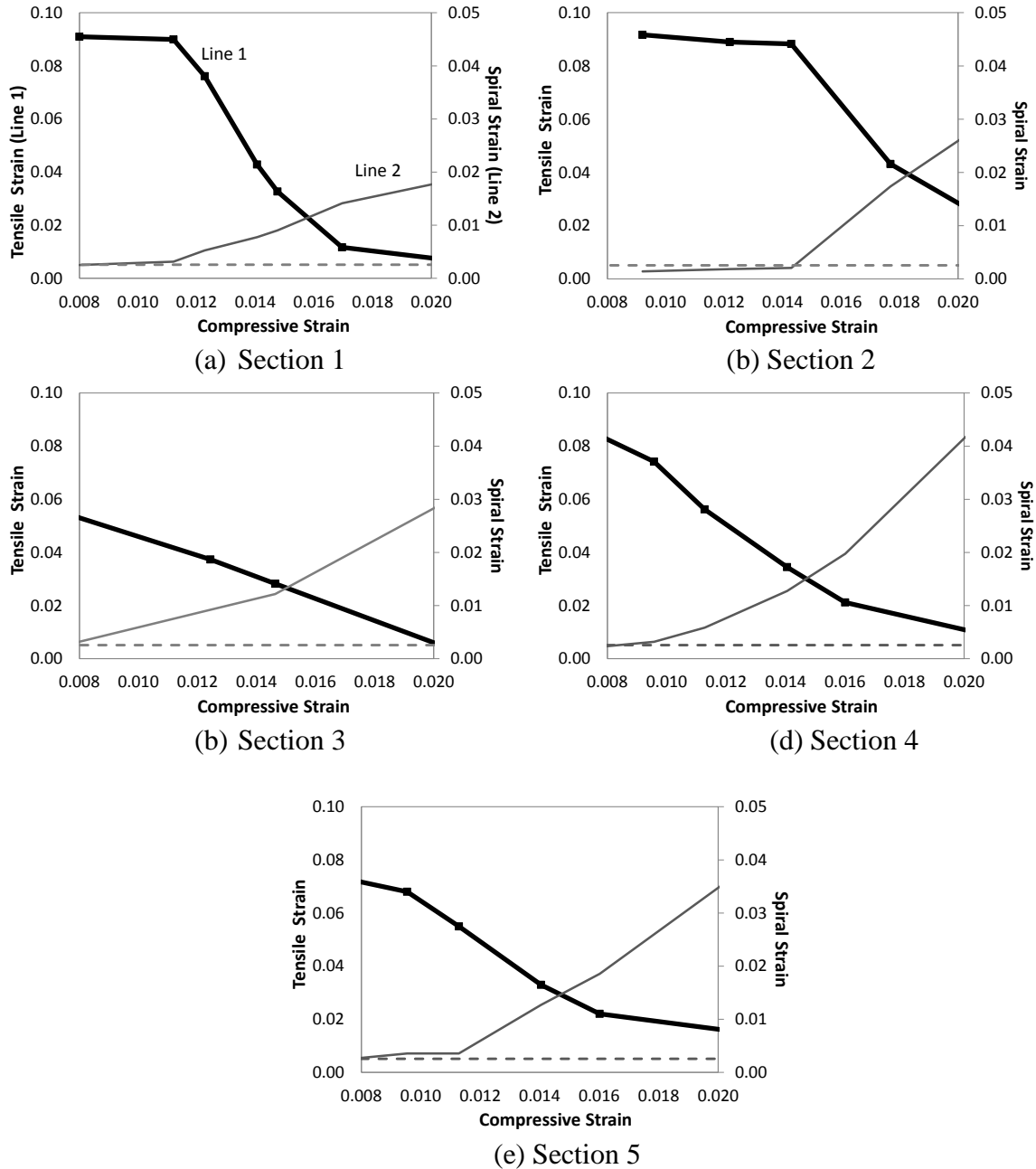
Figure 6.7. Strain Limit Relationship for Bar Buckling

6.6 Proposed Equations for Bar Buckling Strain Limit State

The data from Figure 6.7 can be used to develop design equations that relate compressive and tensile strains to key geometric variables. Expressions were developed using multi-linear regression, as shown in Eq. 6.1 to 6.3. The three variables considered in the equations are the ratio of spiral pitch to the longitudinal bar diameter and the ratio of the hoop diameter to longitudinal bar diameter. These equations can be used for both SI units and US customary units, and both tensile and compressive strains are positive in the equations. Due to the limited reinforcement combination in the parametric study, these equations are suggested to be used in modern detailed RC sections where s/d_{bl} is less than 5 and the volumetric ratio of transverse steel is greater than 0.5%. The comparisons between the predictions from Eq. 6.1 to 6.3 and the analysis results are shown in Figure 6.8 where the total R square value from the regression is 0.958.

$$\varepsilon_t = \frac{-15\left(\varepsilon_c - \frac{0.0205}{\sqrt[3]{\frac{s}{d_{bl}}-1}}\right)}{\left(\frac{d_{bl}}{d_h}-1\right)^2} \tag{6.1}$$

$$\varepsilon_t \geq -1.7\frac{s}{d_{bl}}\sqrt{\frac{d_h}{d_{bl}}}\varepsilon_c + 0.045\sqrt{\frac{s}{d_{bl}}} \tag{6.2}$$

$$\varepsilon_t \leq 0.09 \text{ , if } \frac{s}{d_{bl}} < 3 \tag{6.3a}$$

$$\varepsilon_t \leq 0.06 \text{ , if } \frac{s}{d_{bl}} > 4 \tag{6.3b}$$

$$\varepsilon_t \leq 0.09 - 0.03(\frac{s}{d_{bl}}-3) \text{ , if } 3 < \frac{s}{d_{bl}} < 4 \tag{6.3c}$$

(a)

(b)

(c)

(d)

(e)
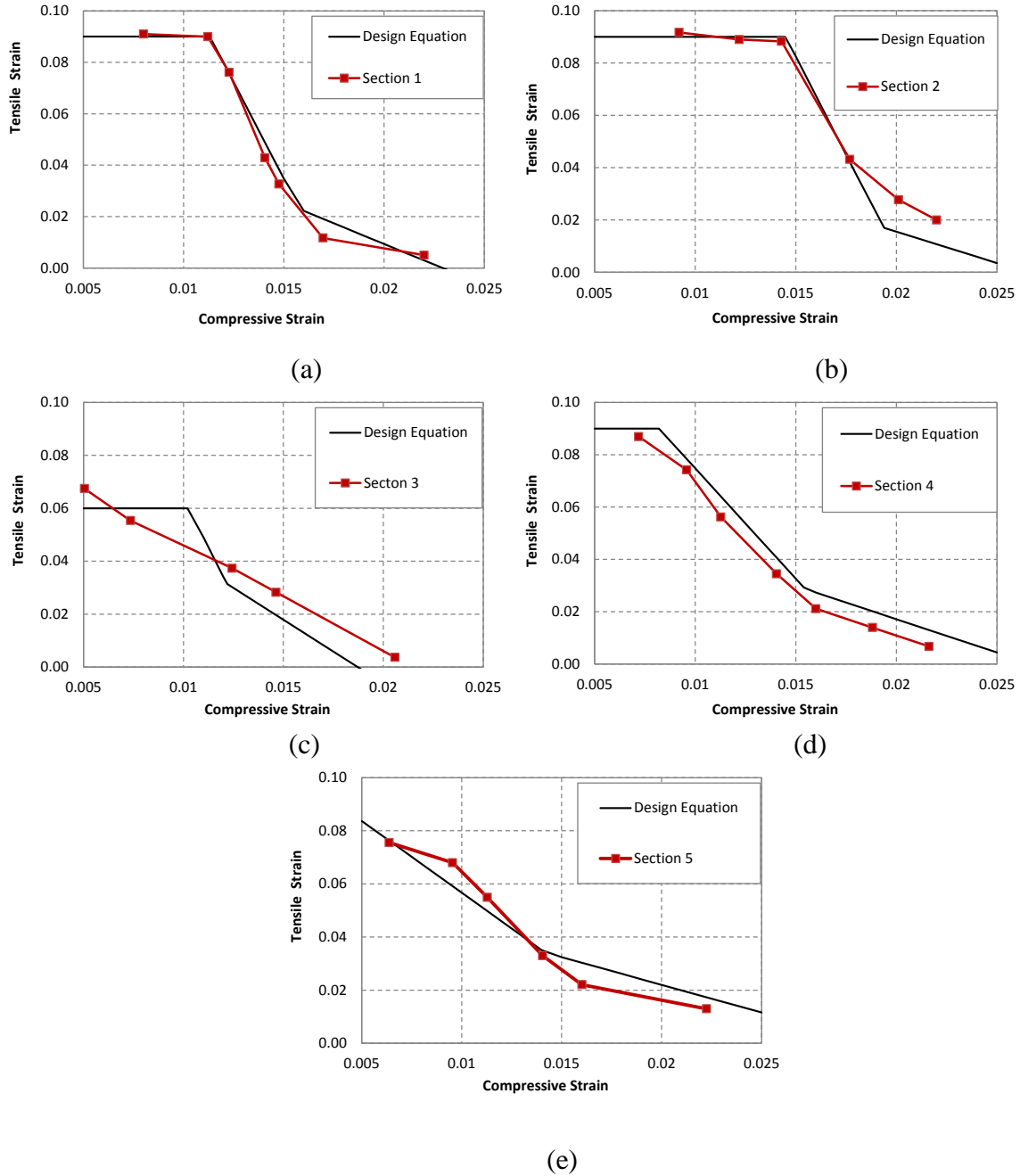
Figure 6.8. Comparison of Proposed Equation and Analytical Result

6.6.1   Comparison of Proposed Model to Tests Conducted at NCSU

To verify the accuracy of the proposed model, the expressions were utilized to predict the buckling strains for twelve experimental tests conducted at North Carolina State University, where specimens were subjected to three-cycle-set and real earthquake load histories. Details of these tests can be found in Goodnight et al. (2013), where the important feature is that an advanced instrumentation system was used which allowed measurement of strains in longitudinal steel well into the nonlinear range. The photo in Figure 6.1 shows LED markers in a sample test that were placed directly on the longitudinal steel and monitored with a non-contact instrumentation system. As shown in the strain history from Figure 6.9, the peak tensile and compressive strain combination prior to buckling (circles) were extracted from the test data to represent the buckling strain limit while the strain combinations at lower deformation levels (squares) were extracted as the strain magnitudes which failed to generate buckling. Both of these combinations are plotted against the proposed model, as shown in Figure 6.10. If the prediction is correct, any combination of strains outside the curve should buckle the bar and a couple of strains inside the curve should not lead to bar buckling in Figure 6.10. In most cases, it appears that the proposed model provides a good indication of the boundary between the buckled and non-buckled strain limits. The impact of section detailing on the buckling strain limit is also captured well by the proposed equations from Figure 6.10(a) to (e).
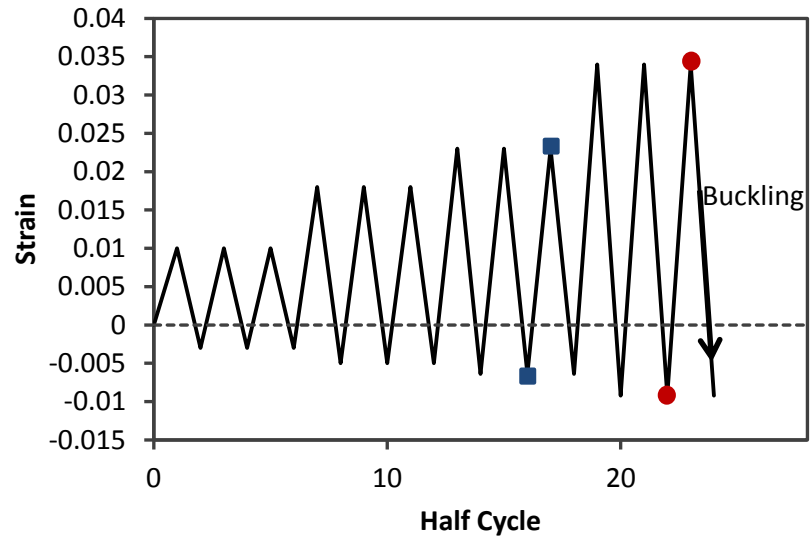
Figure 6.9. Strain Points for Bar Buckling in Test Data

Figure 6.10. Comparison of Proposed Design Equation and Test Data
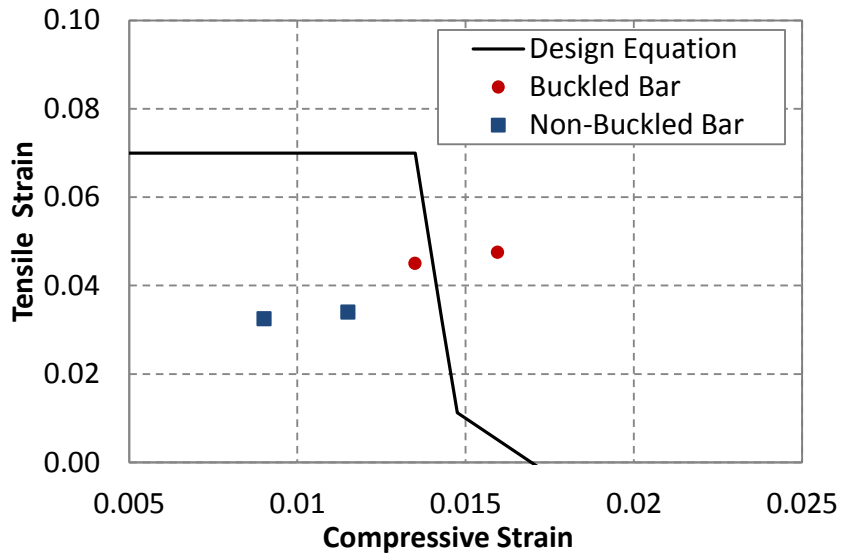
(a)   #6 bar with #4 spiral at 7cm
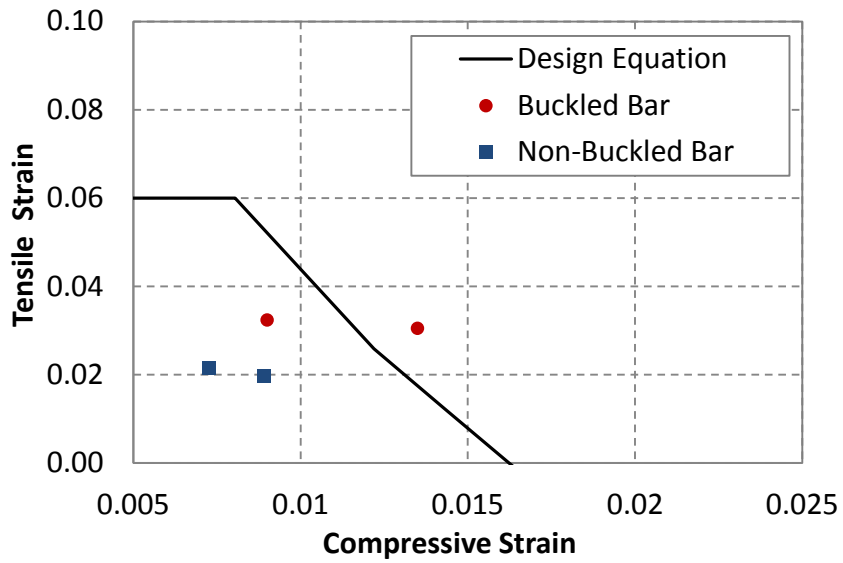
(b)   #6 bar with #3 spiral at 10cm
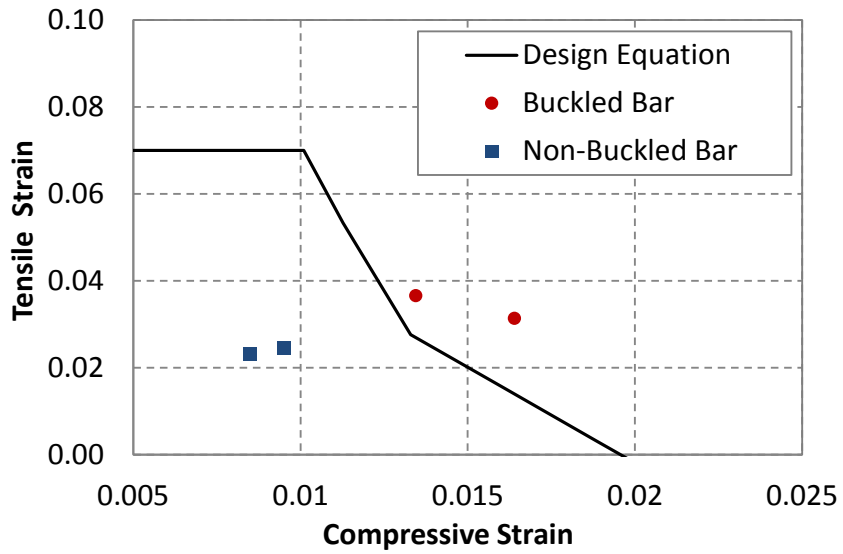
(c)   #6 bar with #3 spiral at 7cm
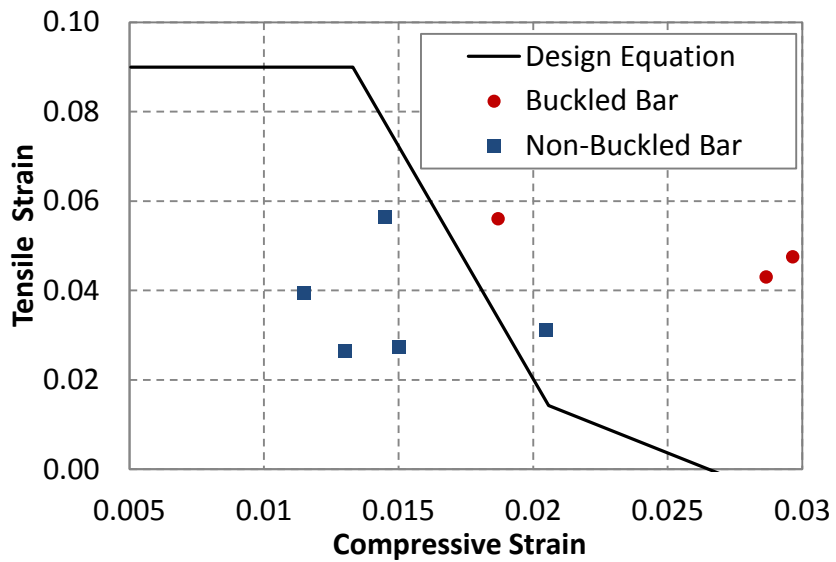
(d)   #6 bar with #3 spiral at 4cm
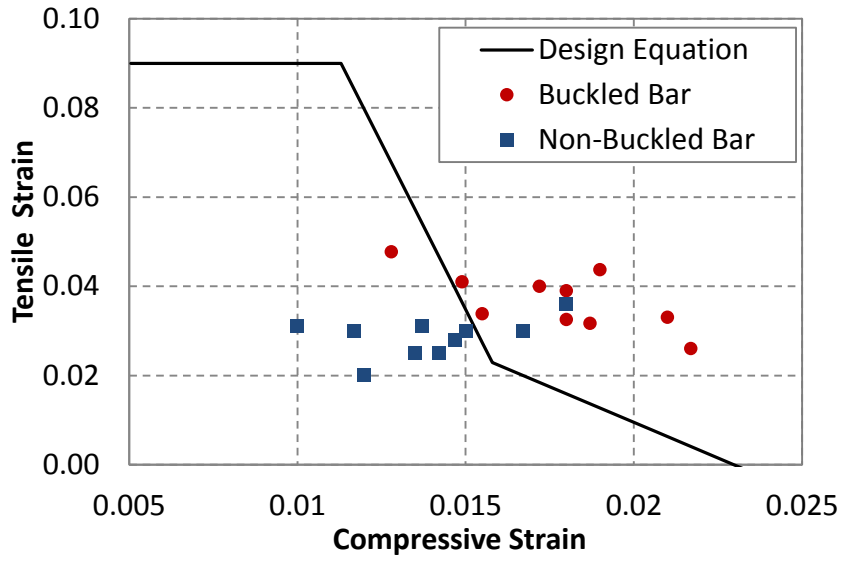
(e)   #6 bar with #3 spiral at 5cm

6.7 Application of the Design Equation

The primary function of the proposed design equation is to identify the strain limit state for bar buckling with a given sectional detailing. For design, it would be more helpful to express the equation in terms of displacements. Therefore, the strain limit curves need to be converted to a displacement relationship given the structural member length and the axial load. Sectional analysis and the plastic hinge method can be used for this purpose, or alternatively a fiber-based model could be constructed for each case.

Outlined below is a step by step approach that is also accompanied by a numerical example of a bridge column. The details of the column example are as follows: Column dimensions: 2.4 m in height, 0.6 m in diameter; Material properties: f'$_c$ = 41 MPa, f$_y$ = 468 MPa; Axial load in compression of 756 kN; Internal reinforcement of 16 #6 bars and #3 spiral at 7 cm.

1.   **Generate Strain Limit Curve with Eq. 6.1-6.3:**

$$\varepsilon_t = \frac{-15\left(\varepsilon_c - \dfrac{0.0205}{\sqrt[3]{\dfrac{s}{d_{bl}} - 1}}\right)}{\left(\dfrac{d_{bl}}{d_h} - 1\right)^2} = -15(\varepsilon_c - 0.0148)$$

$$\varepsilon_t \geq -1.7\frac{s}{d_{bl}}\sqrt{\frac{d_h}{d_{bl}}}\varepsilon_c + 0.045\sqrt{\frac{s}{d_{bl}}} = -4.41\varepsilon_c + 0.0862$$

$$\varepsilon_t \leq 0.09 - 0.03(\frac{s}{d_{bl}} - 3) = 0.07 \text{ , since } 3 < \frac{s}{d_{bl}} = 3.67 < 4$$

The corresponding strain limit curve is shown in Figure 6.11(a)

2. **Find the end points of each branch as shown in Figure 6.11(a), and convert them to corresponding displacement combinations which will be used to establish the displacement limit curve.**

   The point of (0.01, 0.07) from Figure 6.11(a) is selected as an example to carry through the process.

3. **Apply sectional analysis to obtain the curvature at the both strain values of the point:**

   M-ϕ analysis results in a curvature of 0.081 1/m for a bar compressive strain of 0.01.

   M-ϕ analysis results in a curvature of 0.161 1/m for a bar tensile strain of 0.07.

4. **Estimate the equivalent yield curvature with the equation from Priestley et al. (2007):**

   $\varphi_y = 2.25\varepsilon_y/D = 2.25*0.00234/0.6 = 0.0088$ 1/m

5. **Calculate the plastic hinge length with the equations from Priestley et al. (2007):**

   $L_{SP} = 0.022f_{ye}d_{bl} = 0.022*468*1.9 = 19.6$ cm

   $k = 0.2(f_u/f_y - 1) = 0.2*(650/468-1) = 0.078$

   $L_p = kL_C + L_{SP} = 0.078*240 + 19.6 = 38.3$ cm $< 2L_{SP}$

   $L_p = 2L_{SP} = 2*19.6 = 39.2$ cm

6. **Calculate the equivalent yield displacement:**

   $\Delta_y = \varphi_y(H+L_{SP})^2/3 = 0.000088*(240+19.6)^2/3 = 1.98$ cm

7. **Calculate the total displacement :**

   $\Delta_c = \Delta_y + \Delta_p = \Delta_y + (\varphi_c - \varphi_y)L_PH = 1.98 + (0.00081-0.000088)*39.2*240 = 8.8$ cm

$\Delta_t = \Delta_y + \Delta_p = \Delta_y + (\varphi_t - \varphi_y)L_P H = 1.98 + (0.00161 - 0.000088)*39.2*240 = 16.3$ cm

8. **Select another point from Figure 6.11(a) and go through step 2 to 7 again to obtain the displacement combination:**

   The strain combination of (0.01, 0.07) leads to the displacement combination of (8.8, 16.4). Similarly, the strain combinations of (0, 0.07), (0.0133, 0.0276), and (0.0196, 0) lead to the displacement combinations of (0, 16.3), (11.2, 7.1), and (15.4, 0) cm, respectively.

9. **Utilize the four displacement points to establish the displacement limit curve, as shown in Figure 6.11(b).**

(a)   (b)
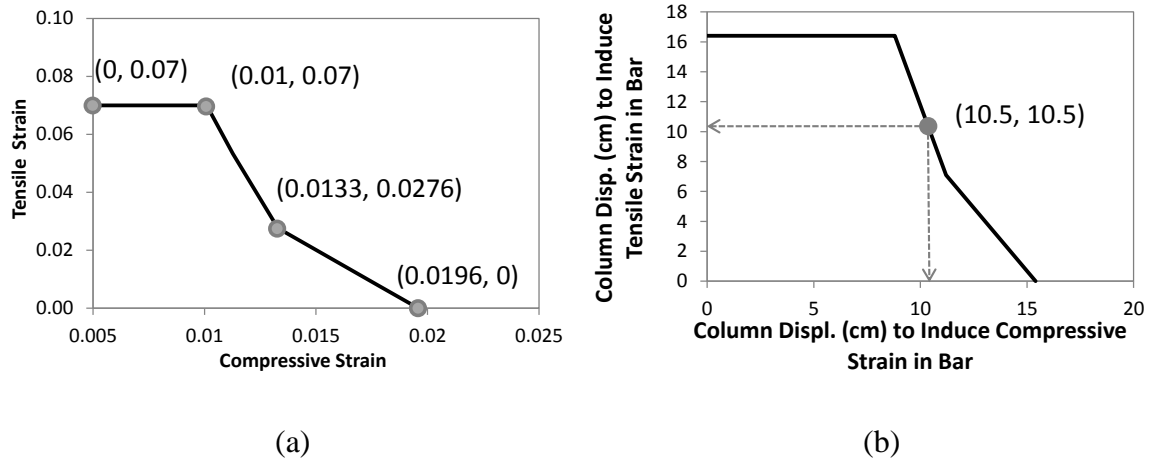
Figure 6.11. Displacement Limit Relationship for Bar Buckling

Figure 6.11 presents the outcome of this calculation for the example column described above. The manner in which this graph is used would be to identify the column displacement that induces compression in a given bar, and then read up to find the required column displacement that would cause the required amount of tension to cause bar buckling upon reversal. For example, a lateral column displacement of 5 cm would require 16cm in the opposing direction to initiate bucking. From a post-earthquake assessment perspective where input motions are known, this could of course be rather useful; however, for design, where imposed member deformation are unknown in advance of an earthquake, it is suggested the displacement to be assumed at the same level in each direction. As a consequence, to obtain the column displacement limit for the onset of bar buckling, the one point on the curve where the column displacements are the same is identified. In the case of the example in Figure 6.11, that occurs at a displacement of 10.5 cm.

As an alternative, the strain limits themselves can be obtained with a simpler process. First, a moment curvature analysis is conducted to obtain the relationship between the tensile strain and compressive strain at given levels of curvature level which indicates a single displacement level. Each combination of compressive and tensile strain is then plotted along with the strain limit curve from Eq. 6.1-6.3, an example of which is shown in Figure 6.12. The intersecting point (0.012, 0.04) represents the strain limit for the onset of bar buckling which combines a compressive strain of 0.012 and a tensile strain of 0.04.
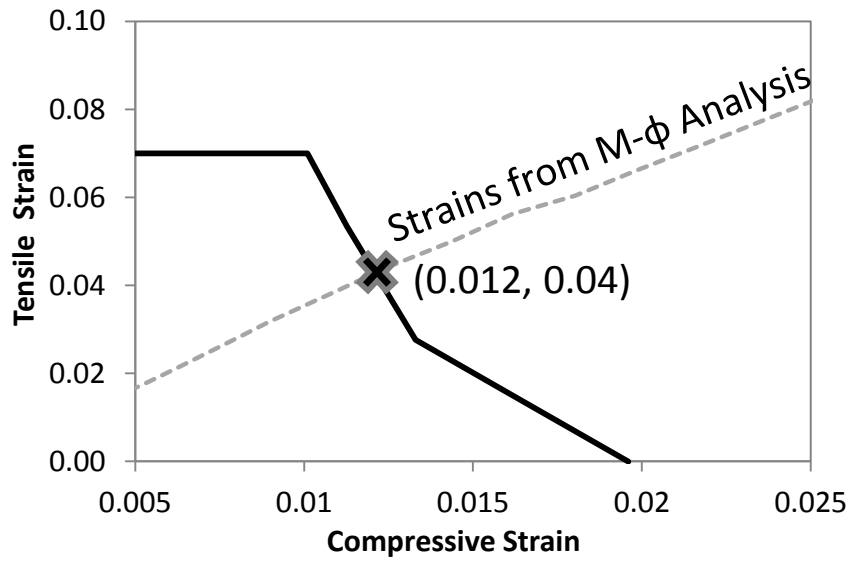
Figure 6.12. Method to Define Strain Limit

6.8 Comparison to Structural Performance Database

The Structural Performance Database (http://www.ce.washington.edu/~peera1/) contains experimental results from cyclic column tests where bar buckling was observed and the corresponding displacement levels were recorded. The range of parameters for column detailing are as follow: aspect ratios from 2 to 6.6; column diameters from 0.25 to 1.5 m; longitudinal bar diameters from 7 to 43 mm; ratios of hoop diameter to longitudinal bar diameter from 0.28 to 0.71; ratio of hoop spacing to longitudinal bar diameters from 1.3 to 8.4; axial load ratios from 4% to 70%.

The proposed equations were used to predict the buckling strain limit curve in which the predicted displacement limit for bar buckling can be obtained with the method previously discussed. As shown in Figure 6.13, the predicted displacement level for the 49 tests from the database serves as a very good limit beyond which bar buckling will be observed in the tests. The horizontal axis in Figure 6.13 is the number of each tested column and each data point represents a column test. Around 70% of the data points ($\Delta_{exp}/\Delta_{pre}$) in Figure 6.13 are within the range from 0.9 to 1.5.

There are a few reasons for the scatter in Figure 6.13. (1) The method to determine displacement at which bar buckling occurs is affected by the accuracy of the plastic hinge method which is used to convert the strain to the displacement. Goodnight et al. (2013) found that the plastic hinge method overestimated the tensile strain in longitudinal bars from experimental tests. As a consequence, given a strain limit from the proposed equation, the predicted displacement level by the plastic hinge method will be underestimated as shown by most points in Figure 6.13. This is why the comparisons in Figure 6.10 with tests conducted at NCSU were presented first. Strain information was directly available from the tests conducted at NCSU, and the accuracy of the model can as a result be readily established. However, direct strain information is generally not available in the literature due to difficulty in measurement, and as a consequence can only be inferred by analysis. A more reliable method, such as fiber-based modeling, to convert local strain to column displacements may

allow the proposed method to provide a better deformation limit prediction for bar buckling. Analyses have shown that the displacements at a given level of strain using fiber-based analysis are consistently larger than those obtained from the plastic hinge method (Goodnight and Feng (2012)). Nonetheless, for design, it is unlikely that a fiber-based model will be employed and until more accurate plastic hinge length expressions are developed, the approach described above may be used to achieve conservative results for identifying the displacement limit state to initiate bar buckling. (2) The proposed method has a defined numerical limit for longitudinal bar deformation to identify the onset of bar buckling; however, the manner in which bar bucking is reported in the literature may be open to some degree of interpretation by individual researchers and is usually not quantitatively measured but qualitatively observed. The experimental tests conducted at NCSU (see Figure 6.11) used a quantitative definition which can be then be assessed via the instrumentation system employed. The same cannot be done for the experiments in the structural performance database. (3) Most of the tests included in the Structural Performance Database were ramp-up cyclic tests where the incremental displacement from cycle to cycle may not precisely define the deformation limit state for the onset of bar buckling. For example, for a 3-cycle-set loading history, if the deformation limit state for buckling is at ductility 5, the onset of bar buckling can only be observed if the displacement ductility level of 5 is directly imposed on the test specimen. Often, loading may proceed directly from ductility 4 to ductility 6. Bar buckling may have been observed at ductility 5 had the column been subjected to ductility 5 level deformation prior to proceeding to ductility 6. As a result, the recorded displacement at ductility 6 would overestimate the deformation limit state for onset of bar buckling. The same argument can be made for loading from ductility 6 to 8, and beyond.
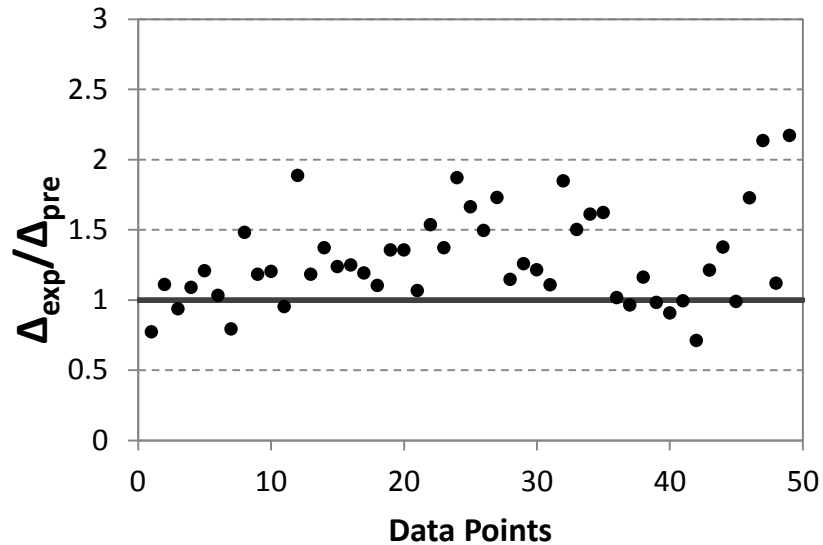
Figure 6.13. Prediction against Test Data

6.9   Chapter Conclusions

This chapter investigates the characteristics of real earthquake load histories and the bar strain history which impacts inelastic bar buckling in circular RC columns. A significant finding in this investigation is that the longitudinal bar buckling often occurs upon reversal from a tensile strain, after transverse steel yielded in a previous compressive strain cycle. Plastic elongation of transverse steel results in an increase in the unsupported length of the longitudinal reinforcing bar, which is a critical factor for inelastic bar buckling.

Given the fact that future earthquake load histories cannot be known in advance for design, a single cycle reverse cyclic loading was utilized to include the most critical factors of load history on bar buckling, which are the peak compressive and tensile strains. Strain limit curves for bar buckling were established for various reinforcement detailing and design equations were developed for the generation of these curves. The variables in the equations

are reinforcing bar diameter, transverse reinforcement diameter, and transverse steel spacing. The proposed equations accurately predict the demarcation point of bar buckling for tests conducted at NCSU using an advanced non-contact instrumentation system. In addition, a simple method to define the displacement limit state for bar buckling is introduced and compared against an existing column database. The comparison shows that the predicted displacement serves as a good limit to define the initiation of bar buckling.

Chapter 7: Conclusions

7.1 General Discussion

Traditional earthquake engineering quantifies the earthquake intensity based on its energy release or the force it imposes on the structure. However, the characteristics of load history or load path may also impact the damage level of a structure. Also, it is important to identify the damage or performance level as limit states in PBEE. For RC structures, longitudinal bar buckling is generally regarded as the condition beyond which the structure requires replacement. For instance, the current practice of the California and Alaska Departments of Transportation is to replace structural members that exhibit a high degree of reinforcing bar buckling. As a result, this research work specifically focuses on the investigation of the seismic load history effect on the onset of bar buckling in RC bridge columns.

Previous research (Moyer and Kowalsky (2003)) has revealed the influence of tensile strain on bar buckling, upon reversal of tensile loading. The strain on individual bars determines the onset of reinforcing bar buckling when the structural displacement is often used as the demand in design. Therefore, it is necessary to study the impact of load history on the relationship between local strain and displacement. The plastic hinge method and sectional analysis is the normal approach utilized to obtain local strain values given a deformation on a structural member. However, the plastic hinge method is empirical and does not include the effect of reverse cyclic loading on structural member behavior. Fiber-based finite elements are implemented in this research in order to relate the strain to displacement. A large amount of work was focused on the theory of fiber-based elements, which eventually allowed the author to modify the model and increase its accuracy. The force-based element was adapted to simulate the reinforced concrete column because of its accuracy in establishing the relationship between the local and global deformations. Two fiber-based models were developed one of which is simple and accurately predicts strain

magnitude while the other is able to provide the strain distribution with a post-processing method. The model with the 'Beam with Hinges' element is selected, because of its accuracy, for a parametric study on the relationship between strain and the displacement. Different structural configurations and sectional detailing are also considered in the study.

The load history effect on the strain limit itself for bar buckling was investigated on a finite element bar buckling model. The model was established with eight node brick elements and material models discussed in previous chapters. Two load histories from experimental tests were converted to strain histories and applied to the finite element bar buckling model to verify its accuracy. A large number of strain histories from nonlinear time history analyses were applied to the bar buckling model to study the effect of strain history on the onset of bar buckling. Given the fact that the engineer is not able to design a structure with the knowledge of a future earthquake load history, it was decided to utilize a reverse cyclic loading to include the most critical load history effect. A parametric study was then conducted for the purpose of developing a design equation to quantify the strain limit for bar buckling. The load history is not a variable in this parametric study since it was assumed that a load history has little additional impact other than its peak tensile and compressive strain. The design equation was developed to be simple and applicable for all systems of units. Given a sectional detailing, engineers can utilize the equation to calculate the strain limit for buckling or to assess the capacity of an existing structure.

7.2 Load History Effect on Relationship between Strain and Displacement

As a direct indicator of local damage, such as bar buckling and concrete crushing, strain response in a RC section results from global deformation demand. The relationship between the displacement and strain needs to be well-established considering the load history effect. Specifically for bar buckling, Moyer and Kowalsky (2003) have illustrated the growth strain from cyclic loading. The growth strain accumulates in loading cycles which may lead to a larger strain at the maximum displacement of a structure compared to the one from monotonic loading. Therefore, a parametric study with the fiber-based model was conducted for the purpose of quantifying the load history effect on the relationship between strain and displacement.

In general, the parametric study showed little load history effect on the relationship between the strain and displacement for all the column configurations. In the fiber-based model, the curvature distribution along the element is integrated to obtain nodal displacement. The growth strain proposed by Moyer and Kowalsky (2003) is a factor which may provide a larger tensile strain value at a given curvature level. For example, given a section diameter of 2 ft, if the strain on the tensile and compressive extreme fiber bars are 0.04 and -0.01, the curvature is around (0.04+0.01)/2=0.05 1/ft. In another case, the tensile growth strain could lead to the strains of 0.045 and -0.005 which also results in a curvature of (0.045+0.005)/2=0.05 1/ft. However, the parametric study showed minimal load history effect on the relationship between strain and displacement since the accumulation of growth strain is not seen in the fiber-based section. As a result, it is suggested to neglect load history effect on the relationship between strain and the displacement in design.

7.3 Load History Effect on the Strain Limit for Bar Buckling

The load history or strain history has significant impact on the strain limit for longitudinal bar buckling. The most significant findings are: (1) the bar is prone to buckling upon reversal from a tensile strain; (1) the magnitude of the tensile strain determines the likelihood of bar buckling; (3) a compressive strain can significantly reduce the required tensile strain to cause buckling. The critical factors in bar buckling, including magnitude of bar stress, tangent modulus, unsupported length, and imperfection, are strongly related to the strain history. Therefore, it is believed that the strain history on a bar determines the onset of bar buckling. However, the large number of analyses with the finite element bar buckling model showed that the most important characteristic of an earthquake load history is its resultant maximum compressive and tensile strain in the bar, which determines the degree of plastic spiral elongation prior to bar buckling and instability upon reversal of loading respectively. In addition, the engineer will not be able to predict the future load history or strain history in design. Therefore, the reverse cyclic strain history was selected in the parametric study to concentrate the most important characteristics in a load or strain history. A series of strain limit curves for bar buckling were established considering a variety of sectional detailing. A design equation was then proposed to quantify the strain limit for bar buckling given a RC section. The proposed equation includes the effect of strain history and reinforcement detailing on bar buckling. Engineers can also use the proposed equation to assess the capacity of a given set of sectional detailing in terms of the buckling strain limit, which can be converted to displacement capacity with the plastic hinge method or any other equivalent method. Since the strain limits predicted by the equation are in terms of a relationship between the tensile and compressive strain, a design approach is recommended to select the unique combination of tensile and compressive strain which gives the same displacement magnitude on both direction. The displacement value serves as the deformation limit state for bar buckling which considers the load history effect and the sectional detailing.

REFERENCES

Abaqus Analysis User's Manual 6.11 (2010)

Alejano, L., Alonso, E. (2005). "Considerations of the Dilatancy Angle in Rocks and Rock Masses." International Journal of Rock Mechanics and Mining Sciences, Vol. 42, No.4, 481-507

Alemdar, B. N. and White, D. W. (2005). "Displacement, Flexibility, and Mixed Beam-Column Finite Element Formulations for Distributed Plasticity Analysis". Journal of Structural Engineering. Vol. 131: No. 12, 1811-1819.

Bae, S., Mieses, A. M., and Bayrak, O. (2005). "Inelastic Buckling of Reinforcing Bars." Journal of Structural Engineering, Vol. 131, No. 2, 314-321

Bazant, Z. P. and Planas, J. (1998). "Fracture and Size Effect in Concrete and other Quasibrittle Materials", CRC, Boca Raton, Fla.

Berry, M. P., and Eberhard, M. O. (2005). "Practical Performance Model for Bar Buckling". J. Struct. Eng., 05(7), 1060-1070.

Calladine, C. R. (1973). "Inelastic Buckling of Columns: The Effect of Imperfections." Int. J. mech. Sci. 1973. Vol. 15, 593-604

de Borst, R., Feenstra, P. H., Panmin, J., and Sluys, L. J. (1994). "Some Current Issues in Computational Mechanics of Concrete Structures". Computer Modelling of Concrete Structures, Proc., EURO-C, H. Mang, N. Bicanic, and R. de Borst, eds., Swansea, U.K.

Dhakal, R., and Maekawa, K. (2002). "Reinforcement Stability and Fracture of Cover Concrete in Reinforced Concrete Members." J. Struct. Eng., 128(10), 1253-1262.

Dodd, L. and Restrepo-Posada, J. (1995). "Model for Predicting Cyclic Behavior of Reinforcing Steel" J. Struct. Eng., 121(3), 433-445.

El-Bahy, A, Kunnath, S.K., Stone, W.C., Taylor, A.W. (1999a). "Cumulative Seismic Damage of Circular Bridge Columns: Benchmark and Low-Cycle Fatigue Tests", ACI Structural Journal, Vol. 96, #4, pp. 633-641.

El-Bahy, A, Kunnath, S.K., Stone, W.C., Taylor, A.W. (1999b). "Cumulative Seismic Damage of Circular Bridge Columns: Variable Amplitude Tests", ACI Structural Journal, Vol. 96, #5, pp. 711-719.

Engesser, F. (1889). "Ueber Knickfragen" Schweizerische Bauzeitung, Vol. XXVI, No. 4, p. 24

Erasmus, L. A. (1981). "Cold Straightening of Partially Embedded Reinforcing Bars-a Different View." Concrete Int., 3(6), 47-52.

Euler, L. (1759). "Sur le forces des colonnes." Memoires de l'Academie Royale des Sciences et Belles Lettres, 13, Berlin, (in French).

Feng, Y., Kowalsky, M. J., and Nau, J. M. (2012). "Fiber-Based Modeling for Investigating the Effect of Lload History on the Behavior of RC Bridge Columns". 15th World Conference on Earthquake Engineering.

Feng, Y., Kowalsky, M. J., and Nau, J. M. (2013)[1]. Fiber-Based Modeling of Circular Reinforced Concrete Bridge Columns, Journal of Earthquake Engineering, Proceeding Paper

Feng, Y., Kowalsky, M. J., and Nau, J. M. (2013)[2]. Finite Element Method to Predict Reinforcing Bar Buckling in RC Structures. Journal of Structural Engineering, Proceeding Paper

Filippou, F. C., Popov, E. P. and Bertero, V. V. (1983). "Effects of Bond Deterioration on Hysteretic Behavior of Reinforced Concrete Joints". Report EERC 83-19, Earthquake Engineering Research Center, University of California, Berkeley.

Goodnight, J. C., Kowalsky, M. J., Nau, J. M. (2012). "Experimental Observations on the Effect of Load History on Performance Limit States of Circular Bridge Columns". 15th World Conference on Earthquake Engineering.

Goodnight, J. C., Kowalsky, M. J., and Nau, J. M., (2013). "The Effect of Load History on Performance Limit States of Circular Bridge Columns." J. Bridge Eng., 10. 1061, Apr. 1

Hildebrand, F. B. (1974). *Introduction to Numerical Analysis*, McGrw-Hill, New York.

Ingham, J.M., Liddell, D., and Davidson, B.J. (2001). "Influence of Loading History on the Response of a Reinforced Concrete Beam", Bulletin of the New Zealand Society for Earthquake Engineering, Vol. 34 #2, June, pp.107-124.

Ingham, J.M., Liddell, D., and Davidson, B.J. (2002). "An Assessment of Parameters Describing the Response of a Reinforced Concrete Beam", Bulletin of the New Zealand Society for Earthquake Engineering, Vol. 35 #1, June, pp.1-16.

Jasinski, F. (1895) "Noch ein Wort zu den Knickfragen." Schweizerische Bauzeitung, Vol. XXV, No. 25, p. 172

Karman (1910). "Untersuchungen uber Knickfestigkeit." Forschungsarbeiten, Nr. 81

Kunnath, S. K., and El-Bahy, A. (1996). "Cumulative Seismic Damage of Reinforced Concrete Bridge Piers", National Institute of Standards and Technology Technical Report 6075

Kunnath, S., El-Bahy, A., Taylor, A., and Stone, W. (1997). "Cumulative Seismic Damage of Reinforced Concrete Bridge Piers." Technical Rep. NCEER-97-0006, National Center of Earthquake Engineering Research, Buffalo, NY.

Lee, C., and Filippou, C., (2009), "Efficient Beam-Column Element with Variable Inelastic End Zones", Journal of Structural Engineering, Vol. 135, No. 11, 1310-1319

Lee, J., and Fenvers G. L., (1998). "Plastic-Damage Model for Cyclic Loading of Concrete Structures." J. of Eng. Mech., Vol, 124. No.8, pp. 892-900

Lehman, D. E., Gookin, S. E., Nacamuli, A. M., and Moehle, J. P. (2001). "Repair of Earthquake-Damaged Bridge Columns". ACI Struct. J., 98(2), 233-242

Lemaitre, J., and J.-L. Chaboche (1990). *Mechanics of Solid Materials*, Cambridge University Press.

Lubliner, J., Oliver, J., Oller, S., and Onate, E. (1989). "A Plastic-Damage Model for Concrete". International Journal of Solids and Structures, Vol. 25, no.3, pp, 229-326.

Malm, R. (2006). "Shear Cracks in Concrete Structures Subjected to In-Plaine Stresses." TRITA-BKN. Bulletin 88

Mander, J. B., Priestley, M. J. N. and Park, R. (1988). "Theoretical Stress-Strain Model for Confined Concrete". Journal of Structural Engineering. Vol. 114: No. 8, 1804-1826.

Massone, L. M. and Moroder, D. (2009). "Buckling Modeling of Reinforcing Bars with Imperfections." Engineering Structures, Vol. 31, 758-767

Masukawa, J., Kumiko, S., and Maekawa, K. (1999). "Three-Dimensional Nonlinear FEM Analysis of Hollow Bridge Piers Considering Spalling of Concrete Cover and Buckling of Reinforcing Bars." Transactions of The Japan Concrete Institute Vol. 21 255-262.

Mau, S. T., and El-Mabsout, M. (1989). "Inelastic Buckling of Reinforcing Bars." J. Eng. Mech. 115(1), 1-17

Moyer, M. J., and Kowalsky, M. J. (2003). "Influence of Tension Strain on Buckling of Reinforcement in Concrete Columns." ACI Struct. J. 03(2), 75-85.

Neuenhofer, A. and Filippou, F. C. (1998). "Geometrically Nonlinear Flexibility-Based Frame Finite Element. Journal of Structural Engineering". Vol. 124: No. 6, 704-711.

Neuenhofer, A., and Filippou, F. (1997). "Evaluation of Nonlinear Frame Finite-Element Models. Journal of Structural Engineering", Vol. 123, No. 7, 958-966

Nip, K. H., Gardner, L., and Elghazouli, A. Y., (2010) "Cyclic Testing and Numerical Modelling of Carbon Steel and Stainless Steel Tubular Bracing Members." Engineering Structures, Vol. 32, Issue 2, 424-441.

Otani, S. (1974). "Inelastic Analysisof R/C Frame Structures". Journal of Structural Engineering, Div., 100, pp. 1433-1449

Pacific Earthquake Engineering Research Center and Network for Earthquake Engineering Simulation (2010). Website of Concrete Column Blind Prediction Contest 2010.

Paulay, T. and Priestley, M. J. N. (1992). *Seismic Design of Reinforced Concrete and Masonry Buildings*, Wiley, New York.

Petrini, L., Maggi, C., Priestley, M. J. N. and Calvi, G. M. (2008). "Experimental Verification of Viscous Damping Modeling for Inelastic Time History Analyzes". Journal of Earthquake Engineering. Vol. 12:1, 125-145.

Priestley, M.J.N., Calvi, G.M., and Kowalsky, M.J. (2007) *Direct Displacement-Based Seismic Design of Structures*, IUSS Press, Pavia Italy, ISBN 978-88-6198-000-6. 740 pages.

Restrepo-Posada, J. I., Dodd, L. L., Park, R., Cooke, N. (1994). "Variables Affecting Cyclic Behavior of Reinforcing Steel." J. of Struct. Eng.,120(11), 3178-3196.

Rodriguez, M., Botero, J., and Villa, J. (1999). "Cyclic Stress-Strain Behavior of Reinforcing Steel Including Effect of Buckling." J. Struct. Eng., 125(6), 605-612.

Scott, M. H. and Fenves, G. L. (2006). "Plastic Hinge Integration Methods for Force-Based Beam-Column Elements." Journal of Structural Engineering. Vol. 132: No. 2, 244-252.

Shanley, F. R. (1947). "Inelastic Column Theory." J. Aeronautical Sciences, 14(5), 261–264.

Spacone, E., Ciampi, V., and Filippou, F. C. (1996). "Mixed Formulation of Nonlinear Beam Finite Element". Comput. Struct., 58, 71–83.

Urmson, C. R. and Mander, J. B. (2012) "Local Buckling Analysis of Longitudinal Reinforcing Bar." Journal of Structure Engineering, Vol. 138, No. 1, 62-71

Vecchio, F. J. and Collins, M. P. (1986). "The Modified Compression-Field Theory for Reinforced Concrete Elements Subjected to Shear". ACI Structural Journal. March-April: No 83-22, 219-231

Vecchio, F. J. and Collins, M. P. (1988). "Predicting the Response of Reinforced Concrete Beams Subjected to Shear Using Modified Compression Field Theory". ACI Structural Journal. May-June: No. 85-S27, 258-268

Yassin, M. H. M. (1994). "Nonlinear Analysis of Prestressed Concrete Structures under Monotonic and Cycling Loads". PhD dissertation, University of California, Berkeley.

Zhao, J. and Sritharan, S. (2007). "Modeling of Strain Penetration Effects in Fiber-Based Analysis of Reinforced Concrete Structures". ACI Structural Journal. Vol. 104: No. 2, 133-141.

Zong, Z., and Kunnath, S. (2008). "Buckling of Reinforcing bars in Concrete Structures under Seismic Loads." 14h World Conference on Earthquake Engineering.

Zong, Z., Kunnath, S., and Monti G. (2013). "Simulation of Reinforcing Bar Buckling in Circular Reinforced Concrete Columns.".ACI Struct. V.110. No.4, 601-616

APPENDICES

Appendix A
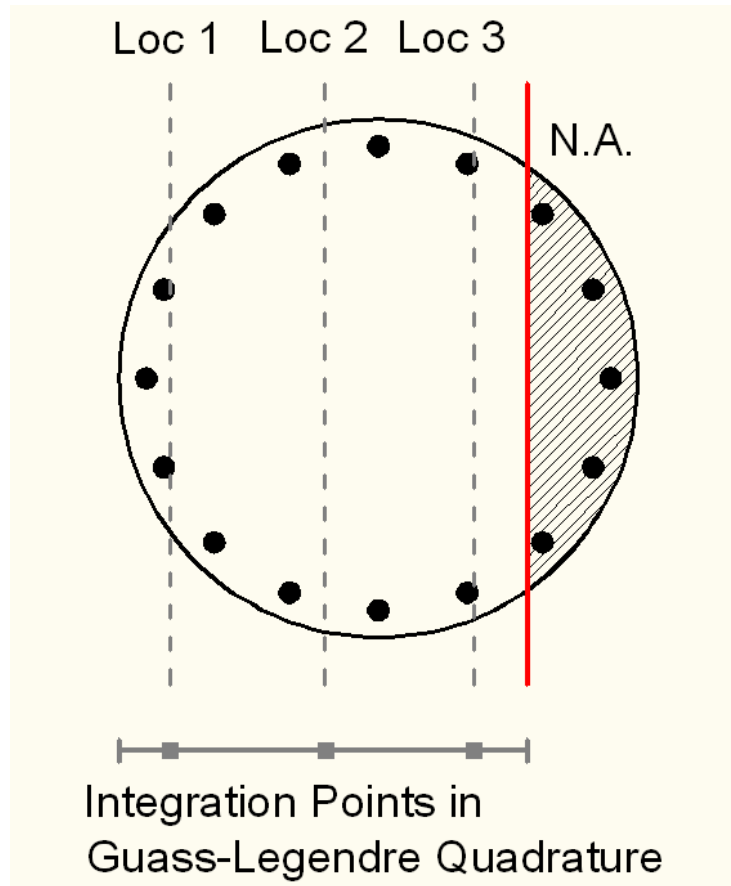
Figure A1. Locations at Tensile Side of a Section
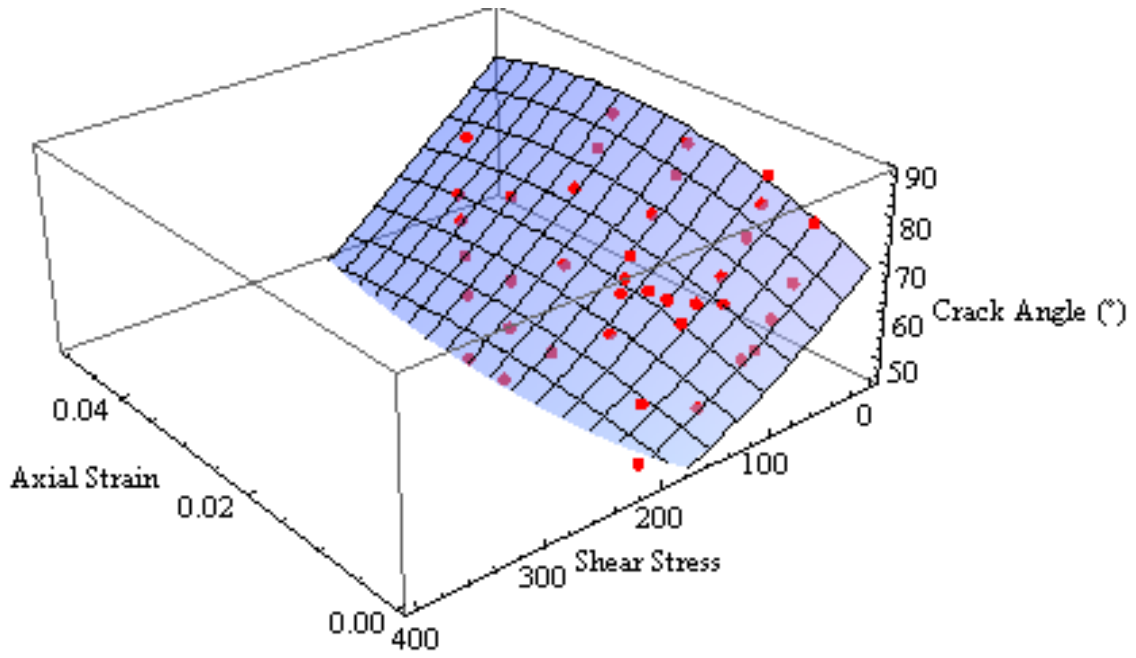
**Figure A2. Crack Angle Surface at Location 1**
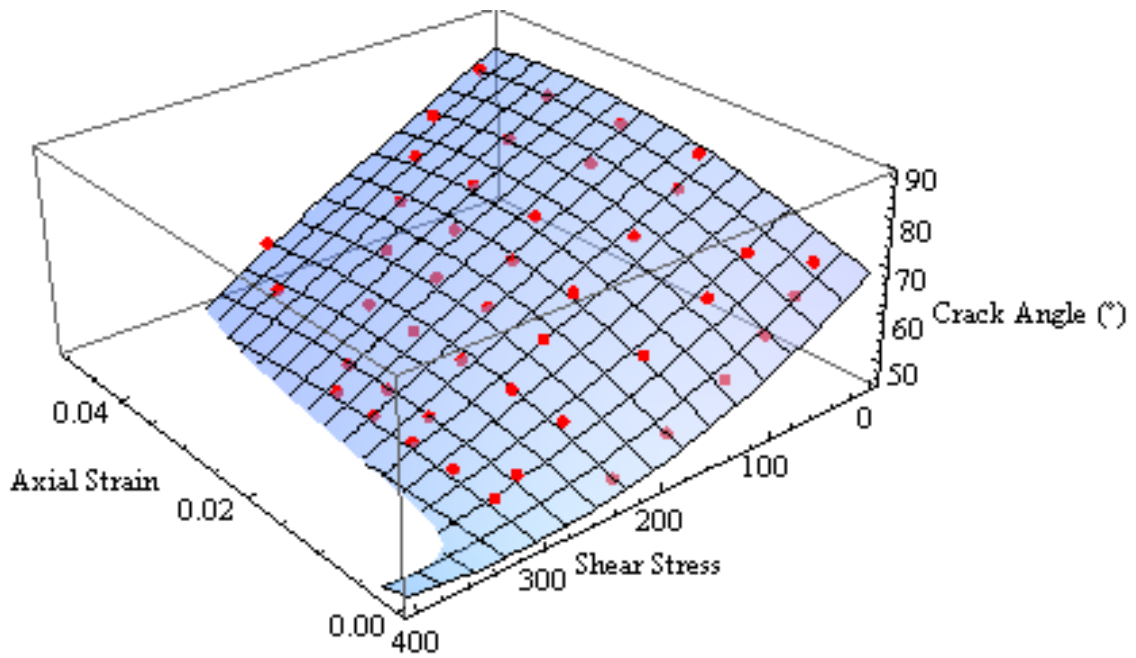
Figure A3. Crack Angle Surface at Location 2
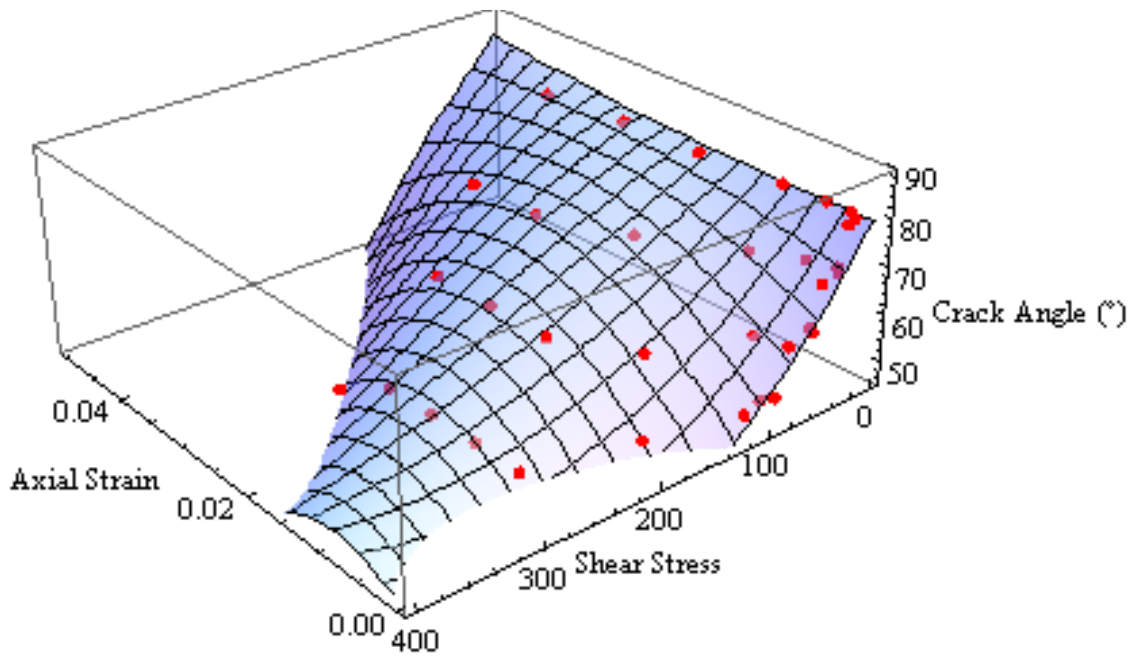
Figure A4. Crack Angle Surface at Location 3